ΕΛΛΗΝΙΚΗ ΔΗΜΟΚΡΑΤΙΑ

ΠΑΝΕΠΙΣΤΗΜΙΟ ΙΩΑΝΝΙΝΩΝ

ΠΟΛΥΤΕΧΝΙΚΗ ΣΧΟΛΗ

ΤΜΗΜΑ ΜΗΧΑΝΙΚΩΝ ΕΠΙΣΤΗΜΗΣ ΥΛΙΚΩΝ

ΠΡΟΓΡΑΜΜΑ ΜΕΤΑΠΤΥΧΙΑΚΩΝ ΣΠΟΥΔΩΝ

«ΠΡΟΗΓΜΕΝΑ ΥΛΙΚΑ»

ΜΕΤΑΠΤΥΧΙΑΚΗ ΔΙΑΤΡΙΒΗ

ΙΩΑΝΝΗΣ Ο. ΑΝΔΡΙΚΟΣ

“ΤΡΙΣΔΙΑΣΤΑΤΗ ΑΝΑΚΑΤΑΣΚΕΥΗ ΣΤΕΦΑΝΙΑΙΩΝ ΔΙΧΑΣΜΩΝ ΜΕ ΧΡΗΣΗ ΔΕΔΟΜΕΝΩΝ ΕΠΕΜΒΑΤΙΚΗΣ ΣΤΕΦΑΝΙΟΓΡΑΦΙΑΣ”

ΙΩΑΝΝΙΝΑ, 2018

Εσώφυλλο:

Η παρούσα Μεταπτυχιακή Διατριβή εκπονήθηκε στο πλαίσιο των σπουδών για την απόκτηση του Μεταπτυχιακού Διπλώματος Ειδίκευσης στην εξειδίκευση:

Βιοϋλικά και βιοϊατρική τεχνολογία

που απονέμει το Τμήμα Μηχανικών Επιστήμης Υλικών του Πανεπιστημίου Ιωαννίνων.

Εγκρίθηκε την ……..από την εξεταστική επιτροπή:

ΟΝΟΜΑΤΕΠΩΝΥΜΟ	**ΒΑΘΜΙΔΑ**
1. Δημήτριος Φωτιάδης, Επιβλέπων	Καθηγητής του ΤΜΕΥ της Πολυτεχνικής Σχολής του Παν/μίου Ιωαννίνων
2. Λεωνίδας Γεργίδης	Επίκουρος Καθηγητής του ΤΜΕΥ της Πολυτεχνικής Σχολής του Παν/μίου Ιωαννίνων
3. Λάμπρος Μιχάλης	Καθηγητής της Ιατρικής Σχολής, τμήμα Καρδιολογίας, του Παν/μίου Ιωαννίνων

ΥΠΕΥΘΥΝΗ ΔΗΛΩΣΗ

"Δηλώνω υπεύθυνα ότι η παρούσα διατριβή εκπονήθηκε κάτω από τους διεθνείς ηθικούς και ακαδημαϊκούς κανόνες δεοντολογίας και προστασίας της πνευματικής ιδιοκτησίας. Σύμφωνα με τους κανόνες αυτούς, δεν έχω προβεί σε ιδιοποίηση ξένου επιστημονικού έργου και έχω πλήρως αναφέρει τις πηγές που χρησιμοποίησα στην εργασία αυτή."

(Υπογραφή υποψηφίου)

Περίληψη

Η παρούσα μεταπτυχιακή διπλωματική εργασία παρουσιάζει μια υπολογιστική μέθοδο για την τρισδιάστατη ανακατασκευή διακλαδώσεων της στεφανιαίας αρτηρίας, χρησιμοποιώντας δεδομένα επεμβατικής στεφανιογραφίας. Ο απώτερος σκοπός αυτής της εργασίας είναι να αναδείξει την επίδραση του πλευρικού κλάδου στη ροής του αίματος.

Η έρευνα ξεκίνησε με την μελέτη των υπαρχόντων μεθοδολογιών, οι οποίες περιορίζονταν κυρίως στην τρισδιάστατη ανακατασκευή και μοντελοποίηση ροής αίματος σε απομονωμένα τμήματα των στεφανιών αρτηριών, παραλείποντας ουσιαστικά τον πλευρικό κλάδο από την ανατομία του στεφανιαίου διχασμού. Έχει επίσης αποδειχθεί πως οι ενδοθηλιακές διατμητικές τάσεις στο εσωτερικό των αρτηριών μπορούν να αποτελέσουν μια ισχυρή βάση για την οικοδόμηση ενός μοντέλου πρόβλεψης των περιοχών του ενδοθηλίου που είναι ευάλωτες στην ανάπτυξη στην ανάπτυξη αθηρωματικής πλάκας. Συνεπώς, έρευνες που στηρίζονται στην μοντελοποίηση στεφανιαίων τμημάτων, παραλείποντας την πλήρη ανατομία του διχασμού, μπορούν να οδηγήσουν σε υπερεκτίμηση ή υποεκτίμηση των διατμητικών τάσεων και ως εκ τούτου σε λάθος πρόβλεψη. Δημιουργείται λοιπόν η ανάγκη για γενίκευση του μαθηματικού μοντέλου, τόσο στο τρισδιάστατο χώρο, όσο και στον αριθμό των αρχικά επιβαλλόμενων συνοριακών συνθηκών, με σκοπό την δημιουργία ενός ακριβούς υπολογιστικού μοντέλου της ροής του αίματος.

Στο πρώτο κεφάλαιο της παρούσας διατριβής, παρουσιάζεται η ανατομία και φυσιολογία του καρδιαγγειακού συστήματος. Περιγράφονται αναλυτικά μαζί με τη σχετική βιβλιογραφία τα επόμενα θέματα: η λειτουργία της καρδιάς μαζί με τη δομή των αρτηριών και της κυκλοφορίας του αίματος. Επίσης παρουσιάζεται η παθογένεια καθώς και οι τρόποι αντιμετώπισης της αθηροσκλήρωσης. Επιπρόσθετα παρουσιάζονται οι τρόπους διάγνωσης και απεικόνισης της αθηροσκλήρωσης καθώς και τα πλεονεκτήματα και τα μειονεκτήματα αυτών στην κλινική εφαρμογή.

Στο επόμενο κεφάλαιο παρουσιάζεται η υπάρχουσα βιβλιογραφία γύρω από τις μεθόδους τρισδιάστατης ανακατασκευής των στεφανιαίων αρτηριών από απεικονιστικά δεδομένα επεμβατικής στεφανιογραφίας. Παρουσιάζονται επίσης οι συνοριακές συνθήκες με βάση τις οποίες μπορεί να επιτευχθεί η προσομοίωση της ροής του αίματος στα τρισδιάστατα μοντέλα των αρτηριών.

Στο τρίτο κεφάλαιο γίνεται παρουσίαση της προτεινόμενης μεθοδολογίας για την τρισδιάστατη αναπαράσταση την στεφανιαίων διχασμών με χρήση δεδομένων επεμβατικής στεφανιογραφίας, καθώς και ο τρόπος με τον οποίο πραγματοποιήθηκε η αξιολογηση της μεθόδου. Περισσότερο, αναφέρονται οι μαθηματικές υποθέσεις κάτω από τις οποίες πραγματοποιήθηκε η μοντελοποίηση ροής αίματος, όπως επίσης και μια προτεινόμενη μεθοδολογία για τον υπολογισμό του αιμοδυναμικού δείκτη Fractional Flow Reserve (FFR). Τέλος γίνεται παρουσίαση του συνόλου των δεδομένων που χρησιμοποιήθηκαν.

Στο τέταρτο κεφάλαιο παρουσιάζονται τα αποτελέσματα του πειραματικού μέρους της παρούσας διπλωματικής εργασίας. Συγκεκριμένα παρουσιάζονται και αναλύονται τα αποτελέσματα από την αξιολόγηση της προτεινόμενης μεθοδολογίας καθώς και τα αποτελέσματα την μοντελοποίηση της ροής τόσο σε διχασμούς όσο και σε τμήματα της στεφανιαίας. Περισσότερο, γίνεται επικύρωση του υπολογισμένου αιμοδυναμικού δείκτη FFR με βάση την επεμβατική μέτρηση.

Το πέμπτο κεφάλαιο αποτελεί συζήτηση πάνω στα αποτελέσματα των μεθοδολογιών καθώς στο τέλος της παρούσας διπλωματικής εργασίας αναφέρεται η βιβλιογραφία που χρησιμοποιήθηκε.

HELLENIC REBUBLIC

UNIVERSITY OF IOANNINA

TECHNICAL SCHOOL

DEPARTMENT OF MATERIAL SCIENCE AND ENGINEERING

MASTER OF SCIENCE

«ADVANCED MATERIALS»

MSc THESIS

IOANNIS O. ANSRIKOS

“3D RECONSTRUCTION OF CORONARY BIFURCATING ARTERIES USING CORONARY ANGIOGRAPHY DATA”

IOANNINA, 2018

Dedication

To my Family.

Abstract

This master thesis introduces a novel computational method for three-dimensional (3D) reconstruction of coronary bifurcating vessels utilizing Invasive Coronary Angiography (ICA) data. The novelty of this study is that it unveils the impact of the side branch of the coronary bifurcation anatomy on the blood flow patterns. The surveyed literature suggests that shear stress distribution on the endothelial tissue of the artery could be the base of the definition of a coherent prediction model for plaque development.

However, any existing state of the art methodologies omit theses data while computing the three-dimensional model suffering from potential over or underestimation of the shear stress and providing poor plague growth prediction capabilities. Thus, it is essential to generalize the existing mathematical models to the three-dimensional space as well as to the number of the imposed initial boundary conditions to provide a precise blood flow simulation model.

In this context, the anatomy and physiology of the cardiovascular system along with an in detail survey of literature on the topics of the heart functionality are initially introduced. Vascular system, blood circulation, pathogenesis, treating strategies, as well as medical imaging procedures are the core concepts that the reader should be familiar with.

The second chapter is dedicated on presenting the state of the art methodologies in the field of the 3D reconstruction of the coronary arteries from ICA data along with some mathematical background for blood flow simulation, while the contribution of our work is introduced in chapter 3. A novel methodology for the 3D reconstruction of the coronary bifurcated arteries from ICA data is proposed. The mathematical assumptions for the blood flow simulation as well as the algorithm for the computation of the Fractional Flow Reserve (FFR) are introduced to enforce the validation of our work.

Further experimental results are discussed on chapter 4, while chapter 5 concludes asserting the overall methodology, contribution and the impact of our work on the assessment of the Coronary Artery Disease (CAD).

List of Abbreviations

Acronym	*Meaning*
2D	Two Dimensional
3D	Three Dimensional
ASVD	Arteriosclerotic Vascular Disease
CAD	Coronary Artery Disease
CAU	Caudal Angulation
CFD	Computational Fluid Dynamics
CIMT	Carotid Intima Media Thickness
CRA	Cranial Angulation
CT	Computed Tomography
DARCA	Dual Axis Rotational Coronary Angiography
DC	Dice Coefficient
DICOM	Digital Imaging and Communications in Medicine
DM	Distal Main
DS	Degree of stenosis
EC	Endothelial Cell
ESS	Endothelial Shear Stress
FFR	Fractional Flow Reserve
FN	False Negative
FP	False Positive
HD	Hausdorff Distance
ICA	Invasive Coronary Angiography
IVUS	Intravascular Ultrasound
LAO	Left Anterior Oblique
LDL	Low Density Lipoprotein
LL	Lesion length
MLD	Minimum Lumen Diameter
MRI	Magnetic Resonance Imaging
NIRS	Near Infrared Spectroscopic
OCT	Optical Coherence Tomography
PET-CT	Positron Emission Tomography–Computed Tomography
PM	Proximal Main
PTCA	Percutaneous transluminal coronary angioplasty
QCA	Quantitative Coronary Angiography
RAO	Right Anterior Oblique
ROI	Region Of Interest
RVD	Reference Vessel Diameter
SB	Side Branch
SID	Source to Object Distance
SMC	Smooth Muscle Cell
SNR	Signal-to-Noise-Ratio
SOD	Source to Object Distance
TP	True Positive

List of Symbols

Symbol	*Meaning*
I_1	1st angiographic view
I_2	2nd angiographic view
BM_{left}	Left border of the main branch
BM_{right}	Right border of the side branch
BS_{left}	Left border of the side branch
BS_{right}	Right border of the side branch
C_{MB}	Centerline of the main branch
C_{SB}	Centerline of the side branch
C_{MBs}	Smoothed centerline of the main branch
C_{SBs}	Smoothed centerline of the side branch
BRP_{I_1}	Bifurcation reference point of the 1st view
BRP_{I_2}	Bifurcation reference point of the 2nd view
$LD_{MB\_I_1}$	Lumen diameter of the 1st view main branch
PS	Pixel Size
S_1	1st X-ray source point
S_2	2nd X-ray source point
SOD	Source to object distance
SID	Source to image distance
OID	Object to image distance
$R_{x\_I_1}$	x-axis rotation matrix of the 1st view
$R_{x\_I_2}$	x-axis rotation matrix of the 2nd view
$R_{y\_I_1}$	y-axis rotation matrix of the 1st view
$R_{y\_I_2}$	y-axis rotation matrix of the 2nd view
OID	ISO center
$Surf_{MB\_I_1}$	Back projected surface of the 1st view main branch
$Surf_{MB\_I_1}$	Back projected surface of the 2nd view main branch
$Surf_{SB\_I_1}$	Back projected surface of the 1st view side branch
$Surf_{SB\_I_1}$	Back projected surface of the 2nd view side branch
C_{MB_3D}	3D centerline of the main branch
C_{SB_3D}	3D centerline of the side branch
N_{MB_3D}	Normal vector of the 3D main branch
N_{SB_3D}	Normal vector of the 3D side branch
PL_{MB_3D}	Plane perpendicular to the 3D centerline of the main branch
PL_{MB_3D}	Plane perpendicular to the 3D centerline of the side branch
$Contour_{MB\_3D}$	3D lumen contour of the main branch
$Contour_{SB\_3D}$	3D lumen contour of the side branch
G_{MB}	Geometry of the main branch
G_{SB}	Geometry of the side branch

Table of Contents

List of Figures

List of Tables

Chapter 1. Introduction

1.1 Physiology of the Cardiovascular System

1.1.1 The Heart

The human heart is the core muscular organ of the Cardiovascular System. In fact, the heart is the pump that drives the Circulation System [1]. It is about the size of a fist and is located to the left of the middle of the chest cavity. The average adult heart size is approximately 14 cm long and 9 cm wide [2]. The pericardium membranes of heart consist of three layers: the outer (pericardium), the middle (myocardium) and the inner layer (epicardium) (Figure 1.1). The external layer (pericardium), comprising of connective tissue as well as adipose tissue, is responsible for the heart protection; it provides a sufficient isolation layer by reducing the friction between the heart and other vital organs, during the cardiac cycle.

Next to the row is the myocardium, the thick middle layer made up cardiac muscle tissue, nerve fibers, and blood and lymph capillaries. The operation of this layer is to pump the blood out of heart chambers. The endocardium consists of connective tissue, elastic fibers, collagenous as well as many blood vessels. The internal of the heart is divided into four chambers whose walls are

made of cardiac muscle. The upper chambers (Atria) receive the blood returning to the heart while the lower two chambers (Ventricles) pump the blood into the arterial vessels. A solid wall-like structure, known as Septum separate the right atria and ventricle from the left atria and ventricle. As a consequence, the blood circulating through the left side of the heart cannot be mixed with blood circulating through the right side of the heart. Furthermore, the unidirectional blood flow from ventricle to atria is ensured by the operation of the atrioventricular valves (AV valve), which are consists of the tricuspid valve on the right and the mitral valve on the left.

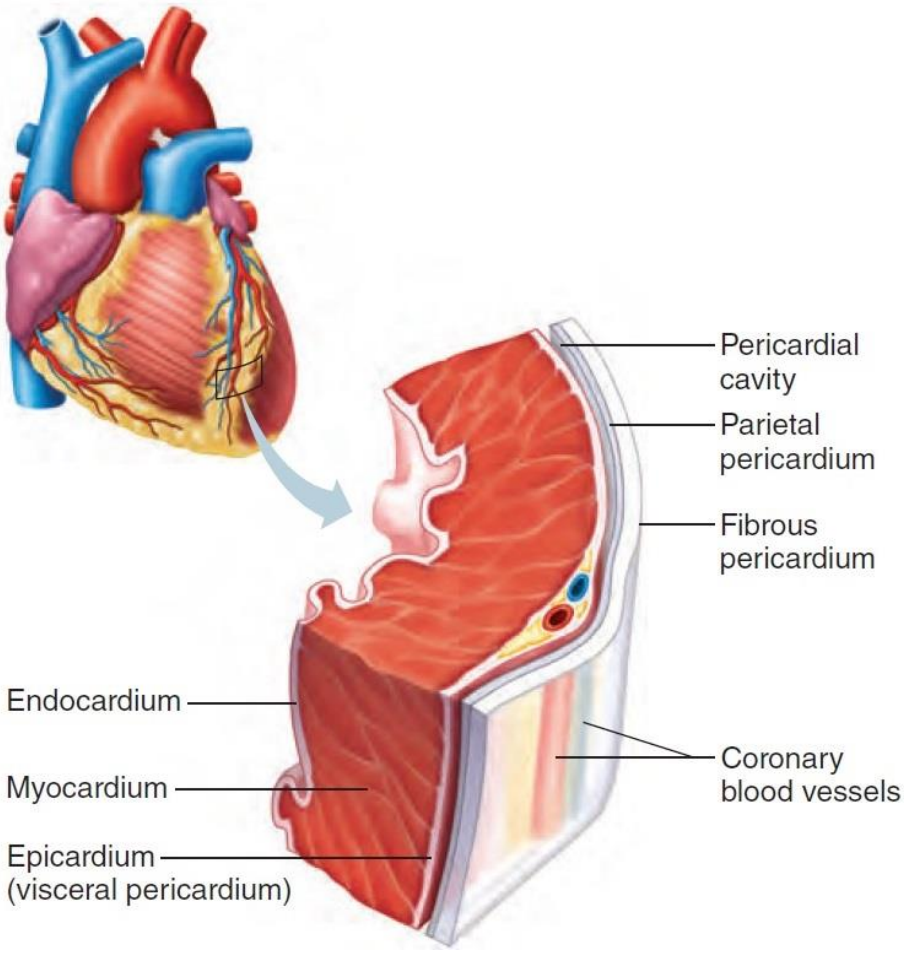

Figure 1.1: Heart wall layers [3].

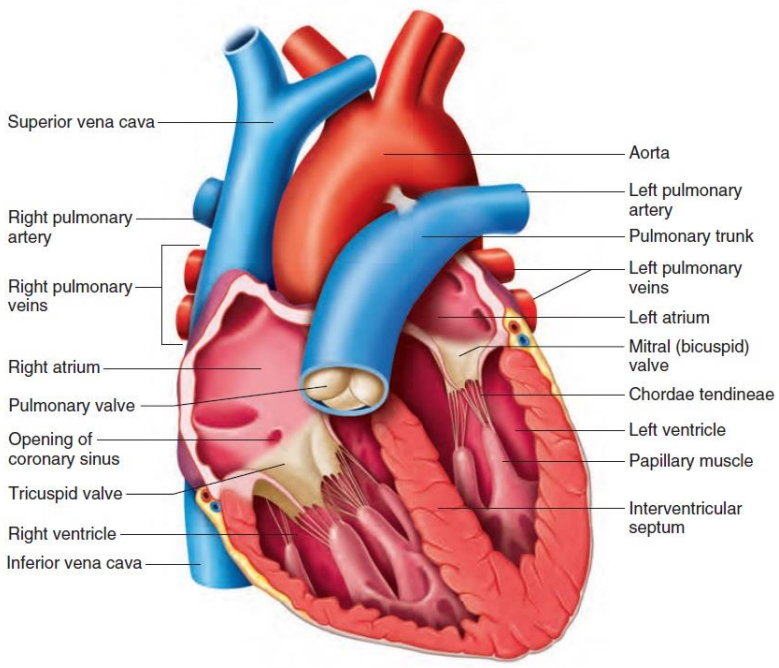

Figure 1.2: Heart's anatomy [3].

The blood flows into the heart, though three veins accessing to the right atrium of the heart. Superior and inferior vena cava are the two main veins routing the blood to the heart from the head and the body, respectively, while coronary sinus aims to drain blood from the heat's myocardium (Figure 1.2). The blood flows from the right atrium into the right ventricle through the tricuspid valve. Tricuspid valve features projections (cusps) to prevent any potential blood backflow. The right ventricle provides low resistant blood flow to the lungs while the left one provides the rest of the body with high resistance blood flow. In this context, left ventricle walls are thicker than the right ones. Right ventricle contracts to increase the blood pressure in the chamber. As a result, the tricyclic valve is passively closed and the blood is allowed to flow only through the pulmonary trunk. The pulmonary trunk is divided into the right and the left pulmonary arteries that lead the blood to the lungs. In addition, a valve (pulmonary valve) lies at the base of the pulmonary trunk to ensure the unidirectional blood flow to the lungs, preventing the blood backflow into the ventricle.

Regarding the operation of the left side of the heart, four pulmonary veins lead the blood returning from the lungs, into the left atrium. The mitral valve (bicuspid valve) ensures the one-way blood flow from the left atrium to the left ventricle, preventing any blood backflow into the

left atrium's chamber. The blood flow is directed to the large artery (aorta) when the mitral valve closes. The aortic valve, located at the entrance of the aorta, allows the blood to leave the right ventricle, preventing also the blood backflow. Finally, the blood flows through the aorta to the rest of the Circulatory system. The first two aortic branches are divided into the left and right coronary artery, supplying the heart tissue with blood (Figure 1.3).

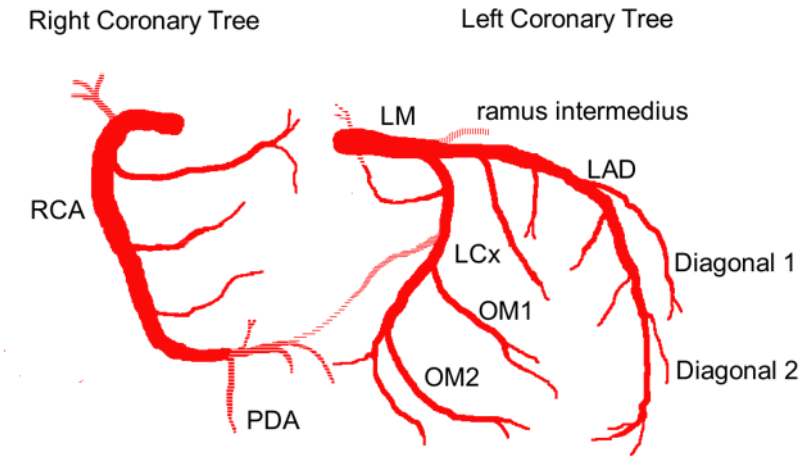

Figure 1.3: Coronary arteries [3].

1.1.2 The circulation of blood

In the human body there are about four to six liters of blood which flow through the circulation system, transferring oxygen and nutrients to the cells, whereas removing carbon dioxide (CO_2) and other wastes away from the cells [4]. In addition, blood flow controls the body temperature. Blood consists of three main types of cells: red blood cells (erythrocytes), white ones (leukocytes) as well as plasma. The blood flow is divided into two individual circulations: the pulmonary circulation and the systemic one.

Pulmonary circulation is defined as the circulation of blood between the heart and the lungs. The pulmonary artery receives blood from the right ventricle of the heart. Then, blood reaches the left and the right lungs via the corresponding pulmonary arteries (left and right). Inside the lungs, the artery splits into smaller arteries known as arterioles and capillaries. Capillaries and the alveoli of the lugs are in touch to facilitate the oxygen and CO_2 exchange. Finally, the fresh and oxygenated blood finds its way back to the heart though the left and the right pulmonary veins which are merged to constitute the main pulmonary vein (Figure 1.4).

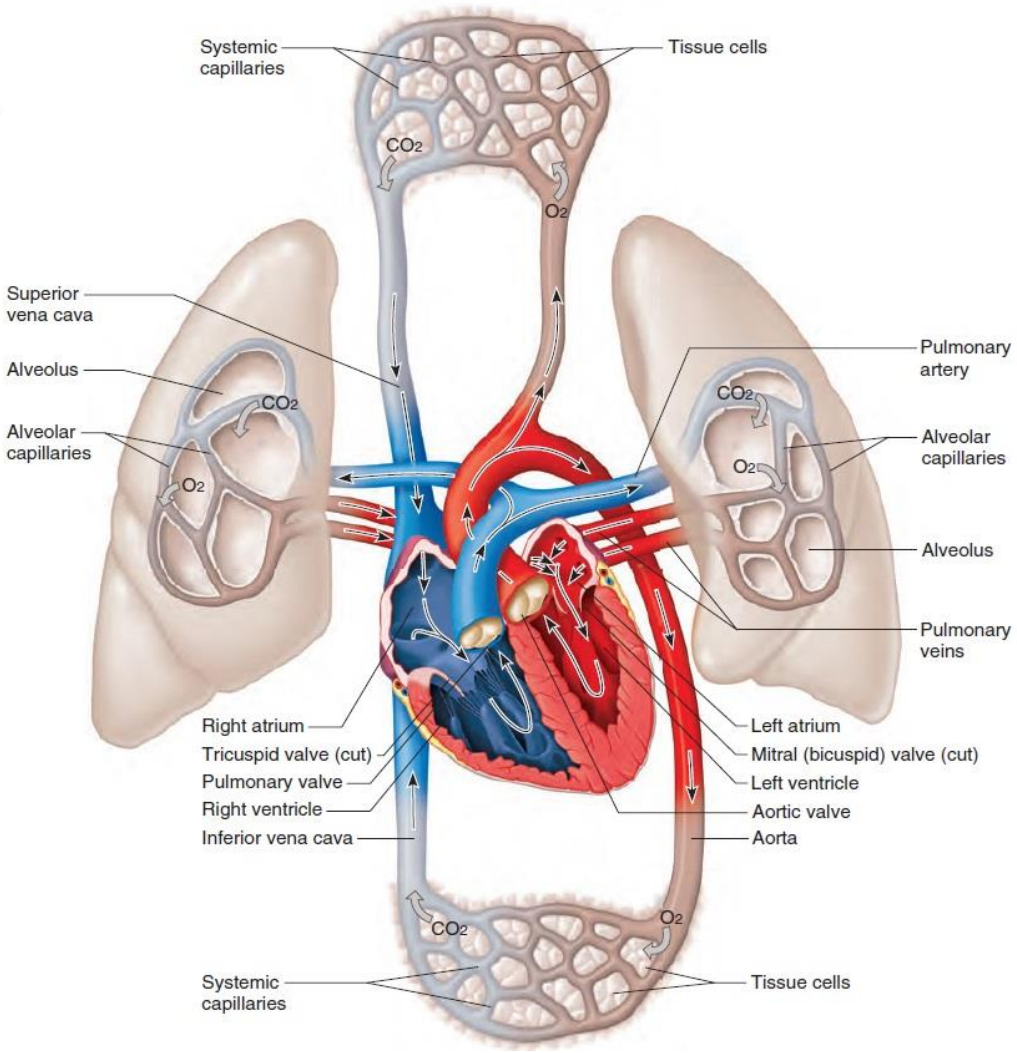

Figure 1.4: The circulatory system [3].

On the other hand, systemic circulation is defined as the circulation of blood from the heart to the rest of the body. More specifically, the fresh blood enters the aorta leaving the heart's left ventricle chamber to reach the whole body through a complicated network of vessels. Furthermore, the blood flows through separate branches of the aorta approaching all the arterioles and the capillaries of the human body. There, the exchange of oxygen and CO_2 between the blood and the cells eventually take place. The blood, carrying more carbon dioxide as well as other organic waste products, ends up to the heart through two main veins: the inferior vena cava, which collects the blood from the lower body, and the superior vena cava which collects the blood from the upper body (Figure 1.4).

1.1.3 The vascular system

The circulatory system constitutes of vessels that carry blood through the body. The vessels are divided into three main categories: the arteries, the veins and the capillaries [5]. The arteries are blood vessels that carry oxygenated blood from the heart to all organs and the body. On the contrary, the veins which are also blood vessels, carry the blood, which contains CO_2 and other waste products, back to the heart. The tiny blood vessels between arteries and veins called capillaries distribute oxygen-rich blood to the body.

The blood vessels have complex structures with distinct features. The arterial wall is composed of three different layers: the external (tunica adventitia), the middle (tunica media) and the internal layer (tunica intima) [6]. Tunica adventitia is composed of collagen, fibroblasts and perivascular nerve cells. The collagenous adventitia adds rigidity while the elastic lamina provides elasticity to the vessel. Tunica media is made of Smooth Muscle Cells (SMCs), fibers and elastic connective tissue. The main operation of tunica media is to maintain the blood pressure in the vessel. Finally, the inner wall, or tunica intima, is made of Endothelial Cells (ECs). This layer is critical since the endothelium tissue prevents the blood clotting, infection and inflammation of adjacent tissues (Figure 1.5).

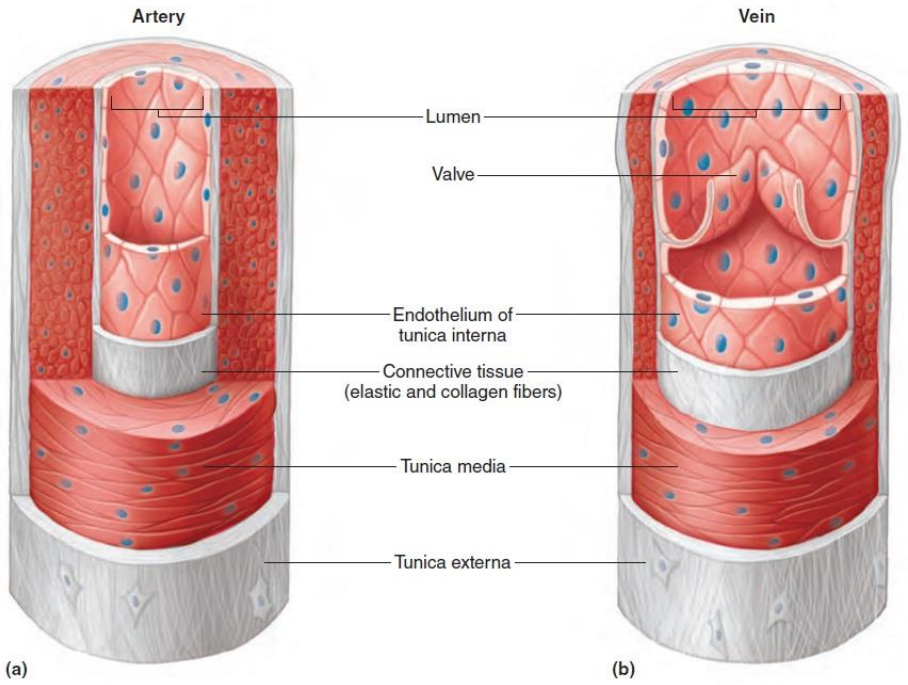

Figure 1.5: a) Artery wall layers, b) vein wall layers [3].

Regarding the structure of the veins, they present the same tissue layers with the arteries. Nevertheless, there are important differences between veins and arteries. Both the middle layer and the outer layer of the veins are thinner than the corresponding arterial layers. Unlike arteries, this occur because the veins do not maintain blood pressure in the vessel. Finally, the veins have valves in their inner walls which control the backflow of blood, even against gravity (Figure 1.5).

1.2 Atherosclerosis

Atherosclerosis (Arteriosclerotic Vascular Disease - ASVD) is a chronic inflammatory disease of arteries, which was enlisted as a one of the leading cause of death worldwide. The high concentrations of cholesterol and Low-Density Lipoprotein (LDL) in the blood is the main reason causing the specific disease [7]. Atherosclerosis was observed to be a critical disease because the arterial occlusion reduces the blood flow to major organs such as the heart or the brain. It starts when the endothelium tissue of the artery wall becomes damaged, developing inflammation, plaque growth which ends up to vessel stenosis and thrombosis. Clinical studies have shown that atherosclerosis is caused by several risk factors such as smoking, alcoholism, hypertension, increased level of cholesterol, obesity, diabetes mellitus as well as genetic predisposition. Researchers argue that the vessels which mainly suffer from atherosclerosis are the coronary arteries, the carotid arteries, the peripheral arteries as well as the aorta.

1.2.1 Atherogenesis

The process of the atherosclerosis disease development is called atherogenesis. Initially, atherogenesis confers a qualitative change in the endothelial cells, despite the endothelium tissue operation which is to resist on the white blood cells attachment on it [8]. In fact, this functionality of endothelial tissue is destroyed when subjected to irrigative stimuli such as dyslipidemia, hypertension or pro-inflammatory mediators. As a result, the changes in endothelial permeability assist the LDL particles to penetrate into the arterial wall [9]. Once the LDL particles enter into the arterial wall inflammation is developed. The endothelial cells, due to their damage, do not produce any more nitrogen monoxide but emit a risk signal, attracting white blood cells in the area. These cells (phagocytes) consume the LDL of the arterial wall, resulting in the swelling and the transformation of them into foamy fat cells. Then, the foamy fat cells are destroyed, releasing a fatty substance which exacerbates inflammation. Moreover, the atheroma is extended into the middle layer of the arterial wall, lesioning the smooth muscle cells. The SMCs, in their effort to

limit inflammation, swell and proliferate to form a fibrous capsule, resulting in an increase in the size of the atherosclerotic plaque. In advanced lesions, SMCs and macrophages die by apoptosis, forming the lipid pool or the necrotic core of the plaque [10]. The ultimate state of atherogenesis is thrombosis which complicates the rupture of the capsule surrounding the atherosclerotic plaque. Thrombus extends into the vessel lumen, where it can impede the blood flow (Figure 1.6).

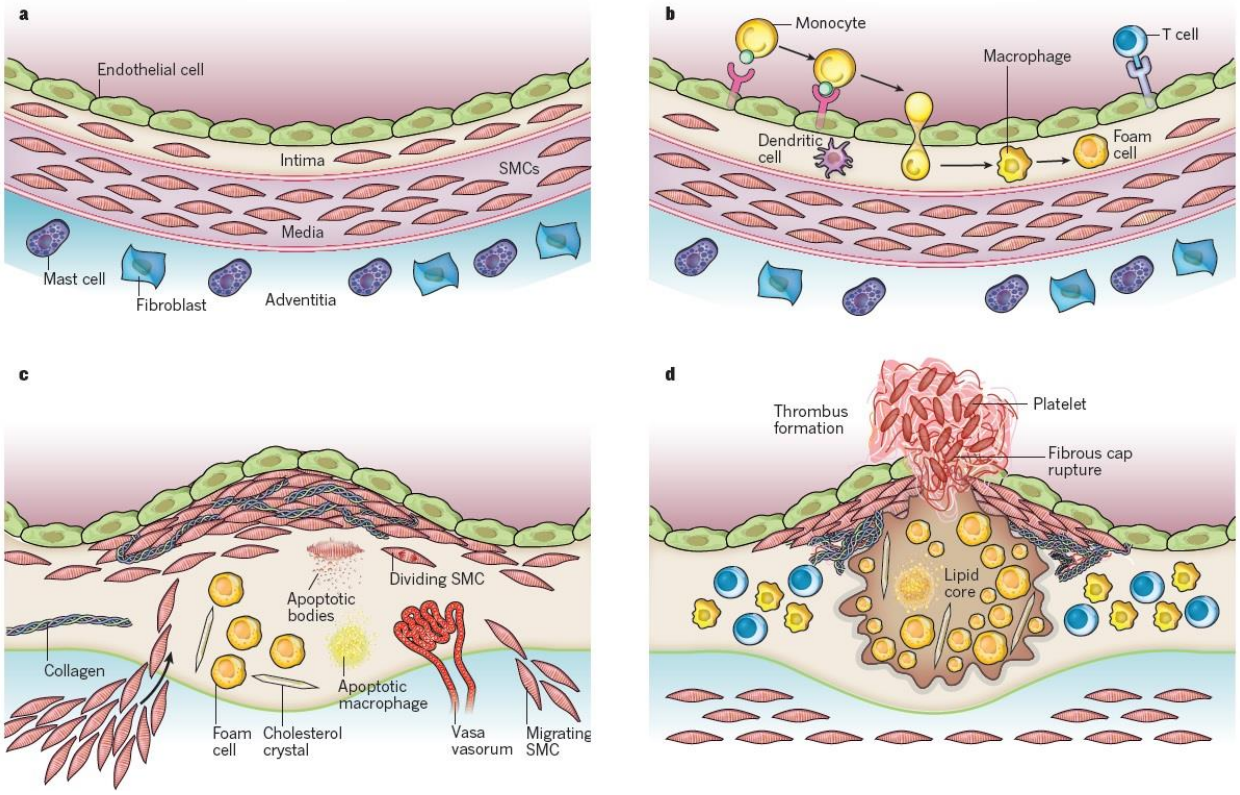

Figure 1.6: Atherogenesis: a) the healthy artery having three layer structure, b) adhesion of the white blood cells in the endothelial tissue, c) lesion extension into SMCs, d) and plaque rupture and thrombosis [8].

Regarding the risk factors for atherosclerosis, several traits, conditions, or habits may raise the risk for the disease evolution. Some of them, such as hypertension, affects directly the atherogenesis. Briefly, the increased level of blood pressure swells the arterial wall in the region of the lesion, forming a sac known as aneurysm. This arterial wall deformation affects the blood flow pattern, contributing to the concentration of white blood cells on the inner wall of the artery. Moreover, smoking, alcoholism and diabetes mellitus increase the risk of atherosclerosis.

Furthermore, the increased level of cholesterol and LDL in the blood is considered a major risk factor of atherogenesis and prevails the cardiovascular research [11].

1.2.2 Atherosclerosis treatment

Any artery in the body could suffer of atherosclerosis disease. Nevertheless, coronaries arteries, responsible for supplying the heart with blood, carotid arteries, transferring the blood to the brain, as well as peripheral arteries in arms and legs are more prone to atherogenesis than the other vessels of the body. Therefore, atherosclerosis could be classified based on the type of the vessel where the lesion is located, i.e. coronary artery disease, carotid artery disease and peripheral artery disease. Consequently, the need for an individual treatment oriented to each subcategory is comes. Considering the coronary artery disease, plaques are developed inside the coronary vessels, restricting the blood flow to the heart. Heart attack is taking place when the plaque rupture, the thrombus and the blood clotting, are blocking the blood flow completely to the heart muscle [12]. Respectively, once plaque is developed in the carotid artery the blood flow to the brain is restricted. Zero or limited blood flow to the brain is causing a stroke [13]. Regarding the peripheral artery disease, atheromatous plaque is developed in main arteries, reducing the blood flow to the legs, arms and the rest body. Symptoms such as numbness and pain in the limbs, declare the peripheral artery disease [14].

Atherosclerosis treatment has been improved, increasing the life expectancy of people with heart failure. A taxonomy of atherosclerosis treatment techniques suggests a priory and posterior cardiovascular event actions: lifestyle changes, medicines, medical procedures and surgery. The lifestyle changes include healthy eating and physical activity aiming for a healthy weight, stress management, no smoking and no alcohol consumption. If the lifestyle changes are not enough to suppress the atherosclerosis progression, drugs should be prescribed to patients. LDL is a major risk factor for coronaries heart disease. Statins are the first – line choice for reducing the oxidation of LDL, which contributes to their effectiveness at preventing atherosclerotic disease [15]. In fact, drugs control the blood pressure reducing the need of the heart for oxygen. Finally, the main purpose of the drugs is to improve to a certain extent, the poor blood supply to the heart or to the brain. Lesions with an increased degree of stenosis are treated with invasive ways such as coronary angioplasty, bypass operation, and endarterectomy. Coronary angioplasty is the dilation of an occluded coronary artery with a balloon. Moreover, a stent is placed in the region of the lesion

preventing future occlusion of the artery (restenosis) (Figure 1.7). In many cases, the stent is eluted with a drug leading to more effective treatment of the lesion [16]. Bypass is a surgical operation and constitutes the most difficult treatment of atherosclerosis (Figure 1.7). Briefly, an autologous vessel is collected from another part of the patient's body and is placed on the coronary tree, bypassing the occluded artery [17]. Usually, the blood vessel is collected from legs while sometimes an artificial vessel is used for this kind of treatment. During the operation of the endarterectomy lipid plaques are removed from the semi-occluded arteries. This kind of treatment is applied mainly to carotid arteries.

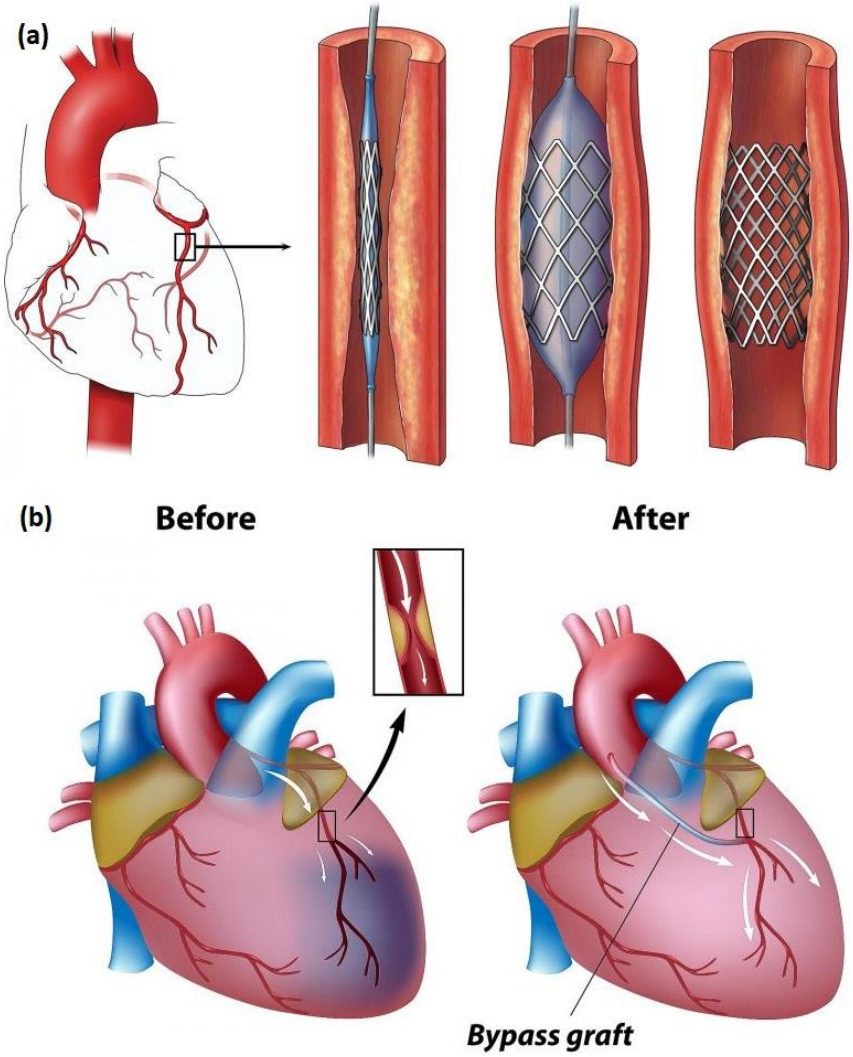

Figure 1.7: Invasive atherosclerosis treatment: a) angioplasty - stent application, b) and bypass operation.

1.2.3 Coronary bifurcation atherosclerosis

Bifurcations are one of the most challenging coronary lesions in cardiology, accounting for the 15-20% of the total Percutaneous Coronary Investigations (PCI) [18]. As a result, in 2004, the European Bifurcation Club (EBC) was founded, promoting the cardiovascular research on the coronary bifurcations. The definition of the bifurcation is: the point where a major coronary artery is divided into a main and a side artery. Atherosclerosis in coronary bifurcations presents a complex structure while several factors such as the coronary anatomy and the blood flow patterns, affect both the atherosclerosis progression and the vascular biology [19]. Therefore, there is the need for a special diagnosis and treatment, oriented to the bifurcation lesions. Regarding the coronary anatomy, a bifurcated artery is divided into three individual branches: the coronary vessel before the bifurcation – Proximal Main (PM), and the two coronary branches after the bifurcation: Distal Main (DM) and Side Branch (SB), respectively [19]. As a consequence, atherosclerosis can be developed separately or in total in the coronary branches. The classification of the bifurcation lesion is depicted in a medical cardiovascular map known as medina score (Figure 1.8).

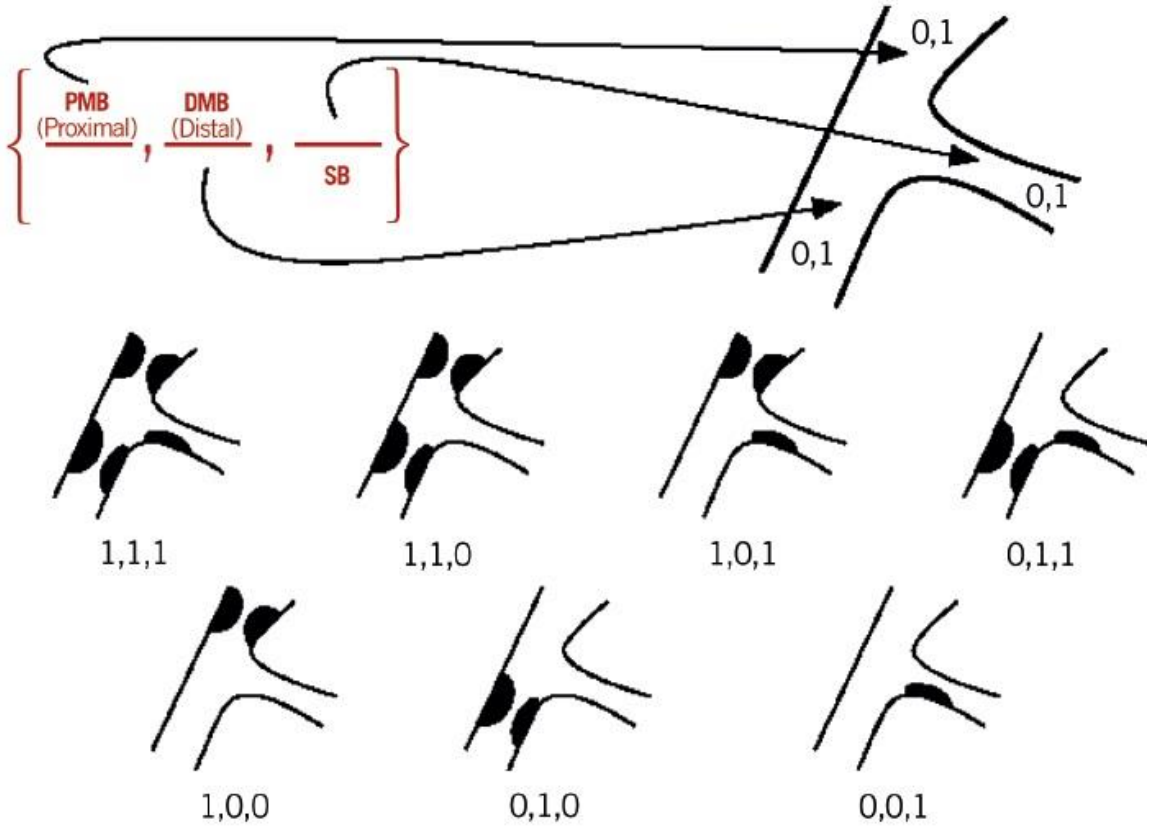

Figure 1.8: Medina score [18].

1.3 Atherosclerosis imaging

Diagnosis of the Coronary Artery Disease (CAD) is based on both clinical and imaging data. In many cases, clinical data such as biochemical examinations, are not capable to provide the risk level of the atherosclerosis progression. Consequently, some major features of the coronary lesions such as the arterial degree of stenosis, the type and the concentration of the atheromatous plaque in the region as well as the thrombogenesis could be diagnosed using only imaging techniques. Nowadays, both the cardiovascular research and the advances in medical imaging technology provide a range of diagnostic tools to characterize the coronary artery disease [20]. The coronary artery imaging techniques are divided into two main categories: the invasive and the non-invasive imaging modalities [21]. Each imaging technique of atherosclerosis provides unique clinical outcome, contributing to novel improved strategies for the coronary lesion treatment.

1.3.1 Invasive atherosclerosis imaging

First cardiac catheterization applied in humans in 1929 using X-ray imaging. Briefly, a narrow wire with the catheter on the top approaches the coronary arteries of the heart (right or left) through the femoral artery of the patient. Contrast agent is injected into the coronary tree revealing any lesion along the vessels. The degree of stenosis remains a major metric which presents the magnitude of the coronary lesion. X-ray angiography or Invasive Coronary Angiography (ICA), was the first invasive imaging which demonstrates both the degree of stenosis and the lesion length of the artery suffer from atherosclerosis (Figure 1.9 a) [22]. Nevertheless, despite the ability of the X-ray angiography to monitor these major atherosclerosis features, the need for internal operation imaging of the arteries is raised. Indeed, the accurate description of the arterial pathology and the lesion progression such as the plaque type, the changes in the composition of the plaque, the thrombogenesis, and the blood clotting are detected using only intravascular imaging techniques [23].

Intravascular Ultrasound (IVUS) is currently the most widely used intravascular imaging modality worldwide (Figure 1.9 b). As the IVUS catheter is passing through the coronary vessel (pull-back), an ultrasound signal (20-70 MHz) is emitted perpendicular to the arterial inner walls. The backscattered signal is received from the catheter and is analyzed into cross-sectional images of the vessel. As a result, this process allows the tomographic assessment of the lumen area, the plaque size, the distribution and the composition of the plaque and the stent positioning, the media,

even the artery's adventitia. Several methodologies, based on radiofrequency analysis of the backscatter signal, have been proposed to increase the accuracy of the plaque characterization (VH-IVUS) [24]. Moreover, these advanced IVUS methodologies take into account both the amplitude and the frequency of the backscattered signal, extracting more plaque features than the simple IVUS.

Optical Coherence Tomography (OCT) is an interferometric imaging technique that provides cross-sectional views of the subsurface microstructure of the biological tissue (Figure 1.9 c). It has almost the same functionality with IVUS, but it is based on different signal processing techniques. In fact, the OCT catheter produces near-infrared light perpendicular to the arterial inner walls and it measures both the delay and the magnitude of the backscattered light [25]. Consequently, high-resolution images are generated (12-18μm), depicting the vessel walls in detail. Considering some lesion features, OCT imaging presents a better sensitivity than the IVUS. Indeed, thrombus, hemorrhage, neointimal hyperplasia, and stent position (malapposition, struts detection) are more visible in OCT than the IVUS [26]. The major disadvantage of the OCT imaging is its poor signal penetration (2-3mm), which often inhibits visualization of the artery's adventitia (outer wall). Furthermore, a relatively recent implementation of optical coherence tomography is the frequency domain OCT (FD-OCT) which provides benefits in signal to noise ratio (SNR).

Finally, Near Infrared Reflectance spectroscopy (NIRS) is used for the accurate detection of the lipid components (cholesterol) along the vessel (Figure 1.9 d) [27]. NIRS, which is integrated on the catheter, uses wave lengths (800-2500 nm), converting a diffuse reflectance signal from the arterial walls to produce a spectrum. In fact, different organic molecules reflect and scatter light to different degrees and at various wavelengths. Therefore, the spectral analysis of the reflected light depicts the tissue chemical composition, allowing the detection of the lipid plaques. Nevertheless, NIRS cannot provide any visualize of the arteries anatomy such as the inner or the outer wall.

Despite the ability of the intravascular imaging techniques to depict biological features of the atheromatic plaques, none of them can provide any information about the vessel geometry and the distribution of the plaque into the arterial wall. On the contrary, X-ray angiography is capable to provide geometrical features (e.g. stenosis) about the lesion along the coronary vessel, but it cannot provide any plaque characterization. Consequently, nowadays the medical invasive treatment of

coronary atherosclerosis utilizes a hybrid image modality which is based on the fusion of the X-ray angiography and the intravascular imaging.

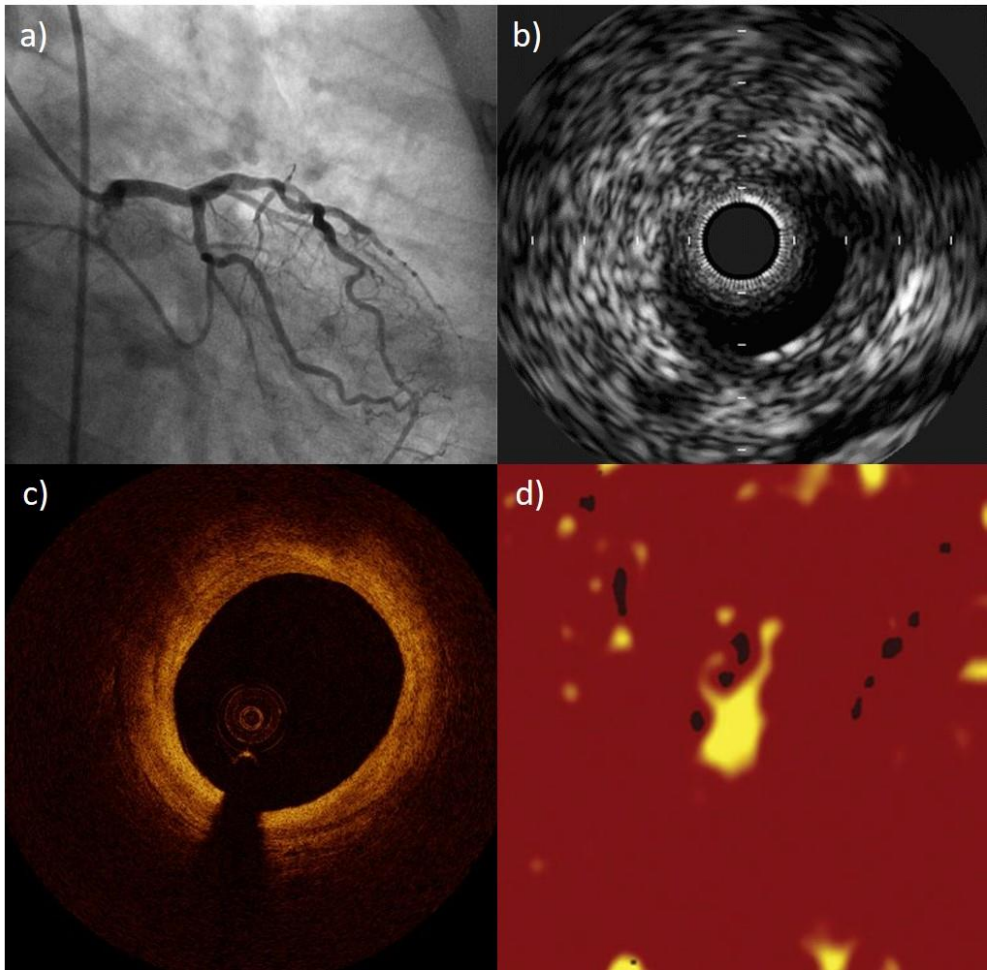

Figure 1.9: invasive atherosclerosis imaging: a) X-ray angiography, b) IVUS, c)and OCT, NIRS [21, 27].

1.3.2 Non-Invasive atherosclerosis imaging

Ultrasound imaging represents a non-invasive, fast and cheap method of assessing atherosclerosis. It is mainly applied in cases of carotid and peripheral artery disease, allowing the accurate measurement of the distance from the luminal surface to the intima-media boundary, called Carotid Intima-Media Thickness (CIMT) [28]. Regarding the functionality of the ultrasound imaging, acoustic signals are transmitted from the epidermis to carotid artery, penetrating into any type of tissue. The reflected signals are received from the device in order to localize and characterize

different tissue types (Figure 1.10 a). Nevertheless, ultrasound is limited in its ability to detect plaque components and morphology of the vessel [29].

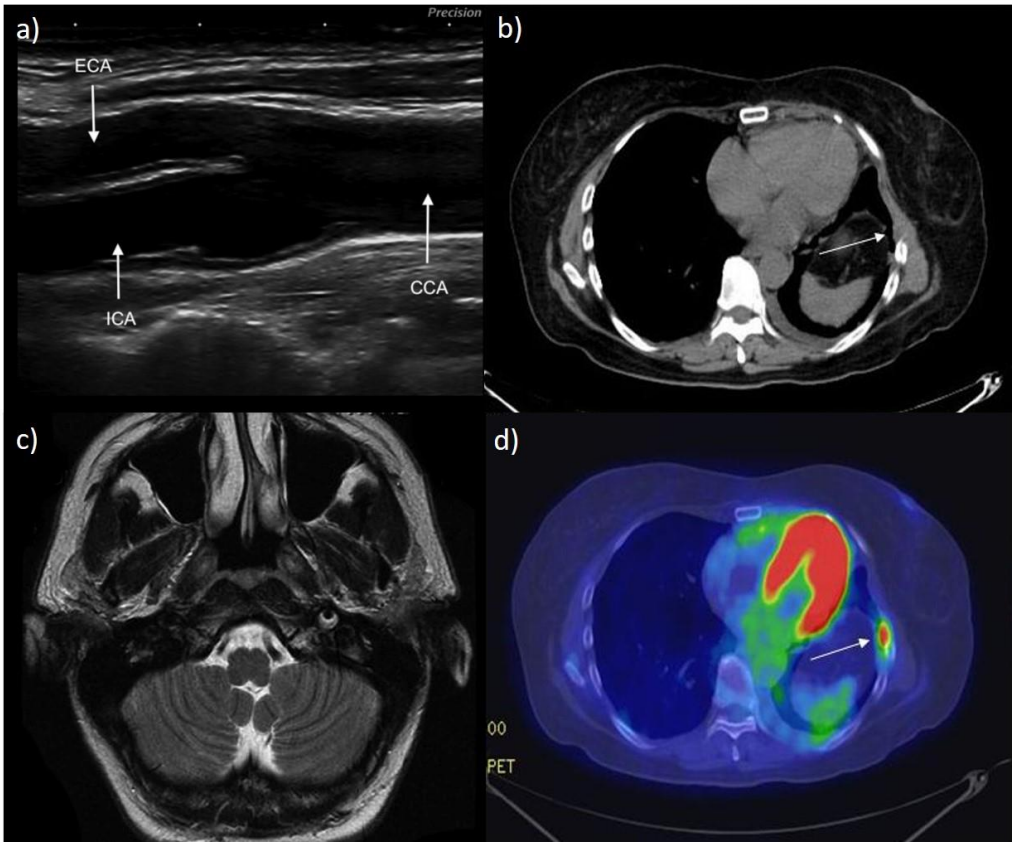

Figure 1.10: Non-invasive atherosclerosis imaging: a) Ultrasound, b) CT, C) MRI, d) PET-CT [30].

The Last years, Coronary Tomography Angiography (CTA) has been gaining widespread acceptance in clinical practice for the investigation of coronary artery disease (CAD) [31]. Briefly, contrast agent is injected through veins into the patient's body before the exam, in order to generate images with an increased level of contrast. CT scan is performed in multiple planes, producing cross-sectional images of the body (Figure 1.10 b). Nowadays, CT scans produce up to 320 high-quality image around the human body, allowing an accurate detection of the atherosclerotic lesions. Comparing with the invasive imaging techniques, CT is less performable in the detection and the characterization of the atheromatic plaques. In this context, many studies address the detection of coronary atheromatous type, especially the calcified and the non-calcified plaques [32]. Moreover, the major limitation of CT is the dangerous exposure of patient to radiation which probably could cause cancer [33].

Magnetic Resonance Imaging (MRI) of the atherosclerosis can depict information both of the arterial walls and the plaque volume. It is mainly applied in cases of carotid desease. The majority of the proposed studies focus both on the carotid artery and aorta, presenting the ability of the MRI to visualize the vessel anatomy and to detect the plaque composition [28]. MRI uses the body's natural magnetic properties to produce detailed cross-sectional images (Figure 1.10 c). In fact, during the application of the magnetic field on the human body, the various types of tissues present individual responses, allowing the depiction of body's anatomy on the image [34]. Unlike CT, MRI does not involve exposure of the patient to ionizing radiation. Regarding the limitation of MRI, high-quality images are assured only if the patient is able to remain perfectly still and follow breath-holding instructions while the images are being recorded, even the heart-beat affects the procedure.

Finally, Positron Emission Tomography in combination with computed tomography (PET-CT) remains an important non-invasive medical imaging technique for the investigations of CAD. This efficient hybrid imaging predicts both the topology and the degree of the coronary lesions. More specifically, PET depicts the spatial distribution of metabolic and biochemical activity in the body, while CT depicts the anatomy of the body (Figure 1.10 d) [35]. Nevertheless, PET-CT is mainly used in clinical oncology.

Chapter 2. Literature review

2.1 Introduction

Coronary Artery Disease (CAD) is the major cause of death worldwide due to the fact that atheromatous plaques are developed inside the coronary vessels, limiting the blood flow to the heart's muscle [36]. In the interest of the cardiovascular treatment strategy and research, several studies deal with the accurate assessment of the coronary lesions by promoting new atherosclerosis imaging techniques, and improving the existing ones. Diagnosis of the coronary lesions, based on the two-dimensional (2D) images, provides various features of the atherosclerosis, such as the degree of stenosis, the plaque composition and the characterization along the coronary arteries. Invasive X-ray (catheter-based) angiography (Invasive Coronary Angiography – ICA) is widely used for the assessment of the coronary luminal silhouette, providing an accurate visualization of the lesions along the coronary tree. In fact, it is still considered the gold standard in clinical decision making and therapy guidance [37].

Nevertheless, X-ray angiography is known to be fundamentally limited in some aspects: In many clinical cases, the cumulative effect of suboptimal projection angles, vessel overlap, foreshortening, tortuosity and eccentricity may all lead to underestimation or overestimation of the

lesion and probably to wrong treatment strategy [38]. As a consequence, several clinical techniques aim to detect and treat the coronary lesions, utilizing information from two or multiple X-ray images or exploiting hybrid imaging techniques such as invasive coronary angiography and intravascular imaging (X-ray angiography-IVUS, X-ray angiography-OCT).

Nowadays, three-dimensional (3D) reconstruction of coronary arteries is an accurate way for the assessment of CAD. Several studies propose novel techniques for the 3D reconstruction of the coronary vessels from X-ray projections (3D Quantitative Coronary Angiography - QCA), providing also a range of geometrical metrics capable to afford a quantitate analysis of the coronary arteries. Indeed, taking into account cross-sections along the 3D realistic model of the vessel, geometrical metrics such as the Reference Vessel Diameter (RVS), the Minimum Lumen Diameter (MVD), the Degree of Stenosis (DS) as well as the Lesion Length (LL) can be proven an accurate estimation of the coronary silhouette. Moreover, it is worth noting that, several companies such as "Pie Medical, Maastricht, The Netherlands", (Available: https://www.piemedicalimaging.com) and "Medis, Netherlands" (Available: https://www.medis.nl) have already released commercial tools in the market for the 3D reconstruction of coronary vessels from X-ray angiographies.

In addition, several works deal with the simulation of the blood flow and the computation of the hemodynamic features in the 3D models of the coronary arteries. Actually, it has been observed that both the blood pressure and the Endothelial or Wall Shear Stress (ESS - WSS) distribution on the vessel affect the plaque growth both *a priori* and *a posteriori* of a heart event such as the heart attack [39]. Moreover, the invasive calculation of the Fractional Flow Reserve (FFR) remains a major factor about the treatment strategy that should be applied in the region on the coronary lesion (e.g. stent application or not). Therefore, the computation of the FFR value, through the process of the blood flow modeling in the 3D models of the coronary vessels, remains an up to date topic for many published studies.

Finally, several studies effort to assess the CAD in bifurcated arteries. Therefore, various methods, based both on the 2D and the 3D coronary analysis, are applied on the coronary bifurcations imaging data in order to evaluate the atherosclerotic lesion in this complex artery's structure. Furthermore, the study of the local blood flow patterns in the region of the coronary bifurcations is an up to date research topic of the cardiovascular engineering.

The aim of this study is to propose a novel method for the 3D reconstruction of the coronary bifurcations using QCA, as well as to highlight the impact of the bifurcation anatomy on the computation of hemodynamic features. Therefore, in this chapter, we present a review of the literature about the proposed methods for the 3D reconstruction of the coronary vessels and we cite some proposed studies which deal with the computation of the blood flow dynamics and the FFR in 3D models of the coronary arteries.

The current chapter is structured as following:

- X-ray angiography enhancement and vessel segmentation
- Two-dimensional (2D) centerline extraction
- Three-dimensional (3D) vessel reconstruction
- Computational blood flow dynamics
- Computational Fractional flow reserve (FFR)
- Aim of this study

2.2 3D Quantitative Coronary Angiography

2.2.1 X-ray angiography enhancement and vessel segmentation

Accurate assessment, visualization and quantification of coronary vessels in X-ray angiographies acts a significant role in cardiovascular treatment therapy and research. Indeed, various medical diagnostic tasks address with the measure of the lumen width, reflectivity, tortuosity and abnormal branching. Moreover, the accurate diagnosis of the coronary stenosis is a high valued task for the determination of the treatment strategy. Image enhancement and segmentation are the only computational methods which cope with this challenge [40].

Despite the fact that several algorithms have been developed to improve the coronary angiography images, few studies have been published in the field of the angiography enhancement. In fact, these algorithms can be used in clinical practice to improve the vessels visualization. Algorithms, such as the piecewise normalization [41] and the rolling algorithm [42], attempting to remove the background structures or to increase the contrast of vessels on the image, are not robust to the signal-to-noise-ratio (SNR) of the angiography. Although, the most X-ray angiographic acquisition systems in the market have integrated algorithms for real time angiography enhancement. Briefly, the acquired image is blurred and subtracted from the original image, creating thus an edge image that contains higher spatial frequency components.

(a) **(b)**

Figure 2.1: a) Enhanced image, b) and initial image [40].

Then, the edged image is multiplied by a user specified level gain and fused with the initial image to engender an enhanced image [43] (Figure 2.1). Furthermore, image registration techniques are applied on the angiographies for the detection of the non-vascular artifacts while certain warping methods are implemented to mask images. Finally, the registrated images are subtracted from each other to result in an enhanced angiography [44].

Image segmentation defined as: the process where the region of interest (ROI) is segmented from the rest image using a fully automated or a semi-automated methodology. In the current study the region of interest defined as: a part of the coronary tree (coronary segment or coronary bifurcation) which is depicted on the X-ray angiography, while segmentation defined as: the two-dimensional detection and isolation of the coronary vessels (foreground) from the rest image (background). This process constitutes the first step of the 3D reconstruction algorithm and it is the leading step for the accurate 3D modeling of the coronary vessels. Several published studies address the 2D vessel segmentation. We classify them relatively to the method that they implement for the vessel segmentation, as: image processing, pattern recognition, model-based tracking and propagation, neural networks, fuzzy and artificial intelligence – based methods [45-57].

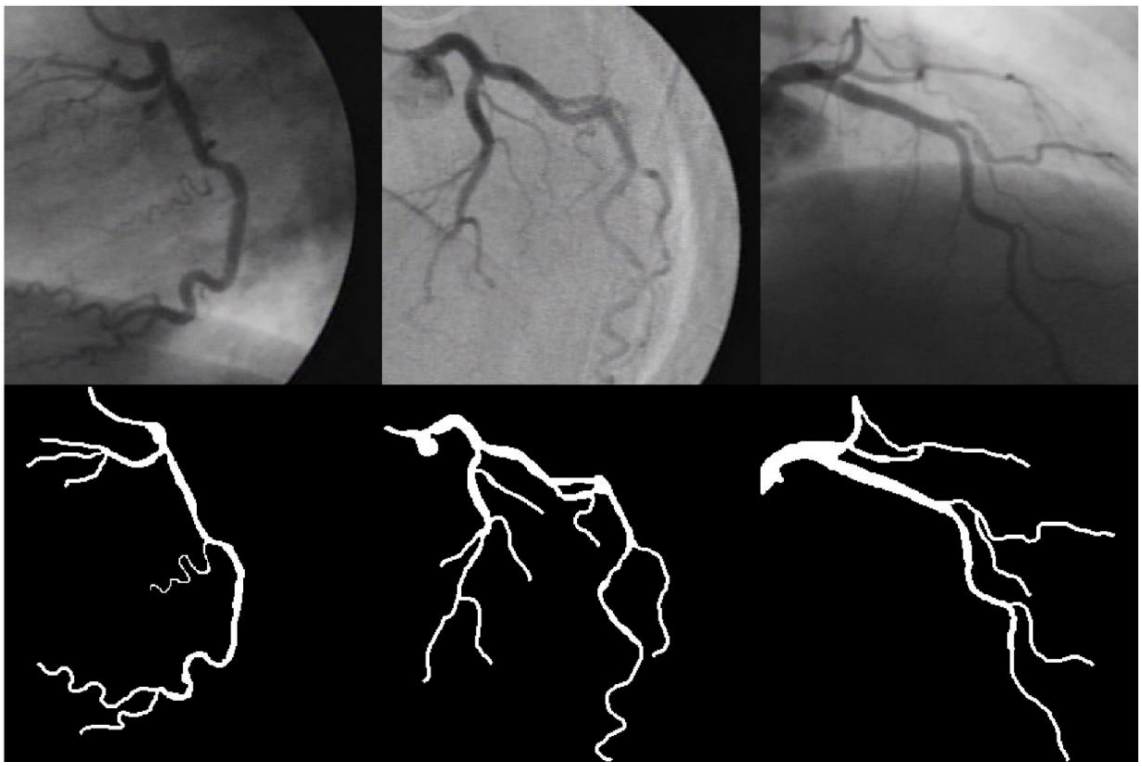

Figure 2.2: Gaussian matched filters (GMF) [57].

Cruz-Aceves *et al.* [57] presented a comparative analysis of four nature inspired algorithms to improve the training stage of a coronary angiography segmentation strategy using Gaussian matched filters (GMF). Briefly, genetic algorithms (GAs) were used to select parameters of the Gaussian matched filters for blood vessel detection while differential evolution (DE) methods were used to optimize the filtering procedure. Considering a validation set of 40 angiograms, the GMF-DE method demonstrated decent accuracy (r = 0.9402) (Figure 2.2).

Lee *et al.* [54] proposed an intensity-vesselness Gaussian mixture model (IVGMM) tracking for 2D segmentation of coronary arteries over a 2D X-ray angiography image sequence. Each of the foreground (vessels) and the background (salient objects) was represented by a Gaussian mixture model (GMM) that is widely used in various object tracking algorithms. The characterization on the Gaussian mixture model was achieved using information from a 2D vector of features based on the pixels intensity and a novel vesselness technique, which is based on the composition of the Frangi vesselness [55] and Krissian medialness [56] filters. Moreover, the proposed method is dynamic due to its upgrade after its implementation on each X-ray image.

Comparing the Frangi's vesselness method, IVGMM presents better recall (r_{IVGMM} =0.794, r_{FRANGI}=0.555) and equal p value ($p_{IVGMM} = p_{FRANGI}$ =1) (Figure 2.3).

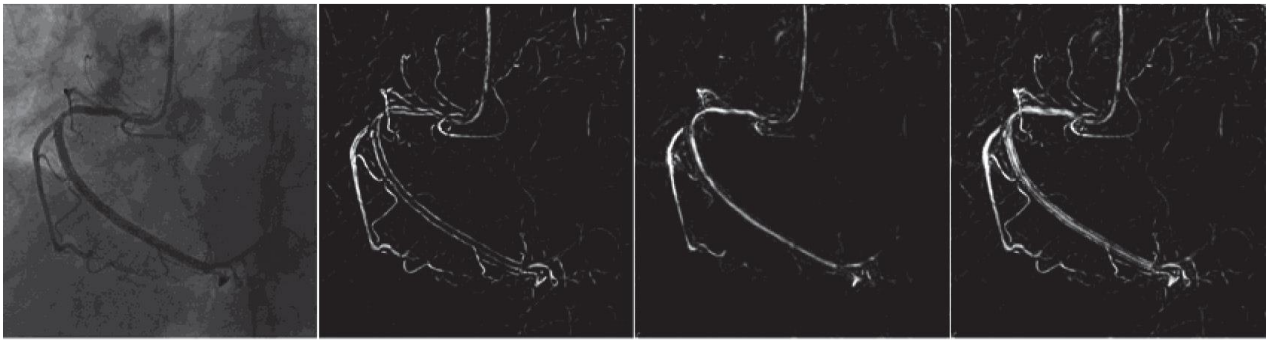

(a) **(b)** **(c)** **(d)**

Figure 2.3: An example of vesselness filters: a) Original image, b) Frangi's vesselness, b) Krissian's vesselness and c) Lee's vesselness [54].

Klein *et al.* [45] presented a deformable spline algorithm for determining vessel boundaries, and enhancing their centerline features on X-ray angiography. Initially, edge detection method was implemented on the angiography, revealing any lumen boundary. B-spline snakes were used for the connection and representation of the lumen boundaries, while dynamic programming was used to configure the control points of the spline, increasing thus the snake complexity needed to achieve lumen segmentation. Klein's method was validated on phantom vessels at the base of geometrical measurements, presenting decent performance.

2.2.2 2D centerline extraction

2D centerline extraction is defined as: the skeletonization of the coronary vessels on the coronary angiography image. However, it has proven to be a challenging task due to the limitation of the X-ray angiography to depict the anatomy of the coronary tree in details. Indeed, multiple coronary branches are overlapped each other, hiding many coronary arteries aspects such as the bifurcation points. Therefore, various published methodologies overcome these problems, calculating successfully the 2D centerline of the coronary vessels.

Auricchio *et al.* [53] deal with the coronary bifurcation artery segmentation and centerline extraction in X-ray angiography using image processing techniques. Initially, the user applies a "pseudo-centerline" manually along both the main and the side branch of the bifurcated vessel. A filtering operation is applied on the angiographies to adjust the intensity values of the pixels,

increasing thus the contrast of the original images. Noise artifacts are removed from angiographies by implementing both Gaussian and Laplacian filtering operations on them. Then, an edge detection method (image gradient) is performed on the images, exposing any boundary of the inner walls. Perpendicular lines along the "pseudo-centerline" cross the boundaries of the lumen walls, revealing the vessel silhouette. Finally, the true centerline is defined as the mean points between the cross points of the lumen boundaries along the vessel (Figure 2.4).

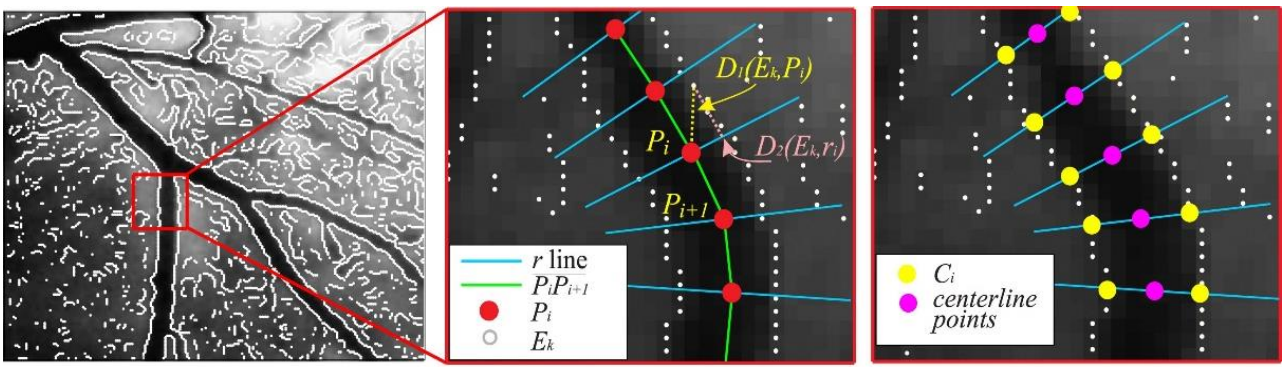

Figure 2.4: a) Edged image, b) pseudo-centerline application, c) 2D cross-section extraction [53].

Both in 2008 and 2016, Zifan *et al.* [58, 59] presented a method for the coronary tree centerline extraction. Initially, both vessel enhancement and segmentation techniques were applied on the coronary angiography. After detecting the intersecting and end points of the branches along the coronary tree, a vessel thinning method [60] was performed on image for the centerline extraction (Figure 2.5).

Figure 2.5: a) Definition of the bifurcation points on angiography, b) 2D centerline extraction [58].

2.2.3 3D reconstruction

The 3D reconstruction of the coronary arteries from CA projection views is based on the implementation of the back-projection algorithm. Specifically, there are two back-projection methods: i) the methods which are based on 2D feature matching, and ii) the methods which are based on back-projection of vesselness responses [61].

The first category of the back-projected methods is based on the 3D matching of related vessels features from multiple X-ray angiographies, such as lumen boundaries, centerlines, start/end and bifurcation points, in order to reconstruct the 3D coronary artery geometry. Moreover, this method was designed to work with non-calibrated systems because the estimation of geometry parameters that relate the projection angiographies can be easily integrated into it. One way to reconstruct the arterial tree is to establish correspondences between the centerlines of biplane angiographies using geometric parameters such as bifurcation points [62-66] (Figure 2.6 a). Another way is to divide the 3D space into parallel planes and to assign each centerline point of the reference view to one of the depth levels using spatial information from multiple X-ray angiographies [67, 68] (Figure 2.6 b).

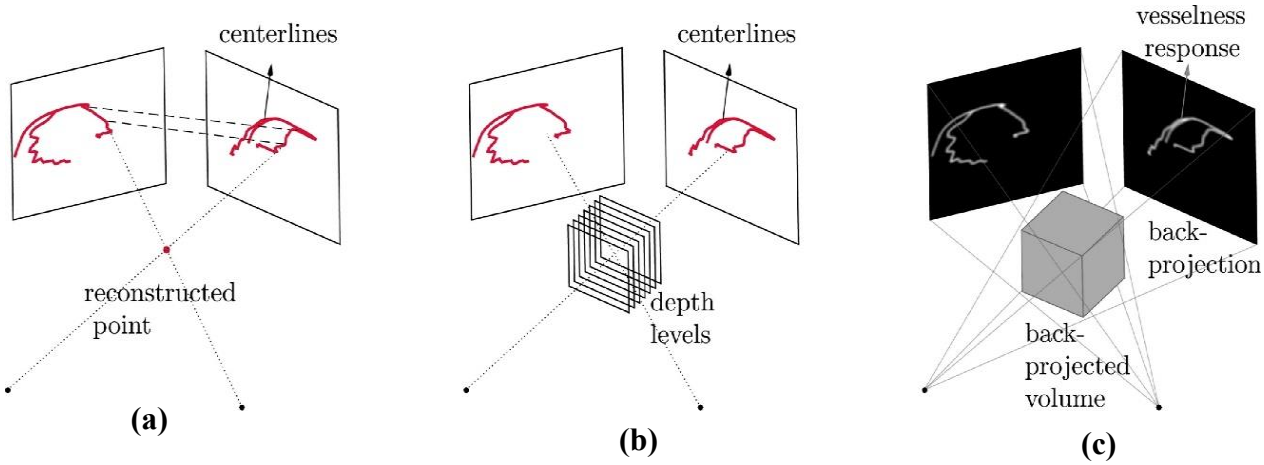

Figure 2.6: Summary of back-projection based methods: a) Methods based on 2D feature matching establish correspondence of centerlines from different 2D views and compute the reconstruction using triangulation. b) methods which divide the 3D space into parallel planes representing the depth levels and each centerline point in the reference frame is assigned to one of the depth levels using the information from multiple X-ray images, c) methods based on back-projection of vesselness response compute a 3D volumetric vesselness response from 2D vesselness responses for further processing [61].

In 2009,Yang *et al.* [66] proposed the mathematical modeling of the back projection algorithm which fully utilizes the information of two X-ray views. Taking into account CA imaging data both from phantom and patient angiograms, the vessel centerlines were reconstructed in 3D space with a mean positive accuracy of 0.665 mm and back projection error of 0.259 mm. Six years later, Cong *et. al.* [69] improved the Yang's work, proposing a novel method for the cross-sectional plane calculation using multiple angiographic views. Considering the X-ray angiography as the "gold standard", Cong's method was validated by calculating the re-projection error.

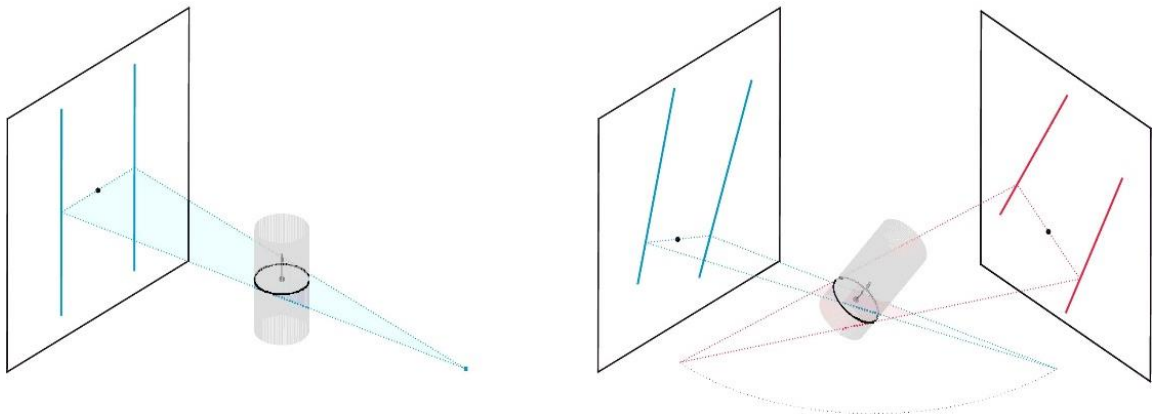

(a) **(b)**

Figure 2.7: 3D reconstruction based on a) a single angiographic view, b) two angiographic views [61].

On the other hand, back-projection of vesselness responses methods does not utilize any image geometry information. Initially, a vesselness filtering is applied on X-ray angiographic views, extracting the vessel response. For this reason, several studies focus on vesselness filtering such as Frangi's study. [55]. Then, the extracted vessels spatial responses of the multiple X-ray views are back projected to obtain the 3D volumetric vessel response [70-73]. Nevertheless, the 3D vessel responses are generally very noisy and robust pre-processing methods, such as vessel enhancement and segmentation, are required. For example, Jant *et al.* [73] extract the 3D voxels that belong to the vascular structure using fast marching approach along the 3D centerline. The algorithm was evaluated both on simulated projections of virtual phantom and clinical imaging data, showing effectiveness (Figure 2.8).

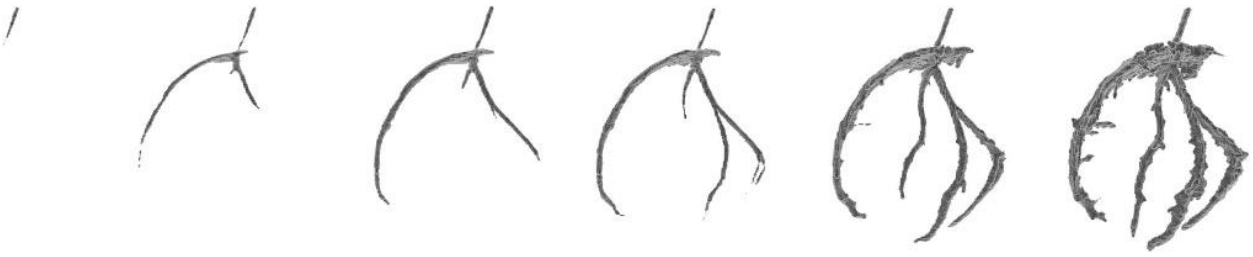

Figure 2.8: 3D reconstruction based on the back-projection of the vesselness response. Visualization of the fast marching process at six different iteration points [73].

2.3 Blood flow modeling

2.3.1 Computational blood flow dynamics

The blood flow patterns hold a significant role in the atherosclerosis progression. Actually, various hemodynamic aspects increase the concentration of the atheromatic plaque in the region of the lesion or provoke detach of the existed plaque and probably a new artery occlusion. Several *in-vivo* experimental studies address the association between the blood flow and blood velocity [74, 75]. Moreover, Ku *et al.*, [76] as well as Zarin *et al.*, [77] used phantoms of the carotid arteries to prove that the low and oscillatory Endothelial Shear Stress (ESS) values along the vessel are correlated with plaque growth.

Nowadays, several studies address the simulation of the blood flow in the 3D models in order to study the hemodynamic features of the human arteries. However, this computational process requires both the accurate reconstruction of the artery's 3D geometry and the suitable definition of the initial boundary conditions. Regarding the 3D geometries of the arteries, coronary vessels have been extracted both from invasive or non-invasive medical imaging data such as X-ray angiography, OCT, IVUS, CT, MRI, as this has been mentioned in previous sections. Regarding the boundary conditions, blood velocity and pressure profiles are mainly used in the inlet and the outlet of the 3D model while the geometry's walls are considered rigid and no-slip. For example, Mohammadi *et al.* [78] proved that the inlet boundary conditions depend on the degree of stenosis, while in severe stenosis the velocity based boundary conditions could not be trueful. On the contrary, the upstream pressure was constant, and thus it could be used as an inlet boundary condition. Most of the studies assume that both in large and medium arteries (coronary arteries) the blood behaves as a Newtonian fluid having constant viscosity, while the blood flow is laminar and incompressible. Nevertheless, in many studies, the viscosity of the blood is assumed as

dynamic (non-constant) which leads to non-Newtonian behavior of the blood into the vessels [79]. Finally, the blood flow modeling requires the solution of the three-dimensional (3D) transient Navier-Stokes equations using the finite elements approach [80, 81] both for the blood and the arterial wall.

Li *et. al.*, [82] examined the impact of the side branch on computational of ESS in coronary artery disease. Actually, blood flow simulations were performed on 21 hybrid 3D models extracted from X-ray angiography and OCT images. The results show that there are significant hemodynamic differences between the 3D models which included the side branch versus the 3D model without the side branch (Figure 2.9).

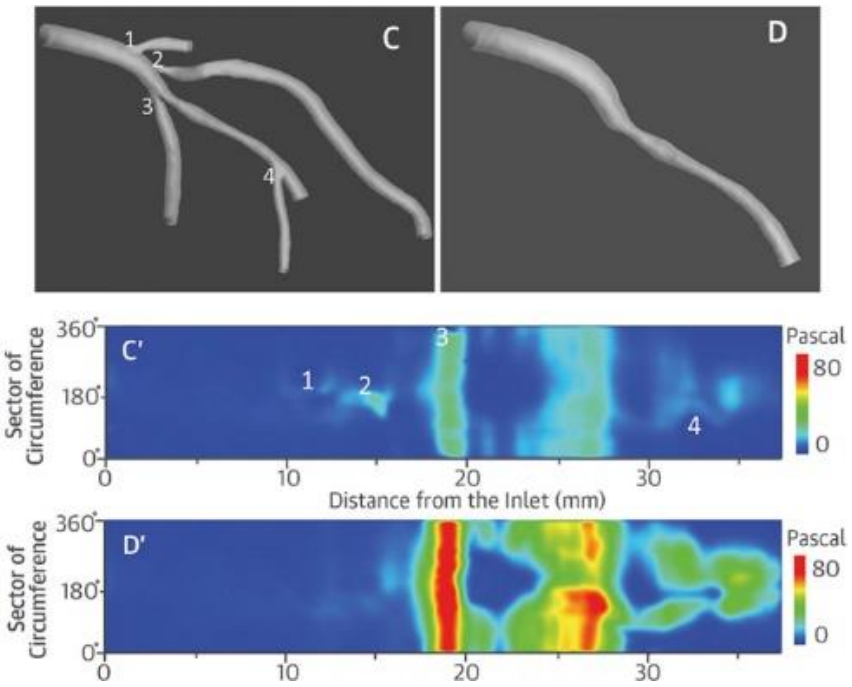

Figure 2.9: The impact of the side branch on the computational ESS in coronary arteries [82].

Sakellarios *et. al.*, [83] examined the effect of the side branches on the hemodynamics and the potential prediction of atherosclerotic plaque development as well as the best flow division model for accurate blood flow modelling. Using CTA images, 17 coronary artery bifurcations cases were reconstructed in 3D space. Using the Murray's law, firstly, blood flow simulations were performed on the coronary bifurcations and secondly, on the coronary segments omitting the side branch. The work concluded that the ESS distribution in coronary models, including the side branches, allows

more accurate prediction of atherosclerotic evolution than the ESS estimated in models including only the main branch of coronary bifurcations.

Papafaklis *et. al.* [84] studied the blood flow dynamics in coronary bifurcation arteries and examined the correlation of the arterial wall thickness with the ESS distribution on the vessel. A few years later, the authors [85] investigated the influence of the ESS to vessel restenosis in patients who have undergone stent implementation.

2.4 Computational Fractional Flow Reserve (FFR)

Intracoronary hemodynamics measurements, such as blood flow and pressure, can directly be assessed during percutaneous coronary intervention (PCI) using sensor-equipped guide wires. The most common measurement in daily clinical practice is the Fractional Flow Reserve (FFR), which provides an accurate assessment of coronary stenosis severity [86, 87]. It is defined as the ratio between the mean distal stenosis and mean aortic pressure during maximal hyperemia [88]. Unfortunately, this invasive measurement is dangerous for the patient because the entry of the wire into the coronary arteries could limit furthermore the blood flow to the heart, causing thus a new heart event (heart attack). Computational Fluid Dynamics (CFD) has been demonstrated to be an effective tool to study the FFR of the coronary lesions, allowing to investigate multiple scenarios of different anatomy and flow conditions. Several up to date studies deal with the computational assessment of the FFR in realistic 3D geometries of the coronary arteries. Most of them consider only the coronary segments (main branch), while even few studies investigate the influence of the bifurcation anatomy on the intracoronary hemodynamics, including pressure drop and FFR of side branch lesions.

Tu *et. al.* [89] computed the FFR value in 77 vessels of 68 patients. Initially, the geometries of the vessels were reconstructed in the 3D space using the QCA method and the mean volumetric flow rate at hyperemia was calculated. Computational fluid dynamics were applied subsequently with Tu's novel strategy for the computation of FFR. Assuming the wire-based FFR as the reference gold standard, the proposed FFR_{QCA} shown decent accuracy ($r=0.81$, $p<0.001$).

Moreover, Liu *et. al.* [90] examined the impact of image resolution on computation of FFR. Briefly, the FFR value was computed considering both QCA-based and CT-based 3D models of the same patient. Taking into account 57 vessels from 41 patients was observed decent correlation between FFR_{QCA} and FFR_{CT} ($r=0.71$, $p<0.001$).

2.5 Aim of this study

The majority of the reported works either propose methodologies for the 3D reconstruction of coronary arteries from medical imaging data, or examine the blood flow dynamics considering the 3D geometries which have been extracted from commercial software products (i.e. CAAS QCA 3D of Pie Medical or QAngio XA of Medis). In this thesis we introduce a novel methodology for the 3D reconstruction of the coronary arteries using the 3D QCA approach and we simulate blood flow in the produced 3D vessels, developing thus a complete study about the cardiovascular coronary modeling. We focus on the coronary bifurcations, studying both 3D anatomy and the hemodynamic factors of them which can lead to atherogenesis. Finally, the clinical wire-based measurements were considered the ground truth for the entire study to evaluate the computational FFR. The flow chart of Figure 2.10 depicts the methodological framework summarizing the workflow of the study.

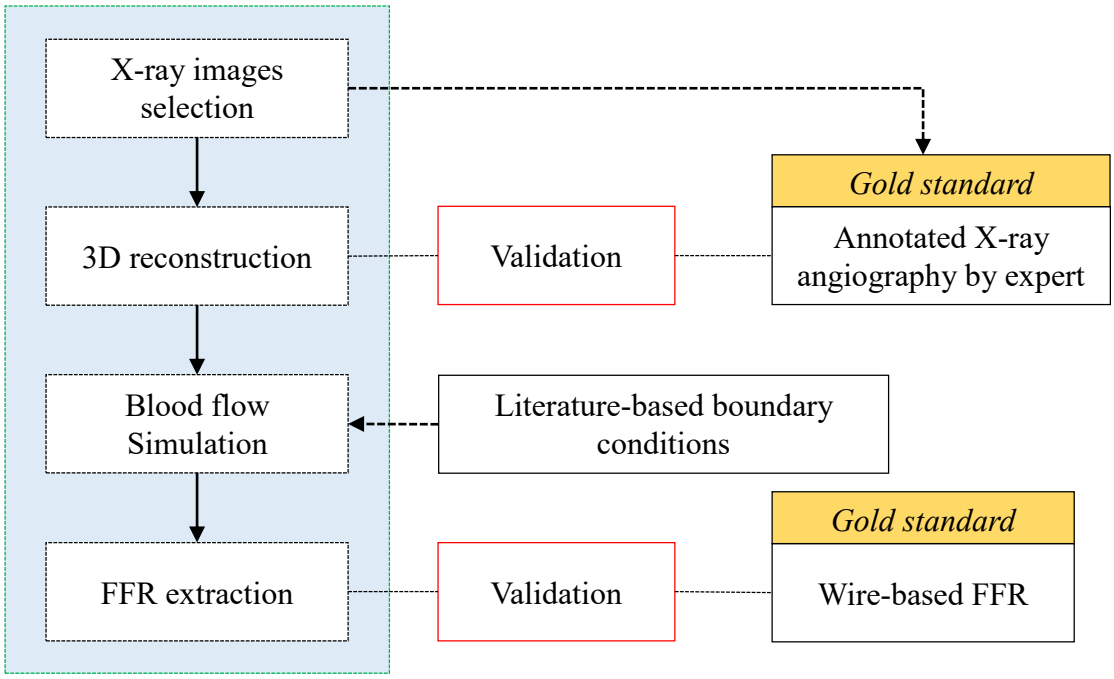

Figure 2.10: Flow chart of our work .

Chapter 3. Materials and methods

3.1 X-ray angiography acquisition

Before introducing our method for the 3D reconstruction of the coronary bifurcations, it is worth to explain how an X-ray angiography acquisition system works. The 3D reconstruction method is a realistic representation of the conditions under which the multiple images have been acquired. An gantry-based system, called C-arm (Figure 3.1), performs a continuous rotation around the patient chest, allowing the physician to focus on coronary vessels from different angles of the projection views [91]. In the one side of the C-arm system a source is placed, which emits X-ray beam and on the opposite side a detector system is located which receives the ionized X-ray beam and generates the angiographic images. The patient plane is defined by the isocenter of the imaging device and slices through the patient such that is perpendicular to the sagittal plane of the body. Initially, zero-degree rotation of the C-arm is referenced to the origin perpendicular to the chest of the patient. The primary axis of C-arm rotation is defined at the intersection of the patient plane and the sagittal plane. The positioner primary angle is defined the transaxial plane at the isocenter

with zero degrees in the direction perpendicular to the patient's chest where + 90° corresponds to the left hand side (left anterior oblique -LAO) and -90° corresponds to the patient's right hand side (right anterior oblique - RAO), while the valid range of primary positioner angle is -180° to 180°. The secondary axis is in the patient plane and is perpendicular to the primary axis at the isocenter. The positioner secondary angle is defined in the sagittal plane at the isocenter with zero degrees in the direction perpendicular to the patient's chest where +90° corresponds to the patient head side (cranial angulation - CRA) and -90° corresponds to the patient's legs (caudal angulation - CAU), while the range of the secondary positioner angle is -90° to + 90° (Figure 3.2). Regarding the dual – axis rotational coronary angiography (DARCA), the C-arm gantry could be placed either in the head position (HP) or in the side position (SP) of the patient [92, 93]. All DARCA acquisitions in this study were performed from the head position of the C-arm gantry. Contrast between vessels and other tissues is achieved through the different absorption of X-ray photons that characterizes the tissues while the number of the projection views depends on the modal acquisition which is located on the rotational angle of the C-arm.

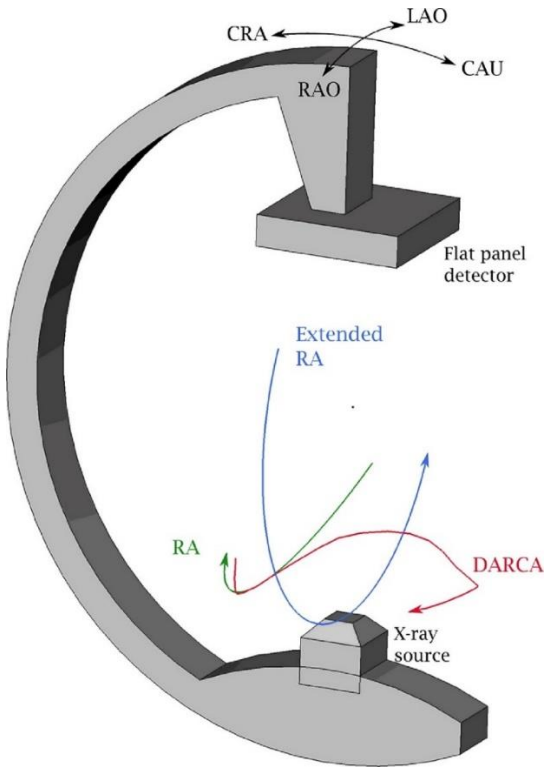

Figure 3.1: C-arm gantry.

In this context Digital Imaging and Communications in Medicine format (DICOM) images constitute our study's dataset. Usually, an angiographic DICOM file contains images that have been recorded with a typical frequency of 15 frames per second. Each frame of this sequence represents a projection of the coronary vessels onto a single-plane system. The images are correlated with the electrocardiographic (ECG) signal to allow thus the qualitative vessels visualization during the cardiac cycle [94]. Except from the patient's data, each DICOM file is enriched with extra information such as the image acquisition setting of the X-ray device (DICOM Tags) which contain the distance source to object-patient (SOD), the distance source to image intensifier (SID), the intensifier size and the intensifier resolution (rows and columns) as well as the primary (LAO, RAO) and the secondary (CRA, CAU) rotation angles. During the X-ray angiography acquisition the patient table movement is minimized by an iso-centering procedure [95]. The flat detector motion is characterized by a constant SID and iso-center value in order to establish a pointwise correspondence between two angiographic projection views [96].

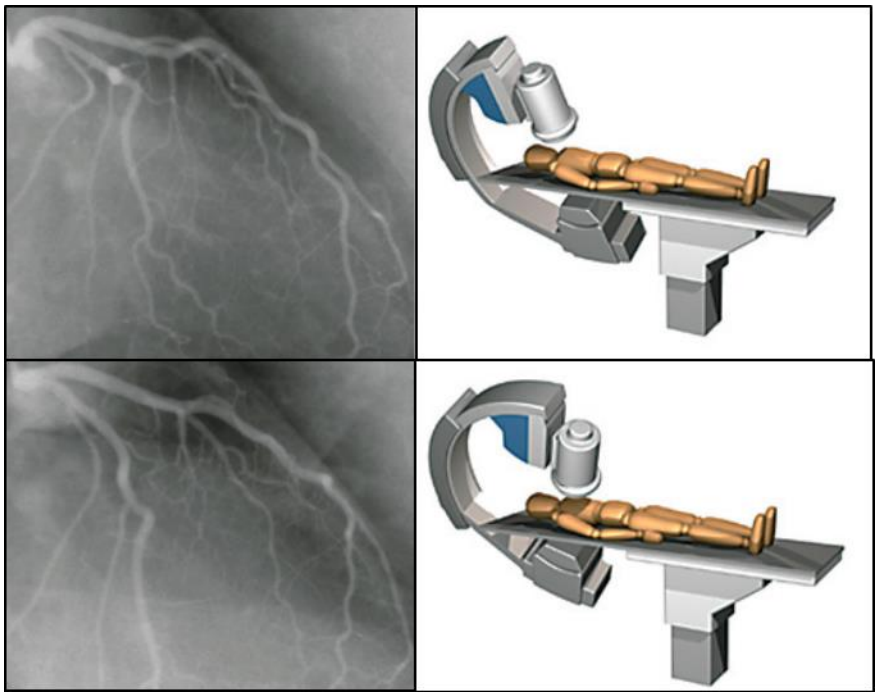

Figure 3.2: Angiographic views based on different rotation angles of the C-arm gantry.

3.2 Image selection

For the 3D coronary reconstruction of a coronary bifurcation two projection views at the same cardiac phase are selected manually from the angiographic sequences. The two projection must have varying LAO – RAO and CRA – CAU angle value as follows [39]:

$$\angle I_1 - \angle I_2 \geq 30^{\circ} . \tag{3.1}$$

Actually, for each sequence of the angiographic images, the user manually selects the projection views at the peak of the R wave of the ECG (end-diastolic time) [32]. Figure 3.3 depicts an example of the angiographic projections selection.

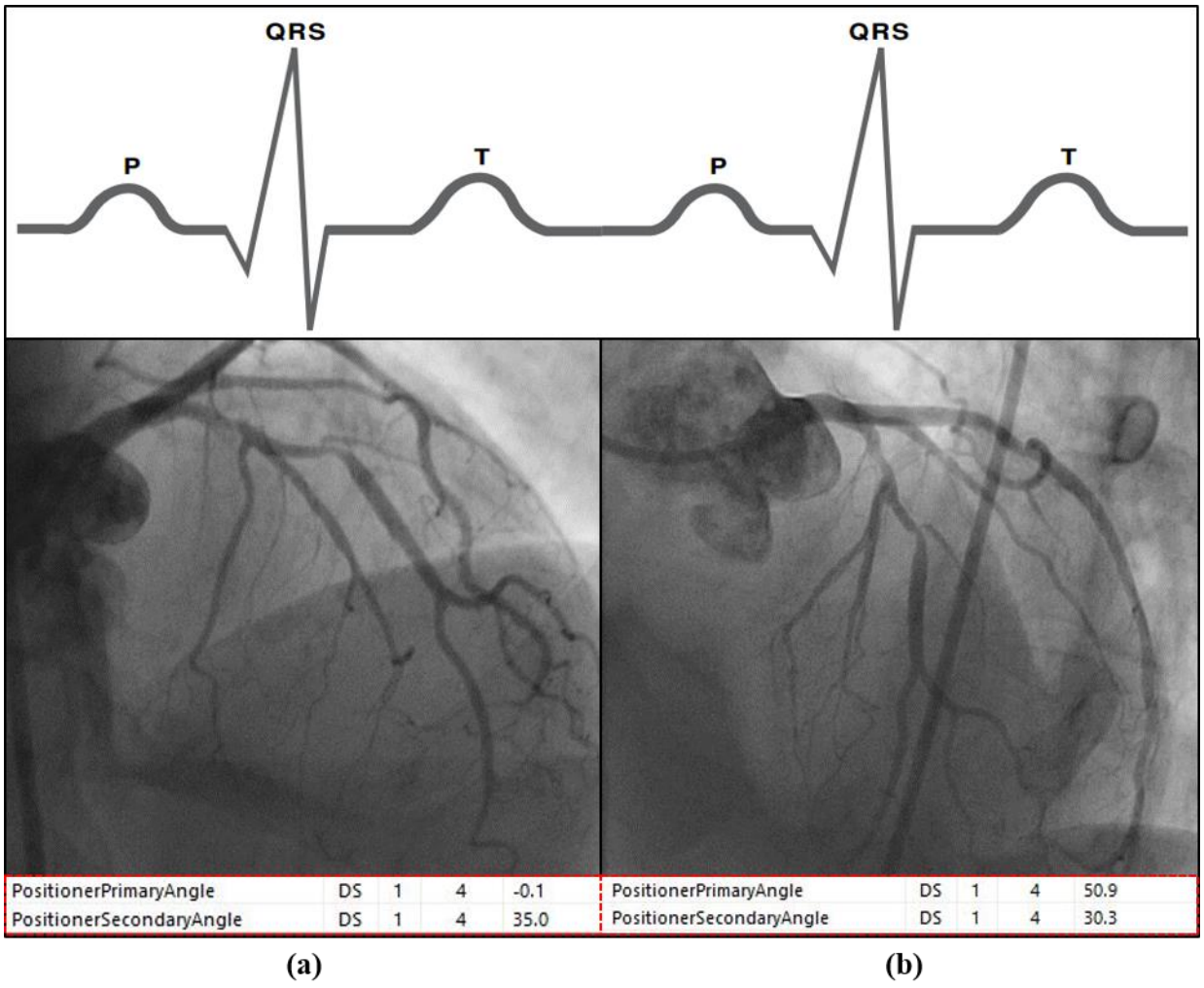

Figure 3.3: Image selection at the R peak of ECG signal a) first angiographic view, b) second angiographic view.

3.3 Preprocessing

The difficulty to analyze the X-ray angiography comes from the low image contrast due to emitting a minimum dose of radiation to the patient. Additionally, the high contrast of anatomical structures such as bones could create shadows on the angiography and make the vessels investigation even harder. Consequently, the preprocessing step is necessary to improve the quality of the angiographic images in order to achieve accurate vessel segmentation and 3D reconstruction. Thus, in the current study the image enhancement was performed by applying specific filtering processes on the initial X-ray projection views $I_1(x,y)$ and $I_2(x,y)$. The preprocessing consists of the following filtering strategy [40] (Figure 3.4):

1. Contrast enhancement,
2. Additional white Gaussian noise (AWGN) removal,
3. Edge detection.

Regarding the contrast enhancement process, the histogram equalization method was applied on both angiographies in order to adjust the intensity values of the pixels. Briefly, assuming that the initial intensity values of the pixels can distributed on a histogram, the current filtering operation produces an output image which has an approximately flat histogram and enhanced image foreground.

The noise was removed from the angiographic images by applying a Gaussian filtering [97] operation. Assuming that the white noise has a Poisson or Gaussian distribution, a 5x5 moving average filter was designed:

$$h(x,y) = \frac{1}{2\pi s^2} e^{\frac{-[(x-x_c)^2+(y-y_c)^2]}{2s^2}}, \tag{3.2}$$

Where h is the spatial response of the filter, x_c and y_c are the coordinates of the mask center and $s = 0.5$ is the standard deviation.

Finally, the edges of the vessels were detected by applying the canny algorithm [97]. This algorithm computes the gradient in any neighborhood of pixels by applying a moving coefficient mask on the image. As a result, the horizontal, the vertical and the diagonal edges of the vessels are revealed.

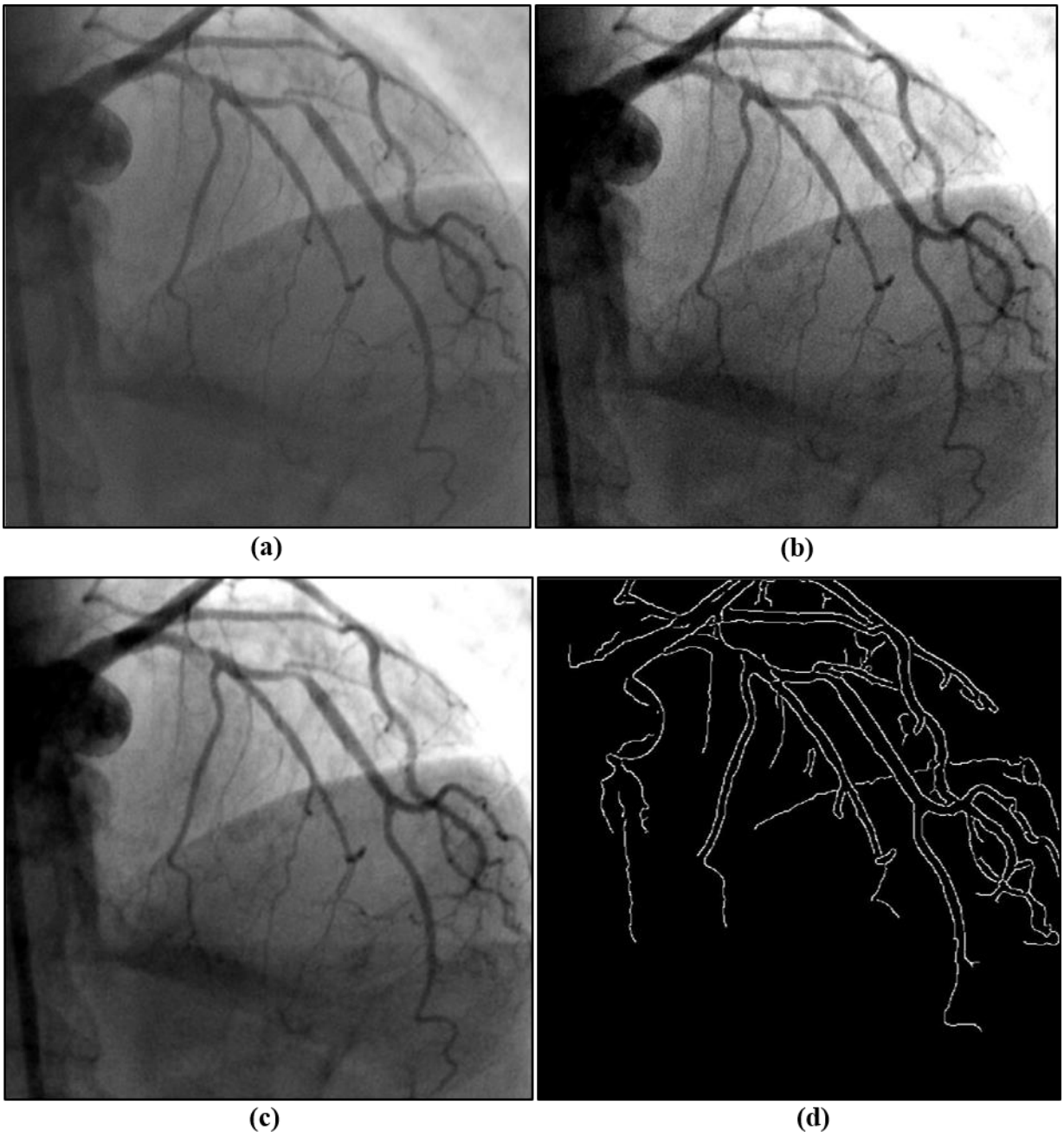

Figure 3.4: Preprocessing stages: a) the initial image, b) the image after the histogram equalization process, c) the image after Gaussian filtering, d) and the edged image.

3.4 Vessel segmentation

The current study suggests a semi-automated methodology for the assessment of the coronary bifurcation lumen utilizing both projection views. Actually, the level of method automation depends highly on the quality (foreground contrast) of the initial angiographies. The current vessel segmentation methodology consists of two main tasks:

1. User-defined points around the region of interest (ROI)
2. An automated algorithm for the bifurcation vessel segmentation

Initially, the user defines some points manually on both angiographies, providing thus a non-strict annotation of the vessels silhouette. Considering a bifurcated vessel, totally 4 lumen borders are annotated by the user on each angiographic projection (two for the main branch and two for the side branch). The number of the user-defined points (denoted as $U_k, k = 1,...,h$) depends on the vessels anatomical complexity, while the start and the end point must correspond to the two vessel landmarks (i.e. bifurcations along the coronary tree), clearly visible in both angiographic views. Assuming an angiographic projection view where the coronary vessels are overlapped each other, the user should define enough points on image in order to figure out the lumen borders. On the contrary, less points by user are required when the arteries anatomy is clearly visualized on the angiography. In any case the user-annotation of the bifurcation area have to be well specified.

Regarding the automated part of the current methodology, a minimum cost path-based method [98] is performed for the accurate segmentation of the vessel lumen along the pre-defined points ($U_k, k = 1,...,h$). Taking into account both the edged image of the previous section (Figure 3.4 d) and the user-defined points, we implement the fast-marching approach to segment the lumen border in $h-1$ steps.

Assuming a pair of points $U_k, U_{k+1}, k = 1,...,h$ of the pseudo-annotation sequence, the algorithm defines:

- U_k as the starting point of the path
- U_{k+1} as the ending point of the path
- It computes the Euclidian distance transform of the edged binary image.

For each pixel, the distance transform assigns a weight ($W_{r,c}\ r = 1, \ldots, 512, c = 1, \ldots 512$) which is the distance between that pixel and the nearest non-zero pixel of the image. It is worth noted that zero-pixel values correspond to black color while non-zero ones correspond to the white color of a binary image. The fast-marching algorithm [99] is implemented on the weighted image in order to extract the minimum cost-path which corresponds to the lumen border between the points U_k and U_{k+1} (Figure 3.5). Finally, the full lumen border is defined by a default number of points ($NP = 100$).

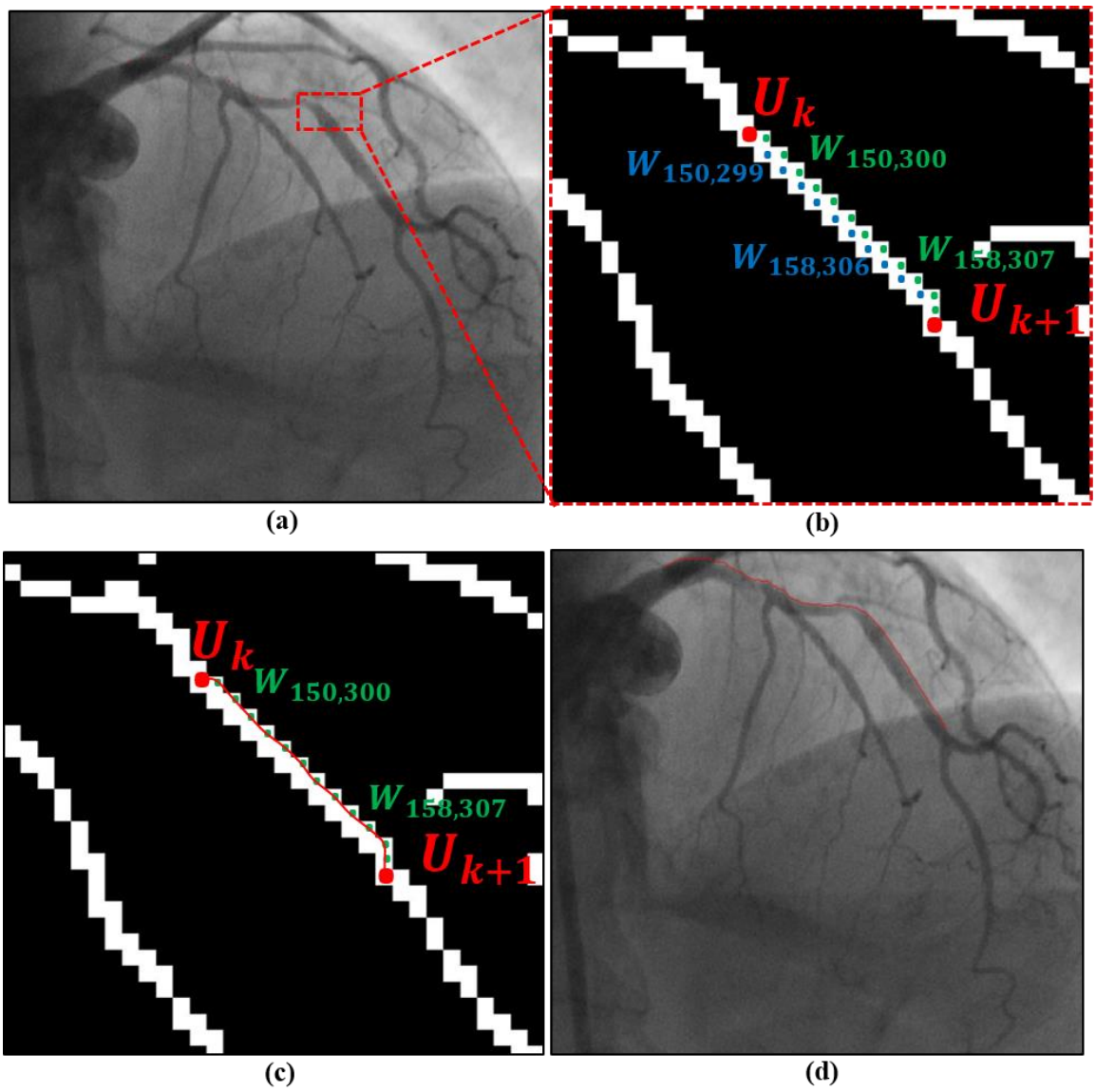

Figure 3.5: Vessel segmentation procedure: a) initial image, b) definition of weights on the edged image, c) minimum cost path calculation, d) extraction of the lumen border.

3.5 2D centerline extraction

During the previous step, four equal length vectors, corresponding to the lumen border of each angiographic view (I_1, I_2), were extracted: two for the main branch (BM_{left}, BM_{right}) and other two for the side branch (BS_{left}, BS_{rigrt}) of the coronary bifurcation artery. In this step we initially calculate the two-dimensional (2D) centerline segmentally for each coronary vessels as follows:

$$\begin{aligned} C_{MB} &= \left(BM_{left} + BM_{right} \right) / 2, \\ C_{SB} &= \left(BS_{left} + BS_{right} \right) / 2, \end{aligned} \tag{3.3}$$

where C_{MB} is the centerline of the main branch and C_{SB} is the centerline of the side branch while element-wise operations occur between the vectors (Figure 3.6 a, b, d, e). Moreover, due to the fact that the extracted bifurcated centerlines are not smooth, a spline method is applied on them. For example, assuming that the centerline curve of the main branch is a polygonal path which contains the finite number of points $C_{MB}, i = 1,...,n$, the spline method yields:

$$\begin{aligned} C_{MBs} &= spline(C_{MB}), \\ C_{SBs} &= spline(C_{SB}), \end{aligned} \tag{3.4}$$

where C_{MBs} is the smoothed centerline curve of the main branch and C_{SBs} is the smoothed centerline curve of the side branch, which correspond to the first angiographic view (Figure 3.6 c). For each projection we define the Bifurcation Reference Point (BRP) as the intersection point between the centerlines of the coronary branches (Figure 3.6 c, f):

$$\begin{aligned} BRP_{I_1} &= \text{intersection}(C_{MBs\_I_1}, C_{SBs\_I_1}), \\ BRP_{I_2} &= \text{intersection}(C_{MBs\_I_2}, C_{SBs\_I_2}), \end{aligned} \tag{3.5}$$

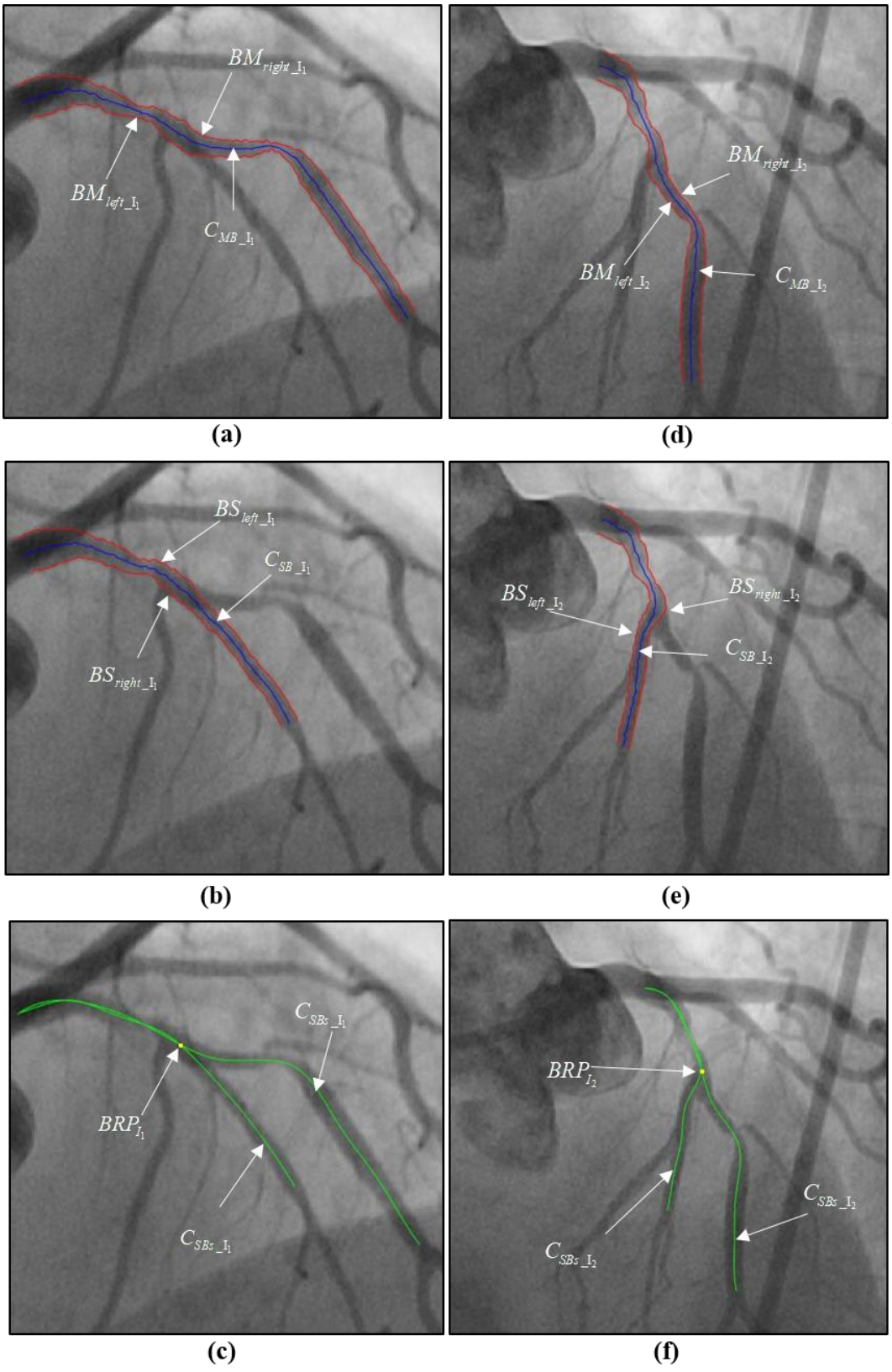

Figure 3.6: Centerline extraction process: a-c) first view, d-f) second view.

3.6 2D Quantitative Coronary Analysis (QCA)

To identify the 2D lumen diameter, we compute the cross-section of the lumen, along the smoothed centerline of the vessel (Figure 3.7). For example, considering the extraction of the lumen diameter of the main branch corresponds to the first angiographic view ($C_{MB\_I_1}, BM_{\text{left\_I}_1}, BM_{\text{left\_I}_1}$) we perform:

Initially, for each $i-th$ point of the centerline $C_{MB\_I_1}(i), i=1,...,n-1$ we compute an edge $\overline{P}$ crossing the $C_{MB\_I_1}(i)$ and perpendicular to the edge $\overline{C_{MB\_I_1}(i)C_{MB\_I_1}(i+1)}$.

Given $\overline{P}$, we compute the two following distances (radius):

$$\begin{aligned} r_{right}(i) &= d(\mathrm{C}_{MB}(i),\, p_1), \\ r_{left}(i) &= d(\mathrm{C}_{MB}(i),\, p_2) \end{aligned} \quad i=1,...,n-1 \tag{3.6}$$

where

$$\begin{aligned} p_1 &= cross(\overline{P}, BM_{right\_I_1}), \\ p_2 &= cross(\overline{P}, BM_{\text{left\_I}_1}). \end{aligned} \tag{3.7}$$

Then we calculate the $i-th$ Lumen Diameter (LD) value as follows:

$$\mathrm{LD}_{MB\_I_1}(i) = (r_{right}(i) + r_{left}(i)) \cdot \mathrm{PS},\ i=1,...,n-1. \tag{3.8}$$

Performing repeatedly the process above, we extracted the lumen diameter of the bifurcated vessel for both angiographies ($\mathrm{LD}_{MB\_I_1}, \mathrm{LD}_{SB\_I_1}, \mathrm{LD}_{MB\_I_2}, \mathrm{LD}_{SB\_I_2}$). Moreover, accounting the Reference Bifurcation Point of each angiography, we classify the bifurcation lumen diameter values into tree individual coronary segments:

- Proximal Main (PM)
- Distal main (DM)
- Side branch (SB)

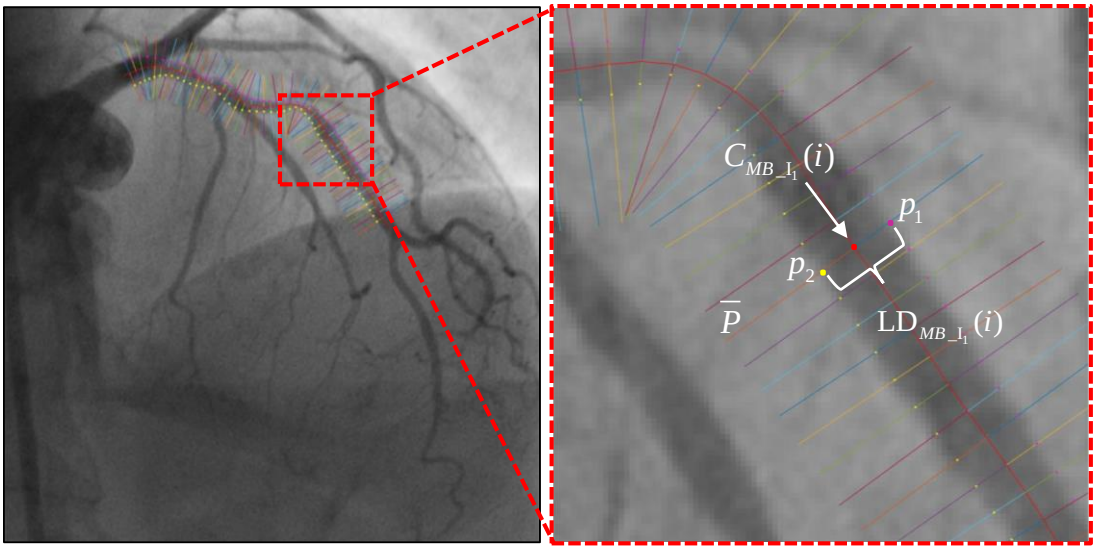

Figure 3.7: 2D quantitative coronary analysis.

3.7 3D bifurcation coronary artery reconstruction

In the previous sections of the current chapter, we described how we retrieved all the necessary geometrical data of the coronary bifurcation from both X-ray angiographic views. In the following section we utilize this 2D information to create the corresponding 3D model of the artery. In fact, we will describe the technique to match all the 2D geometrical features into the 3D space, creating thus the geometry of the vessel. Briefly, the 3D reconstruction process it composed of four main steps:

- Calibration, rotation and translation of the angiographic views,
- 3D centerline reconstruction,
- 3D lumen borders reconstruction,
- Registration of the main and the side branch

In is worth noted that the coronary bifurcation artery was reconstructed segmentally: firstly, the main branch and secondly the side branch. The final 3D bifurcated artery is reconstructed by merging the two branches.

3.7.1 Calibration, rotation and translation of the angiographic views

The core idea of this step is to translate the (x, y) coordinates of each projection view to (u, v, t) coordinates which correspond to the real size of the X-ray image intensifier system as well as the ROA, LOA and CRA, CAU rotation angles of the C-arm around the patient.

Initially, given the image intensified size as well as the image resolution (rows and columns of pixels) we calculate the Pixel Size (PS).

$$PS = \frac{Intesifier\ Size}{image\ resolution}. \tag{3.9}$$

Then, all the 2D information (centerlines and lumen borders), which has been extracted from both angiographic views, are multiplied with the PS, while the middle point of each projection view is assigned on the center of the intensifier grid:

$$I_1 = \begin{bmatrix} x \\ y \end{bmatrix} + \begin{bmatrix} M \\ M \end{bmatrix} \cdot \mathrm{PS}, \mathrm{I}_2 = \begin{bmatrix} x \\ y \end{bmatrix} + \begin{bmatrix} M \\ M \end{bmatrix} \cdot \mathrm{PS}, \tag{3.10}$$

where I_1 and I_2 are the angiographic projections and M is the shift of the middle point of image on the origin of axis:

$$M = \begin{bmatrix} 0 \\ 0 \end{bmatrix} - \begin{bmatrix} image\ resolution / 2 \\ image\ resolution / 2 \end{bmatrix}, \tag{3.11}$$

Figure 3.8 depicts how the calibration of the angiographic projection according to the X-ray intensifier grid.

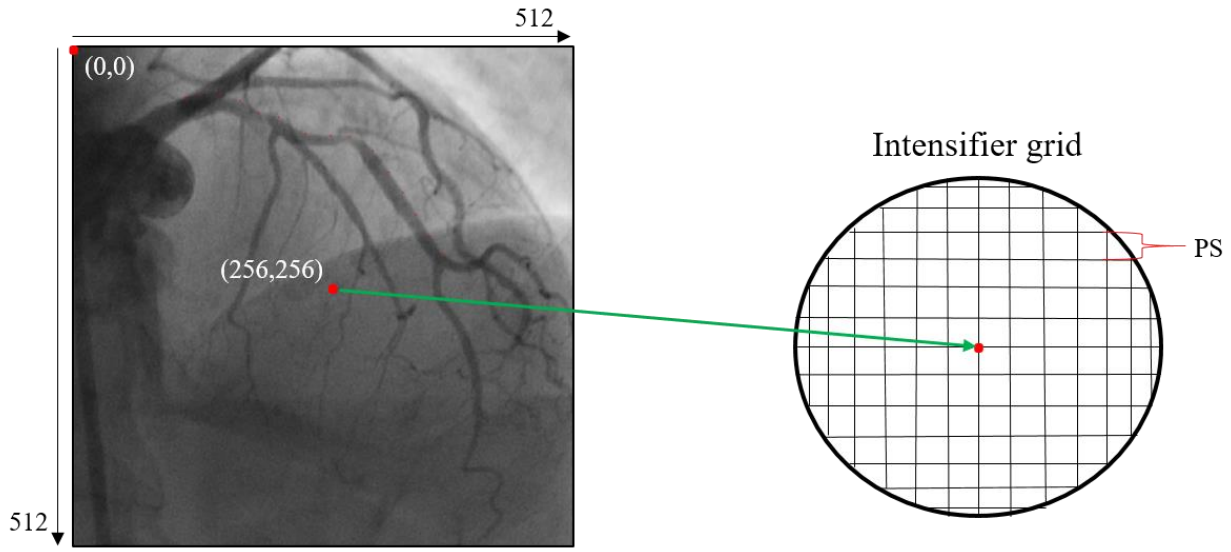

Figure 3.8: Calibration of the angiography according to the intensifier size.

We define the first and the second angiographic views in the global reference system (x, y, z) as follows:

$$I_1 = \begin{bmatrix} x \\ y \\ 0 \end{bmatrix}, \mathrm{I}_2 = \begin{bmatrix} x \\ y \\ 0 \end{bmatrix}. \tag{3.12}$$

In the reference system, which was defined in equation (3.12), the Z-coordinate of both angiographic views is equal to zero. Moreover, we define two points which represent the X-ray source points:

$$S_1 = \begin{bmatrix} 0 \\ 0 \\ 0 \end{bmatrix}, S_2 = \begin{bmatrix} 0 \\ 0 \\ 0 \end{bmatrix}. \tag{3.13}$$

Given the acquisition settings of each angiography: source to object-patient (SOD) and source to image intensifier (SID), we translate the system of equations (3.12) and (3.13) as follows:

$$I_1(z) = I_1(z) - \mathrm{OID} \rightarrow I_1 = \begin{bmatrix} x \\ y \\ 0 \end{bmatrix} + \begin{bmatrix} 0 \\ 0 \\ -(\mathrm{OID}) \end{bmatrix},$$
$$\mathrm{I}_2(z) = \mathrm{I}_2(\mathrm{z}) - \mathrm{OID} \rightarrow \mathrm{I}_2 = \begin{bmatrix} x \\ y \\ 0 \end{bmatrix} + \begin{bmatrix} 0 \\ 0 \\ -(\mathrm{OID}) \end{bmatrix}, \tag{3.14}$$

$$S_1(\mathrm{z}) = S_1(z) + SOD \rightarrow S_1 = \begin{bmatrix} 0 \\ 0 \\ 0 \end{bmatrix} + \begin{bmatrix} 0 \\ 0 \\ \mathrm{SOD} \end{bmatrix},$$
$$S_2(\mathrm{z}) = S_2(z) + SOD \rightarrow S_2 = \begin{bmatrix} 0 \\ 0 \\ 0 \end{bmatrix} + \begin{bmatrix} 0 \\ 0 \\ \mathrm{SOD} \end{bmatrix}, \tag{3.15}$$

where OID is the calculated object to image intensifier distance:

$$OID = SID - SOD\,. \tag{3.16}$$

Considering Θ_1 the primary positioner angle and Θ_2 the secondary positioner angle of the first angiographic view while Θ_3 the primary positioner angle and Θ_4 the secondary positioner angle of the second angiographic view we produce the following rotation matrices:

$$R_{x\_\mathrm{I}_1} = \begin{bmatrix} 1 & 0 & 0 \\ 0 & \cos\theta_1 & -\sin\theta_1 \\ 0 & \sin\theta_1 & \cos\theta_1 \end{bmatrix}, R_{y\_\mathrm{I}_1} = \begin{bmatrix} \cos\theta_2 & 0 & \sin\theta_2 \\ 0 & 1 & 0 \\ -\sin\theta_2 & 0 & \cos\theta_2 \end{bmatrix}, \tag{3.17}$$

$$R_{x\_\mathrm{I}_2} = \begin{bmatrix} 1 & 0 & 0 \\ 0 & \cos\theta_3 & -\sin\theta_3 \\ 0 & \sin\theta_3 & \cos\theta_3 \end{bmatrix}, R_{y\_\mathrm{I}_2} = \begin{bmatrix} \cos\theta_4 & 0 & \sin\theta_4 \\ 0 & 1 & 0 \\ -\sin\theta_4 & 0 & \cos\theta_4 \end{bmatrix}. \tag{3.18}$$

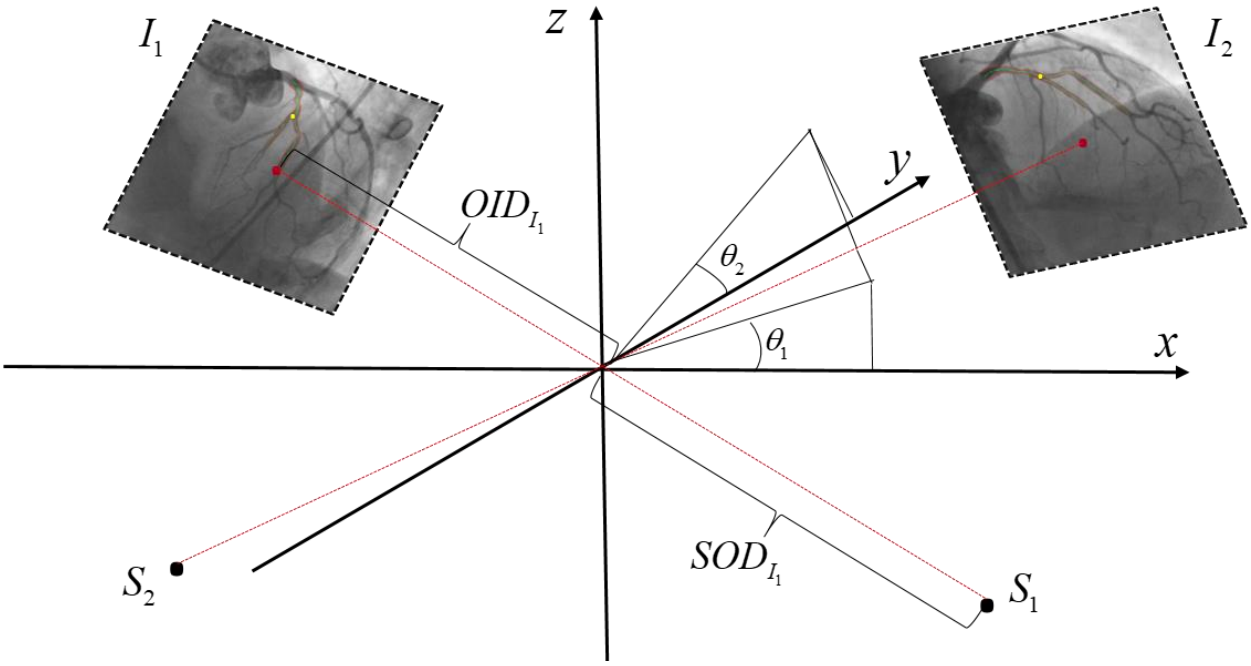

Figure 3.9: The position of the angiographic views and source points into the 3D space.

The final (u, v, t) system of two angiographic views and the source points is defined as follows (Figure 3.9):

$$\begin{aligned} I_1 &= \left[I_1 \cdot \mathrm{R}_{x\_I_1} \right] \cdot \mathrm{R}_{y\_I_1}, \\ S_1 &= \left[S_1 \cdot \mathrm{R}_{x\_I_1} \right] \cdot \mathrm{R}_{y\_I_1}, \end{aligned} \tag{3.19}$$

and

$$\begin{aligned} I_2 &= \left[I_2 \cdot \mathrm{R}_{x\_I_2} \right] \cdot \mathrm{R}_{y\_I_2}, \\ S_2 &= \left[S_2 \cdot \mathrm{R}_{x\_I_2} \right] \cdot \mathrm{R}_{y\_I_2}. \end{aligned} \tag{3.20}$$

Before implementing the back-projection algorithm for the extraction of the 3D centerline we modified the system of equation (3.19) and (3.20) by matching the reference bifurcation points (BRP_{I_1}, BRP_{I_2}) in the 3D space. Initially, we construct the following 3D lines:

$$\begin{aligned} \overline{E_{I_1}} &= \overline{BRP_{I_1}\, S_1}, \\ \overline{E_{I_2}} &= \overline{BRP_{I_2}\, S_2}, \end{aligned} \tag{3.21}$$

where $\overline{E_{I_1}}$ edge connects the points BRP_{I_1} and S_1, while $\overline{E_{I_2}}$ edge connects the points BRP_{I_2} and S_2. Then we project the given ISO Center of the system on both edges:

$$\begin{aligned} B_1 &= project(\text{ISO}, \overline{E_{I_1}}), \\ B_2 &= project(\text{ISO}, \overline{E_{I_2}}). \end{aligned} \tag{3.22}$$

producing thus the points B_1 and B_2 points as it is shown in Figure 3.10.

Finally, we translate the projection views and the source points to (u, v, t) coordinates as follows (Figure 3.11):

$$\begin{aligned} I_1' &= I_1 + \left|\text{ISO} - B_1\right|, \\ S_1' &= S_1 + \left|\text{ISO} - B_1\right|, \end{aligned} \tag{3.23}$$

and

$$\begin{aligned} I_2' &= I_2 + \left|\text{ISO} - B_2\right|, \\ S_2' &= S_2 + \left|\text{ISO} - B_2\right|. \end{aligned} \tag{3.24}$$

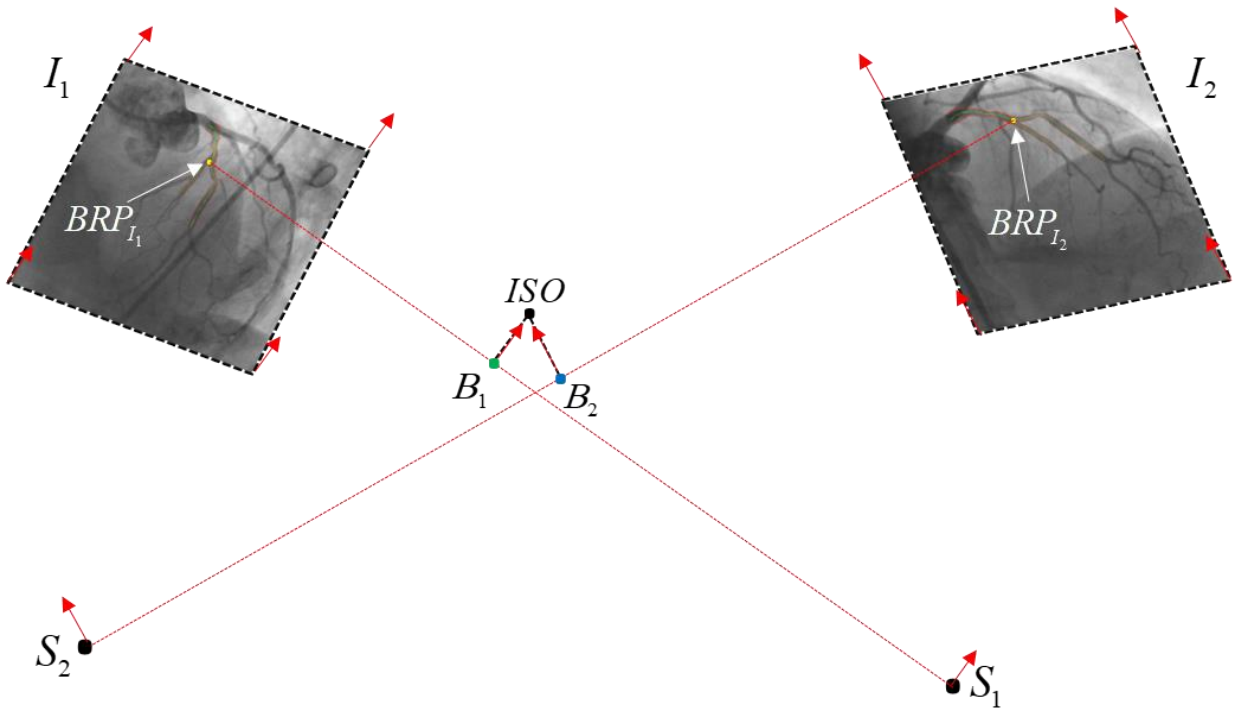

Figure 3.10: The impact of ISO center on the registration of angiographic views and source points in the 3D space.

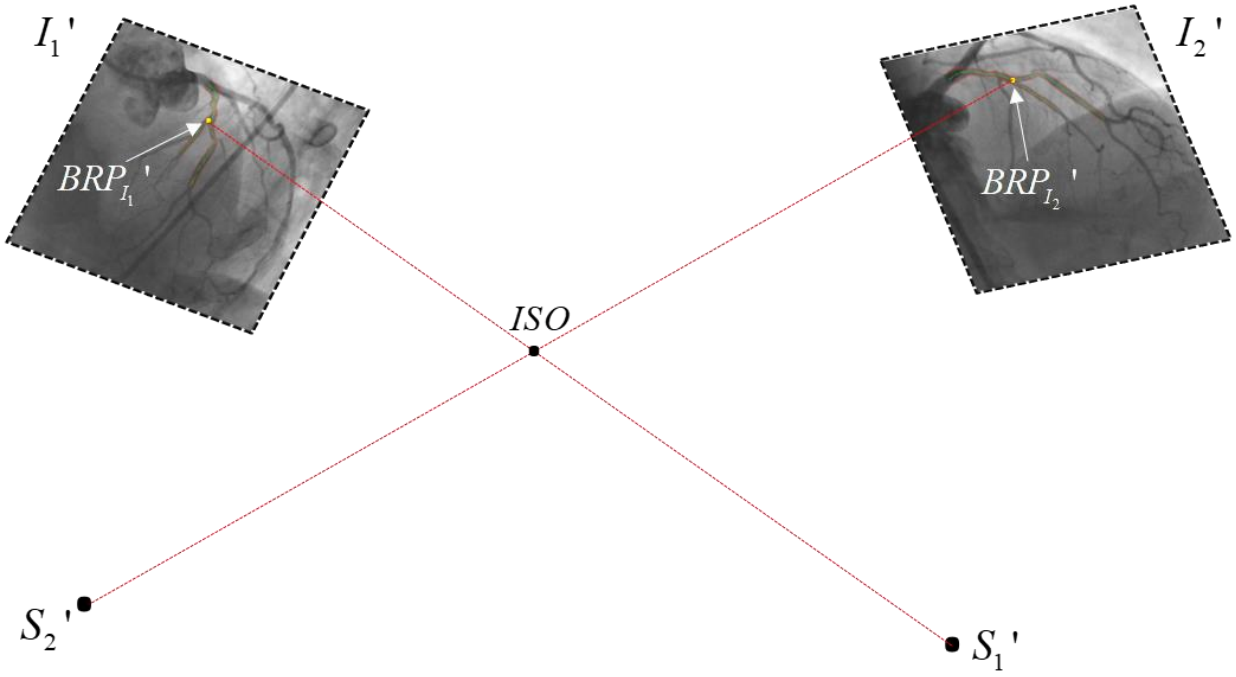

Figure 3.11: The system of angiographies and source points after the registration process.

3.7.2 3D centerline reconstruction

After orienting both the angiographies and the source points properly in the 3D space we implement the back-projection algorithm [39, 100]. Initially, for each projection view ($I_1^{'}$, $I_2^{'}$), we create the surface between all the centerline points of the view and the corresponding source points ($S_1^{'}$, $S_2^{'}$) [101]. For example, working on the main branch, we create the surfaces as follows (Figure 3.12 a):

$$\begin{aligned} Surf_{MB\_I_1}(u,v,t) &= surface(\mathrm{C}'_{MB\_I_1}, \mathrm{S}'_1), \\ Surf_{MB\_I_2}(\mathrm{u},\mathrm{v},\mathrm{t}) &= surface(\mathrm{C}'_{MB\_I_2}, \mathrm{S}'_2), \end{aligned} \tag{3.25}$$

while the cross product between the two surfaces is the 3D centerline of the main branch (Figure 3.13):

$$C_{MB\_3D}(i) = cross(\mathrm{Surf}_{MB\_I_1}, \mathrm{Surf}_{MB\_I_2}),\ i = 1,...,n\,. \tag{3.26}$$

Similarly, we create the back projected surfaces for the side branch (Figure 3.12 b):

$$\begin{aligned} Surf_{SB\_I_1}(u,v,t) &= surface(\mathrm{C}'_{SB\_I_1}, \mathrm{S}'_1), \\ Surf_{SB\_I_2}(\mathrm{u},\mathrm{v},\mathrm{t}) &= surface(\mathrm{C}'_{SB\_I_2}, \mathrm{S}'_2), \end{aligned} \tag{3.27}$$

and finally we extract the 3D centerline of it (Figure 3.13):

$$C_{SB\_3D}(j) = cross(\mathrm{Surf}_{SB\_I_1}, \mathrm{Surf}_{SB\_I_2}),\ j = 1,...,n\,. \tag{3.28}$$

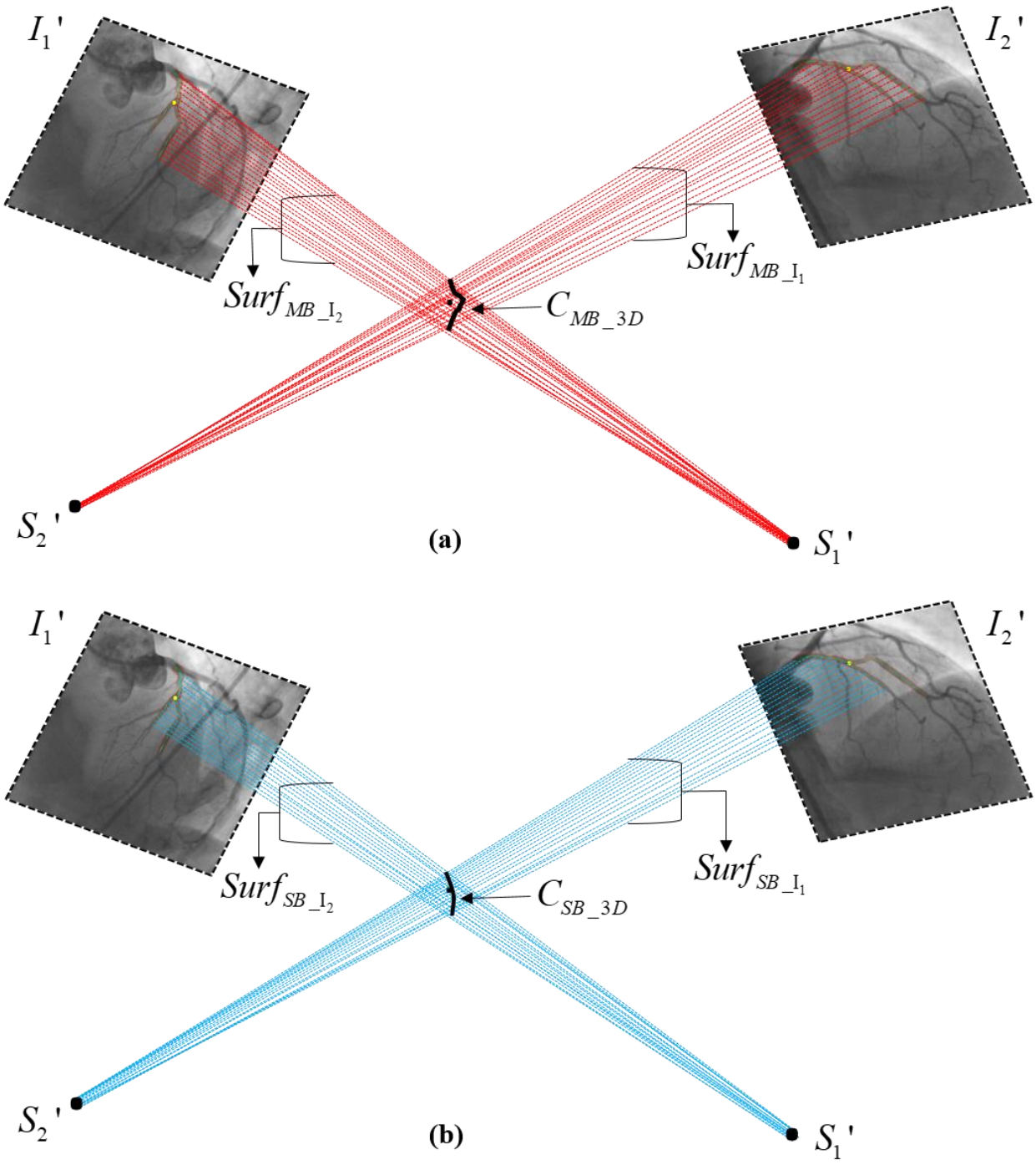

Figure 3.12: Implementation of the Back-projection algorithm for the extraction of: a) the centerline of the main branch, b) the centerline of the side branch.

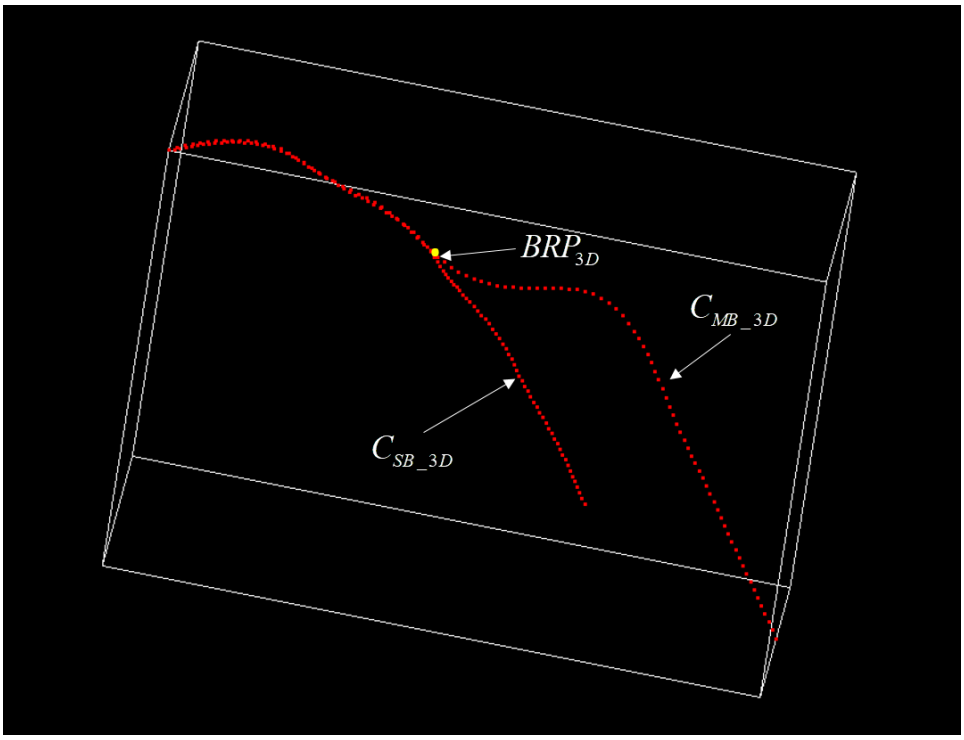

Figure 3.13: The extracted 3D centerline of the bifurcated coronary artery.

3.7.3 3D lumen borders reconstruction

For each point of the bifurcated centerline (C_{MB_3D}, C_{SB_3D}) we compute the normal vectors ($N_{MB\_3D}(i)$, $N_{SB\_3D}(j)$, $i = 1,...,n, j = 1,...,n$) (Figure 3.14).

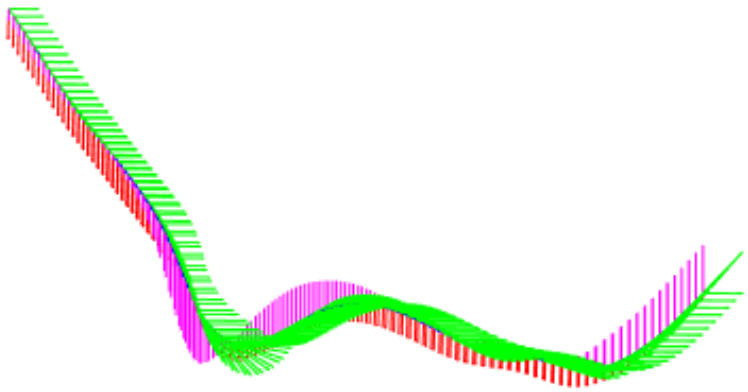

Figure 3.14: The centerline of an artery segment with the tangent, normal and binormal vectors

Taking into account the $i-th$ point of centerline as well as the normal vector on it, we compute the $i-th$ plane perpendicular to the centerline:

- of the main branch

$$PL_{MB\_3D}(i) = plane(\mathrm{C}_{MB\_3D}(i), \mathrm{N}_{MB\_3D}(i)),\ i = 1,...,n, \tag{3.29}$$

- of the side branch

$$PL_{SB\_3D}(j) = plane(\mathrm{C}_{SB\_3D}(j), \mathrm{N}_{SB\_3D}(j))\ \ j = 1,...,n\,. \tag{3.30}$$

Then, we implement again the back-projection algorithm to reconstruct the lumen borders. For example, considering the 3D reconstruction of the lumen borders of the main coronary branch we create the following 3D edges (Figure 3.15):

$$\begin{aligned} \overline{L_{\mathrm{right}\_I_1}(i)} &= \overline{BM'_{right\_I_1}(i)\,S'_1}, \\ \overline{L_{\mathrm{left}\_I_1}(i)} &= \overline{BM'_{\mathrm{left}\_I_1}(i)\,S'_1}, \end{aligned} \quad i = 1,...,n, \tag{3.31}$$

and

$$\begin{aligned} \overline{L_{\mathrm{right}\_I_2}(i)} &= \overline{BM'_{right\_I_2}(i)\,S'_2}, \\ \overline{L_{\mathrm{left}\_I_2}(i)} &= \overline{BM'_{\mathrm{left}\_I_2}(i)\,S'_2}, \end{aligned} \quad i = 1,...,n\,. \tag{3.32}$$

Furthermore, we calculate the intersection between the $i-th$ plane with the edges of equation (3.31) and (3.32) as follows:

$$\begin{aligned} L_{1\_3D}(i) &= \mathrm{intersection}(\overline{L_{\mathrm{right}\_I_1}(i)}, PL_{MB\_3D}(i)), \\ L_{2\_3D}(i) &= \mathrm{intersection}(\overline{L_{\mathrm{left}\_I_1}(i)}, PL_{MB\_3D}(i)), \\ L_{3\_3D}(i) &= \mathrm{intersection}(\overline{L_{\mathrm{right}\_I_2}(i)}, PL_{MB\_3D}(i)), \\ L_{4\_3D}(i) &= \mathrm{intersection}(\overline{L_{\mathrm{left}\_I_2}(i)}, PL_{MB\_3D}(i)), \end{aligned} \quad i = 1,...,n \tag{3.33}$$

extracting thus the four 3D lumen borders (L_{1_3D}, L_{2_3D}, L_{3_3D}, L_{4_3D}).

Finally, we interpolate the four lumen borders with a spline method of 50 points (Figure 3.15).

$$Contour_{MB\_3D}(i) = spline((L_{1\_3D}(i), L_{2\_3D}(i), L_{2\_3D}(i), L_{3\_3D}(i), L_{4\_3D}(i)), 50)\ \ i = 1,...,n\,. \tag{3.34}$$

Totally, we extracted the lumen contours separately for the main branch:

$$Contour_{MB\_3D}(i),\ \ i=1,...,n \tag{3.35}$$

and for the side branch

$$Contour_{SB\_3D}(j),\ \ j=1,...,n \tag{3.36}$$

Figure 3.15 depicts the process of the reconstruction of the lumen borders, while Figure 3.16 depicts the 3D point cloud of the coronary bifurcation artery.

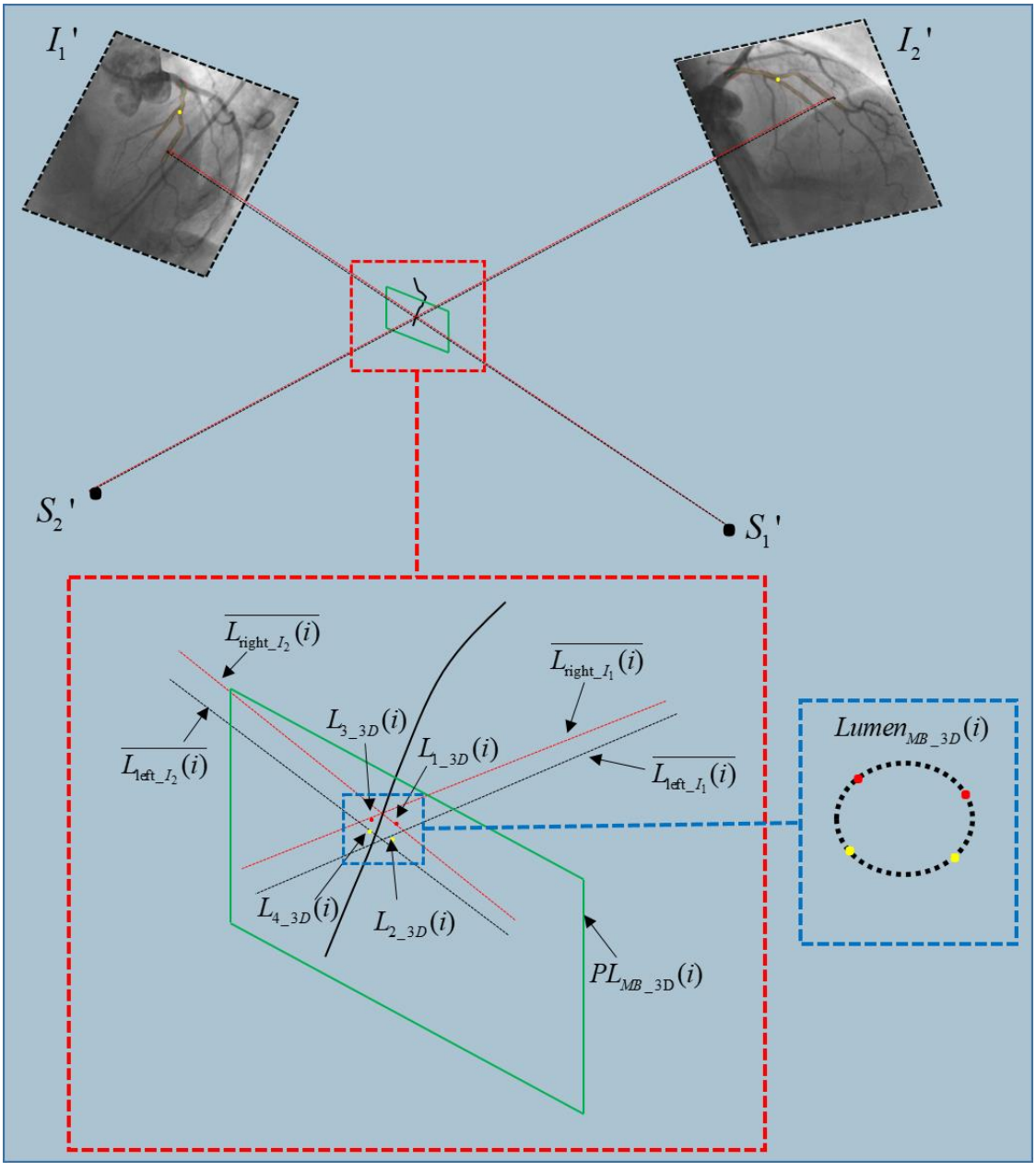

Figure 3.15: The process of the lumen borders 3D reconstruction.

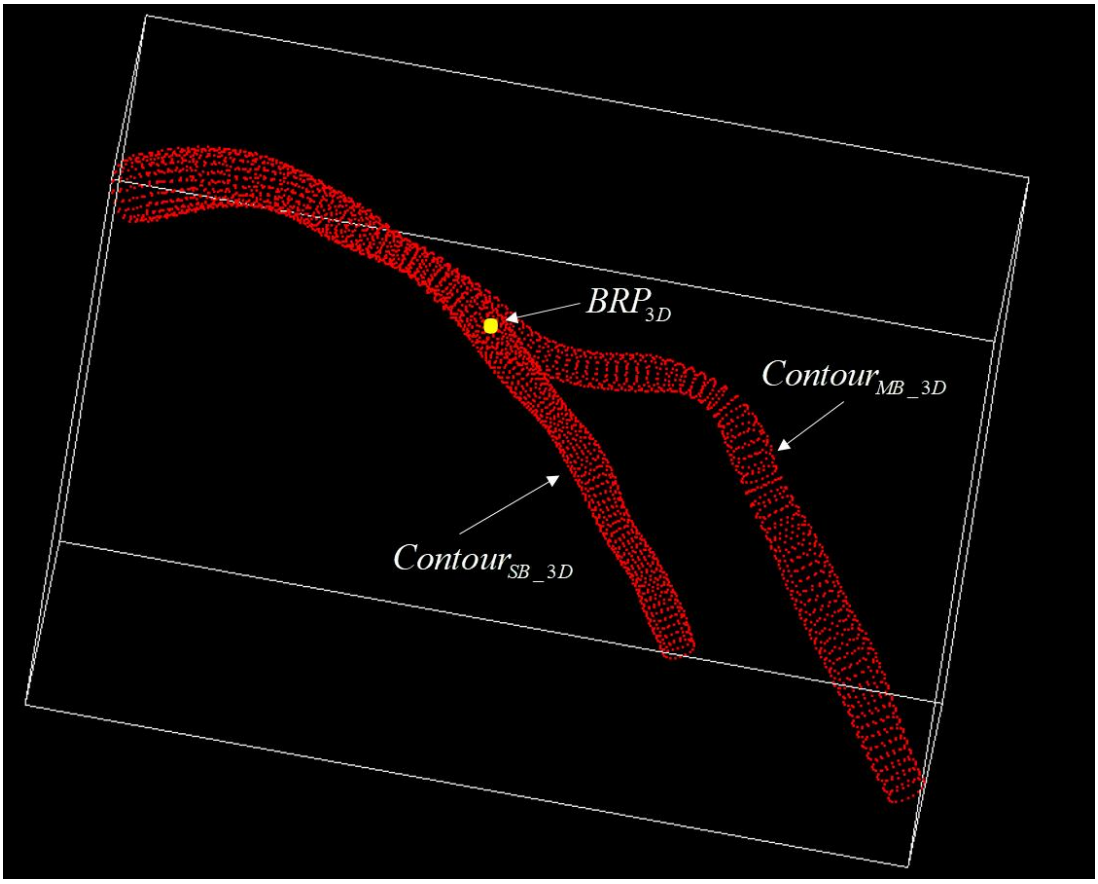

Figure 3.16: The 3D point cloud of the coronary bifurcating artery.

3.7.4 Registration of the main and the side branch

Initially, we define the plane perpendicular to the centerline on the 3D Bifurcation Reference Point (BRP_{3D}). Then, we remove all the points beyond the plane, decreasing thus the number of the contours of the side branch:

$$Contour_{\mathrm{SB\_3D}}(\mathrm{j}),\ j=1,\ldots,n \rightarrow Contour_{\mathrm{SB\_3D}}(\mathrm{m}),\ m=1,\ldots,\mathrm{p},\ \mathrm{p}<\mathrm{n}\,. \qquad (3.37)$$

Subsequently, we extract the 3D geometry of the main branch using the Delaunay triangulation method [102]. The first level of the registration was performed by removing the points of the side branch which are located into the main branch.

$$G_{MB} = delaunay\_triangulation(Contour_{MB}(i)),\ i=1,\ldots,n\,, \qquad (3.38)$$

$$Contour_{SB}(m) = G_{MB} - Contour_{SB}(m),\ m=1,\ldots,\mathrm{p}\,, \qquad (3.39)$$

In the same manner, the 3D geometry of the modified side branch is extracted. Finally, the second level of the registration process is performed by removing the points of the main branch are located the modified (from previous step) side branch.

$$G_{SB} = delaunay\_triangulation(Contour_{MB}(\mathrm{m})),\ \ m = 1,...,\mathrm{p}, \tag{3.40}$$

$$Contour_{MB}(i) = G_{SB} - Contour_{MB}(i),\ \ i = 1,...,n. \tag{3.41}$$

Figure 3.17 depicts the 3D point cloud of the bifurcation artery both before and after the registration process

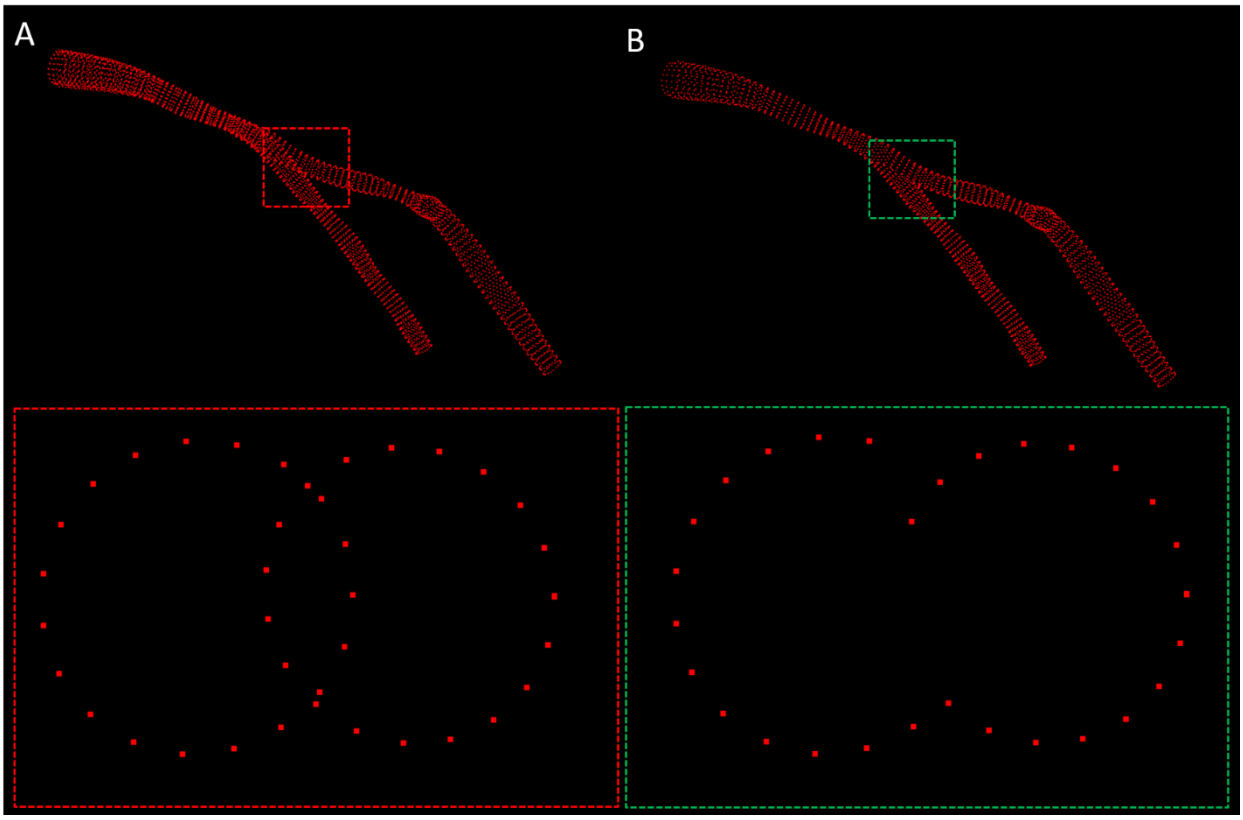

Figure 3.17: A. The 3D model before the registration process B. the 3D model after the registration process.

3.8 Validation strategy

The comparison between different types of coronary artery reconstruction methods is difficult to be achieved due to the diversity of the acquisition protocols, specific requirements for the method and especially the lack of standard dataset and performance metrics. Nevertheless, two evaluation methods are mainly proposed by the literature [61]:

- methods which compare the 3D model of the vessel with phantoms,
- and methods which compare the 3D model with the 2D angiographies.

To validate the performance of the proposed algorithm in this study we use the second methodology. Initially we performed both 2D and 3D quantitative coronary analysis on our dataset, calculating geometrical features of the vessels such as the lumen diameter. Then, considering the 2D X-ray angiography as the "Gold Standard" we evaluate the accuracy of the proposed 3D QCA method using lumen diameter-based metrics [103] :

- Reference Vessel Diameter (RVD),
- Minimum Lumen Diameter (MLD),
- Degree of stenosis (DS),
- Lesion length (LL).

Specifically, we consider the RVD (mm) as the mean value of the healthy vessel diameters before and after the coronary lesion:

$$RVD = \frac{D_{before\_lesion} + D_{after\_lesion}}{2}. \tag{3.42}$$

The MLD (mm) is defined as follows:

$$MLD = \min(D(i)),\ i = 1,...,\mathrm{n}. \tag{3.43}$$

The DS (%) as the difference between the MLD from the target RVD, divided by the RVD:

$$DS = \frac{|RVD - MLD|}{RVD} 100\%. \tag{3.44}$$

Finally, we consider the LL (mm) as the length of the centerline part corresponding to the lesion.

It is worth to be noted that these measurements were extracted segmentally (only the main btanch) for each sub-segment of the bifurcation vessel (Proximal Main Branch, Distal Main Branch, Side Branch) as this has been mentioned in previous sections (Figure 3.18).

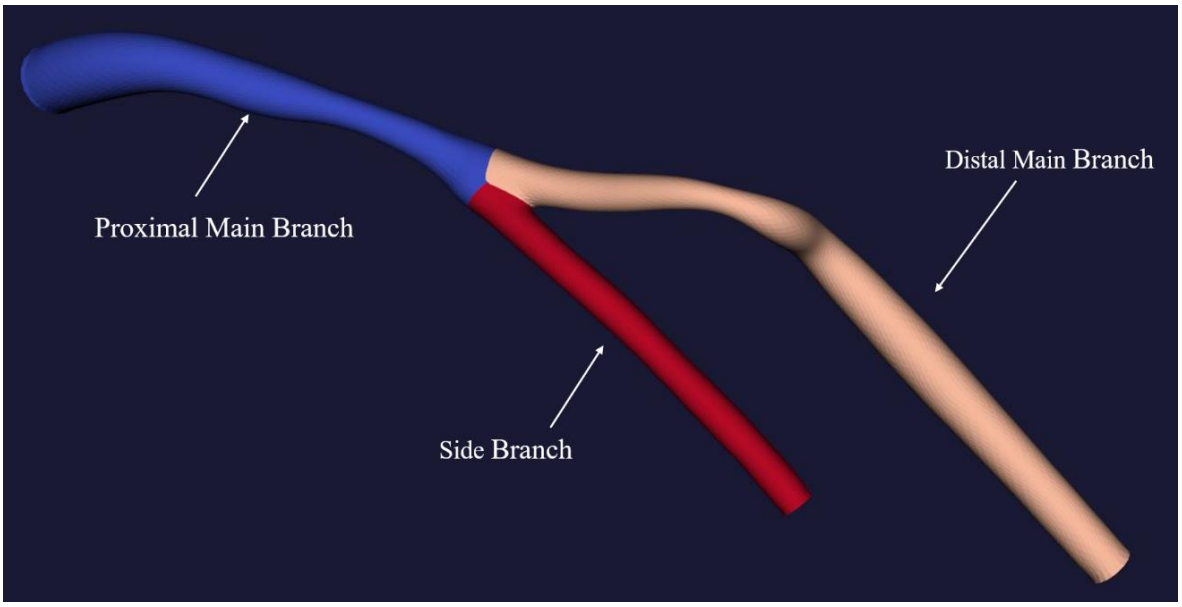

Figure 3.18: The sub-segments of the coronary bifurcation artery.

The calculation of the re-projection error of the 3D model by projecting forwardly the 3D lumen borders onto the angiographic views is another strategy to validate the proposed method. In fact, it does not provide any error of the 3D space but it is used to evaluate the performance in the experiments using clinical X-ray angiography images. Therefore, we recovered the 2D borders of the lumen by projecting the 3D geometry of the vessel onto the angiographies as follows (Figure 3.19):

$$R_{I_1} = project(Bifurcation_{3D}, \mathrm{I}'_1),$$
$$R_{I_2} = project(Bifurcation_{3D}, \mathrm{I}'_2), \tag{3.45}$$

where I'_1 and I'_2 are the projection views of the equations (3.23) and (3.24), $Bifurcation_{3D}$ is the 3D reconstructed model of the equations (3.39) and (3.41), while R_{I_1}, R_{I_2} are the recovered 2D lumen borders. Then, we compare the recovered 2D borders of the model with the true silhouette of the vessel using Spatial distance as well as overlap based metrics [104]:

- Hausdorff Distance (HD)
- Dice Coefficient (DC)

The average Haussdorff distance [105] is defined as follows:

$$HD(R_{I_1}, L_{I_1}) = max(h(R_{I_1}, L_{I_1}), h(L_{I_1}, R_{I_1})), \tag{3.46}$$

where $h(R_{I_1}, L_{I_1})$ is called the direct Hausdorff distance and given by the following equation:

$$h(R_{I_1}, L_{I_1}) = \frac{1}{N} \sum_{a \in R_{I_1}} \min_{b \in L_1} \|a - b\|, \tag{3.47}$$

where $\|a - b\|$ is the Euclidean distance.

The Dice Coefficient [106] is the most used metric in validating medical image segmentations. Using this method, we calculated the pairwise overlapping percentage of the recovered and the true lumen pixels as follows:

$$DICE = \frac{2TP}{2TP + FP + FN}, \tag{3.48}$$

where TP is the true positive rate, FP is the false positive rate and FN is the false negative rate.

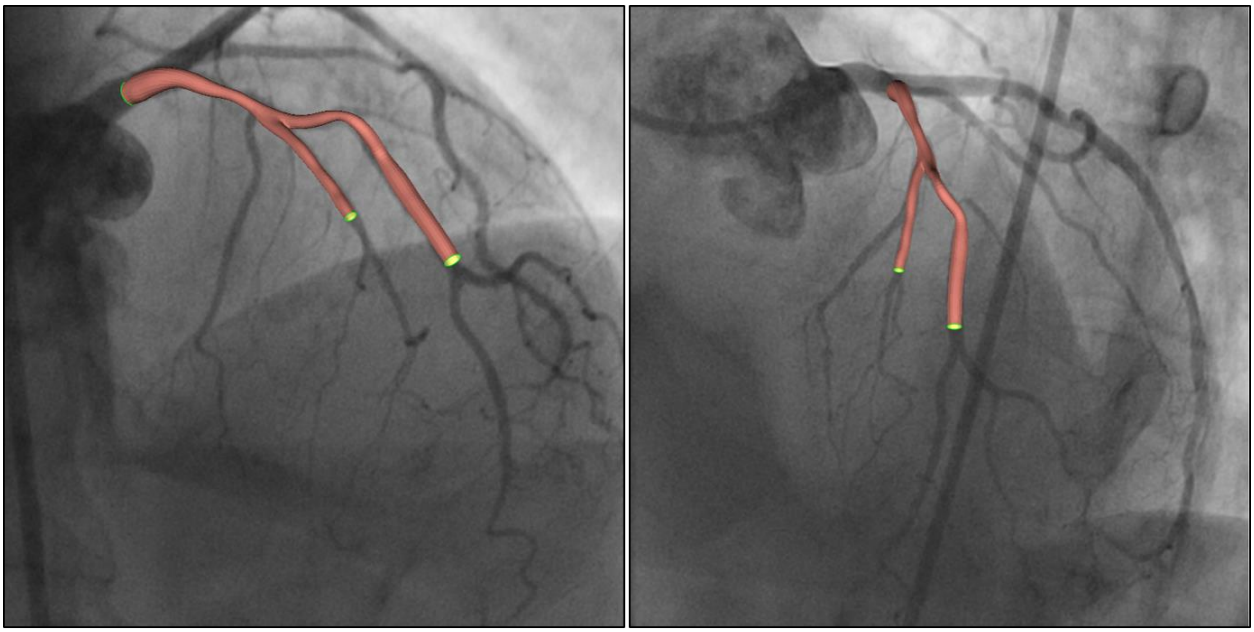

(a) **(b)**

Figure 3.19: Forward projection of the 3D model onto a) the first angiographic projection, b) the second angiographic projection.

3.9 Blood flow modeling

In this section the mathematical background of the blood flow modeling is provided. Therefore, we will describe some principles of the computational fluid mechanics, which are useful for the

simulations. Considering the blood as a Newtonian fluid we model the blood flow by solving the Navier-Stokes equations in the 3D space. Assuming constant density p and viscosity μ the 3D Navier-Stokes equations are:

$$\rho\left(\frac{\partial v_x}{\partial t}+v_x\frac{\partial v_x}{\partial x}+v_y\frac{\partial v_x}{\partial y}+v_z\frac{\partial v_x}{\partial z}\right)=-\frac{\partial p}{\partial x}-\mu\left(\frac{\partial \tau_{xx}}{\partial x}+\frac{\partial \tau_{xy}}{\partial y}+\frac{\partial \tau_{zx}}{\partial z}\right)+\rho g_x, \tag{3.49}$$

$$\rho\left(\frac{\partial v_y}{\partial t}+v_x\frac{\partial v_y}{\partial x}+v_y\frac{\partial v_y}{\partial y}+v_z\frac{\partial v_y}{\partial z}\right)=-\frac{\partial p}{\partial y}-\mu\left(\frac{\partial \tau_{xy}}{\partial x}+\frac{\partial \tau_{yy}}{\partial y}+\frac{\partial \tau_{zy}}{\partial z}\right)+\rho g_y, \tag{3.50}$$

$$\rho\left(\frac{\partial v_z}{\partial t}+v_x\frac{\partial v_z}{\partial x}+v_y\frac{\partial v_z}{\partial y}+v_z\frac{\partial v_z}{\partial z}\right)=-\frac{\partial p}{\partial z}+\mu\left(\frac{\partial \tau_{xz}}{\partial x}+\frac{\partial \tau_{yz}}{\partial y}+\frac{\partial \tau_{zz}}{\partial z}\right)+\rho g_z, \tag{3.51}$$

where V_x, V_y, V_z are the velocity 3D vector, τ is the stress tensor, p is the pressure, g is the acceleration of the gravity and t is the time.

In the case of a Newtonian fluid the stress tensor τ components are:

$$\tau_{xx}=-\mu\left[2\frac{\partial v_x}{\partial x}-\frac{2}{3}(\nabla\cdot v)\right], \tag{3.52}$$

$$\tau_{yy}=-\mu\left[2\frac{\partial v_y}{\partial y}-\frac{2}{3}(\nabla\cdot v)\right], \tag{3.53}$$

$$\tau_{zz}=-\mu\left[2\frac{\partial v_z}{\partial z}-\frac{2}{3}(\nabla\cdot v)\right], \tag{3.54}$$

$$\tau_{xy}=\tau_{yx}=-\mu\left[\frac{\partial v_x}{\partial y}+\frac{\partial v_y}{\partial x}\right], \tag{3.55}$$

$$\tau_{yz}=\tau_{zy}=-\mu\left[\frac{\partial v_y}{\partial z}+\frac{\partial v_z}{\partial y}\right], \tag{3.56}$$

$$\tau_{zx}=\tau_{xz}=-\mu\left[\frac{\partial v_z}{\partial x}+\frac{\partial v_x}{\partial z}\right], \tag{3.57}$$

where

$$(\nabla\cdot v)=\frac{\partial v_x}{\partial x}+\frac{\partial v_y}{\partial y}+\frac{\partial v_z}{\partial z}. \tag{3.58}$$

We consider steady state conditions, and thus the terms $\frac{\partial v_y}{\partial t}$, $\frac{\partial v_x}{\partial t}$ and $\frac{\partial v_z}{\partial t}$ are eliminated from the equations. By ignoring the g forces equations (3.49), (3.50), (3.51) become:

$$\rho\left(v_x\frac{\partial v_x}{\partial x}+v_y\frac{\partial v_x}{\partial y}+v_z\frac{\partial v_x}{\partial z}\right)=-\frac{\partial p}{\partial x}-\mu\left(\frac{\partial \tau_{xx}}{\partial x}+\frac{\partial \tau_{xy}}{\partial y}+\frac{\partial \tau_{zx}}{\partial z}\right), \tag{3.59}$$

$$\rho\left(v_x\frac{\partial v_y}{\partial x}+v_y\frac{\partial v_y}{\partial y}+v_z\frac{\partial v_y}{\partial z}\right)=-\frac{\partial p}{\partial y}-\mu\left(\frac{\partial \tau_{xy}}{\partial x}+\frac{\partial \tau_{yy}}{\partial y}+\frac{\partial \tau_{zy}}{\partial z}\right), \tag{3.60}$$

$$\rho\left(v_x\frac{\partial v_z}{\partial x}+v_y\frac{\partial v_z}{\partial y}+v_z\frac{\partial v_z}{\partial z}\right)=-\frac{\partial p}{\partial z}+\mu\left(\frac{\partial \tau_{xz}}{\partial x}+\frac{\partial \tau_{yz}}{\partial y}+\frac{\partial \tau_{zz}}{\partial z}\right), \tag{3.61}$$

The 3D geometry of the bifurcation artery is discretized into hexahedral finite elements, where the max element size was 0.01 mm. Regarding the material properties, the blood is assumed to be a Newtonian fluid with viscosity 0.0035 Pa · s and density 1050 kg/m^3. Furthermore, we apply a constant inlet blood velocity 0.15 m/s and zero pressure profile at the outlet, while we assume no slip and no penetration boundary condition on the wall (Figure 3.20).

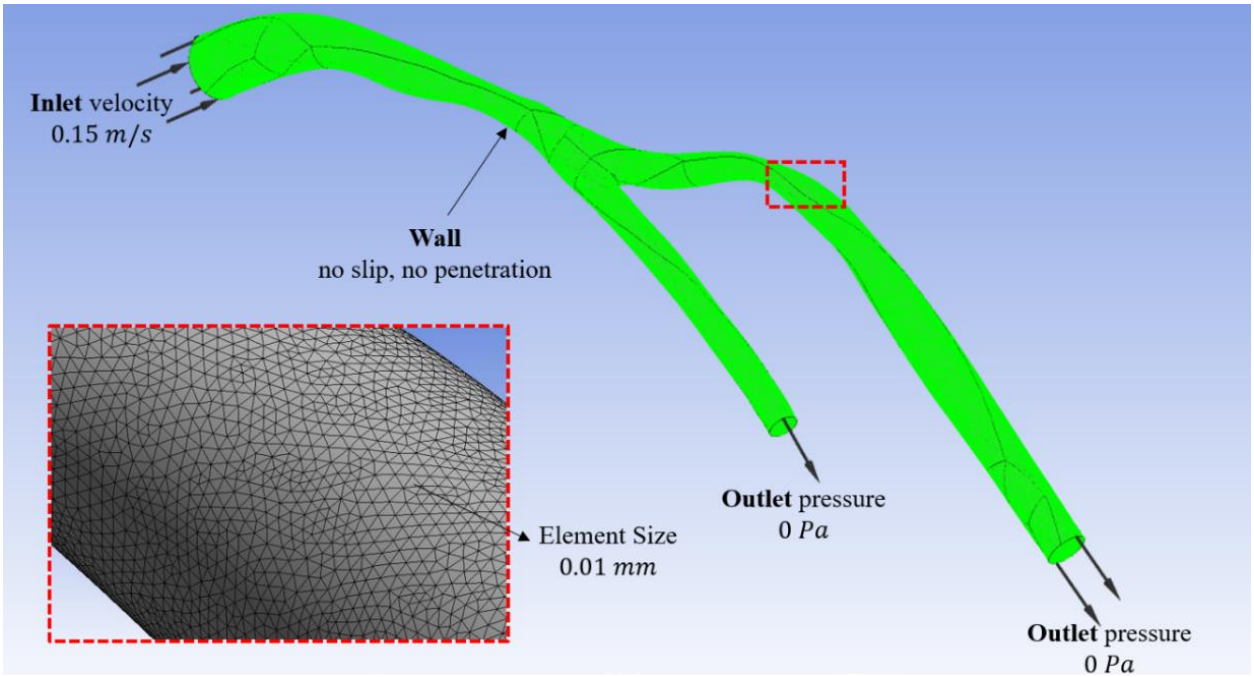

Figure 3.20: Boundary conditions on the 3D geometry of the coronary bifurcation artery.

3.10 Computational Fractional Flow Reserve (FFR)

In this section we describe the methodology that we have implemented in order to compute the FFR value in the 3D model of the bifurcated artery. For each case, we perform the blood flow modeling twice: the first time of simulations we impose outlet flow rates 2 ml/s, which value corresponds to average flow at the left coronary artery during rest, while the second one we consider outlet flow rate 6 ml/s, which value correspond to the average flow under stress. Furthermore, we use the Murray's law, which correlates the flow ratio through the side branches with the diameter of the branches as follows:

$$\frac{q_{D2}}{q_{D1}} = \left(\frac{d_{D2}}{d_{D1}} \right)^3 \tag{3.62}$$

where q_{D1} and q_{D2} are the flows and d_{D1} and d_{D1} are the diameters of the sub-branches which are calculated directly from the 3D model.

For each simulation the pressure gradient of each branch is calculated to produce the patient-specific P_d/P_a vs flow curve [107].

$$\frac{P_d}{P_a} = 1 - f_v \frac{Q}{P_a} - f_s \frac{Q^2}{P_a} \tag{3.63}$$

where Q is the flow rate, while f_v and f_s are the coefficients of pressure loss due to viscous friction and flow separation, respectively. Therefore, imposing $P_a = 100$ mmHg in Equation (3.63) we calculate the coefficients f_v and f_s and the area under the patient-specific P_d/P_a vs flow curve. Totally, the FFR of the 3D model is calculated as the ratio of the area under the patient-specific P_d/P_a vs flow curve to the respective reference area.

3.11 Dataset

Nineteen patients were subjected to Invasive Coronary Angiography (ICA). Out of these patient, totally 26 coronary bifurcation arteries were used in the current study. The first 12 coronary arteries correspond to 12 individual patients with ischemic symptoms. The other 14 coronary bifurcating arteries correspond to the rest 7 patients both before and after the Percutaneous Transluminal Coronary Angioplasty (PTCA) procedure. All the 26 coronary bifurcation arteries were reconstructed into the 3D space, using the proposed method, while blood flow simulations were

performed for the 3D geometries of the vessels. For 9 cases of the dataset we computed the Fractional Flow Reserve and we evaluated it using the clinical wired-based measurements.

Table 3.1: Dataset

cases	ICA imaging data		FFR
	Pre PTCA	Post PTCA	
1	✓		✓
2	✓		
3	✓		✓
4	✓		✓
5	✓		
6	✓		✓
7	✓		✓
8	✓		✓
9	✓		
10	✓		✓
11	✓		
12	✓		✓
13	✓	✓	
14	✓	✓	
15	✓	✓	
16	✓	✓	
17	✓	✓	
18	✓	✓	
19	✓	✓	
20	✓	✓	
21	✓	✓	
22	✓	✓	
23	✓	✓	
24	✓	✓	
25	✓	✓	
26	✓	✓	

Chapter 4. Results

4.1 Validation of the proposed method

4.1.1 Quantitative Validation

Initially, in order to evaluate the performance of the proposed algorithm we compared the 3D model with the 2D bifurcated vessel on the angiography, using lumen diameter-based metrics such as the Reference Vessel Diameter (RVD), the Minimum Lumen Diameter (MLD), the Degree of Stenosis (DS) and the Lesion Length (LL). These comparisons were performed segmentally (without the side branch) for each sub-segment of the coronary bifurcation anatomy (Proximal Main, Distal Main and Side Branch). Table 4.1 depicts the results both of the 2D and 3D quantitative analysis for the total dataset of the 26 coronary bifurcation arteries.

Comparing with the 2D QCA, the proposed method demonstrates high accuracy for the 3D reconstruction of the coronary bifurcation artery. Regarding the RVD, which corresponds to a healthy diameter of the vessel, the 3D reconstructed vessels present almost equal mean value with the 2D ones. The regression analysis (Figure 4.1) show that the correlation between the mean 2D RVD with the mean 3D RVD is ($r=0.99$, $p<0.0001$), ($r=0.95$, $p<0.0001$) and ($r=0.95$, $p<0.0001$) for the Proximal Main, the Distal Main and the Side Branch, respectively. Actually, this accuracy

due to the fact that any healthy (no stenosed) part of the vessel is clearly visible on the angiographies and as a consequence can be easily translated into the 3D space.

Moreover, in the Table 4.1 the mean 3D MLD value is observed to be a little larger than the 2D one: 0.16 mm in the Proximal Main, 0.5 mm in the Distal Main and 0.10 mm in the Side Branch. This variation is absolutely normal and is mainly caused due to the fact that the 3D model was reconstructed using not a single but two angiographic projections. Considering the MLD value of a single projection view as the gold standard, the accuracy of the proposed method is high: ($r=0.86$, $p<0.0001$) for the Proximal Main Branch ($r=0.93$, $p<0.0001$) for the Distal Main Branch and ($r=0.93$, $p<0.0001$) for the Side Branch, while considering the DS, the proposed 3D QCA method presents decent precision for all the sub-segments. The accuracy is ($r=0.86$, $p<0.0001$), ($r=0.88$, $p<0.0001$) and ($r=0.95$, $p<0.0001$) for the Proximal Main, the Distal Main and the Side Branch, respectively.

Finally, the variance between the 3D and 2D LL is 1.73 mm in the Proximal Main, 2.37 mm in the Distal Main and 1.2 mm in the Side Branch. The lower recall of the LL is observed in the distal Main branch ($r=0.80$, $p<0.001$), where the majority of the dataset's lesions are located, while the in the Proximal Main and the Side Branch the accuracy is 0.84 and 0.88, respectively. Generally, the 3D QCA present longer mean LL value than the 2D QCA. This is due to the fact that the 3D QCA reconstruction method, which is based on the matching of two 2D angiographic views into the 3D space, produce a smoothed version of the vessel than the 2D angiography depicts. The total results of the evaluation process, such as the regression and Bland-Altman analysis are depicted in the following Tables and Figures:

- Proximal Main: Table 4.2 and Figure 4.1,
- Distal Main: Table 4.3 and Figure 4.2,
- Side Branch: Table 4.4 and Figure 4.3

Table 4.1: Sub-segment quantitative analysis.

	n=26			
	2D QCA	**3D QCA**	r	p
Proximal Main				
RVD (mm)	3.50 ± 0.68	3.49 ± 0.64	0.99	<0.001
MLD (mm)	2.73 ± 0.86	2.89 ± 0.71	0.86	<0.001
DS (%)	21.70 ± 20.12	17.27 ± 14.66	0.86	<0.001
LL (mm)	7.77 ± 3.78	9.50 ± 4.72	0.84	<0.001
Distal Main				
RVD (mm)	2.69 ± 0.44	2.67 ± 0.43	0.95	<0.001
MLD (mm)	1.71 ± 0.61	1.76 ± 0.59	0.93	<0.001
DS (%)	36.71 ± 17.35	34.11 ± 17.01	0.88	<0.001
LL (mm)	12.10 ± 6.67	14.47 ± 5.92	0.80	<0.001
Side Branch				
RVD (mm)	2.37 ± 3.78	2.36 ± 0.47	0.95	<0.001
MLD (mm)	1.69 ± 0.50	1.79 ± 0.51	0.93	<0.001
DS (%)	28.70 ± 16.53	28.56 ± 16.75	0.95	<0.001
LL (mm)	11.66 ± 6.68	12.86 ± 5.84	0.88	<0.001

Table 4.2: Quantitative analysis of the Proximal Main Branch.

cases	2D QCA				3D QCA			
	Proximal Main				Proximal Main			
	RVD (mm)	MLD (mm)	DS (mm)	LL (mm)	RVD (mm)	MLD (mm)	DS (%)	LL (mm)
1	2.78	2.69	3	4.51	2.85	2.82	1	2.50
2	2.92	2.57	12	9.62	2.91	2.67	8	8.80
3	3.59	2.78	23	11.05	3.57	2.72	24	11.45
4	3.56	2.81	21	10.38	3.51	2.94	16	13.89
5	2.48	1.85	26	5.55	2.66	1.81	32	9.30
6	3.63	3.11	14	4.16	3.55	3.15	11	7.18
7	3.59	3.55	1	3.57	3.57	3.55	1	2.38
8	3.67	3.57	3	11.45	3.53	3.26	8	10.76
9	3.80	2.24	41	9.08	3.76	2.30	39	8.55
10	5.00	3.71	26	13.16	4.86	3.59	26	15.73
11	3.26	2.86	12	5.63	3.17	2.79	12	9.91
12	3.39	3.17	6	4.19	3.57	3.44	4	3.70
13	4.25	3.45	19	12.77	4.25	3.79	11	18.71
14	3.83	3.51	8	14.18	3.89	3.31	15	17.23
15	4.12	3.43	17	5.35	4.05	3.42	16	10.55
16	2.61	2.16	17	4.43	2.53	2.33	8	7.54
17	4.13	3.74	10	5.68	4.05	3.91	3	6.72
18	2.81	2.68	5	2.67	2.81	2.63	6	6.72
19	3.19	1.72	46	14.30	2.97	1.68	43	13.89
20	4.04	3.82	5	1.73	4.02	3.75	7	3.22
21	2.27	1.20	47	5.49	2.27	1.29	43	8.13
22	2.41	2.11	13	7.06	2.64	2.56	3	3.38
23	3.35	1.13	66	6.73	3.38	1.98	41	7.39
24	4.31	1.03	76	13.17	4.30	3.02	30	18.05
25	4.20	2.31	45	7.72	4.16	2.53	39	12.78
26	3.82	3.73	2	8.46	3.98	3.92	2	8.48

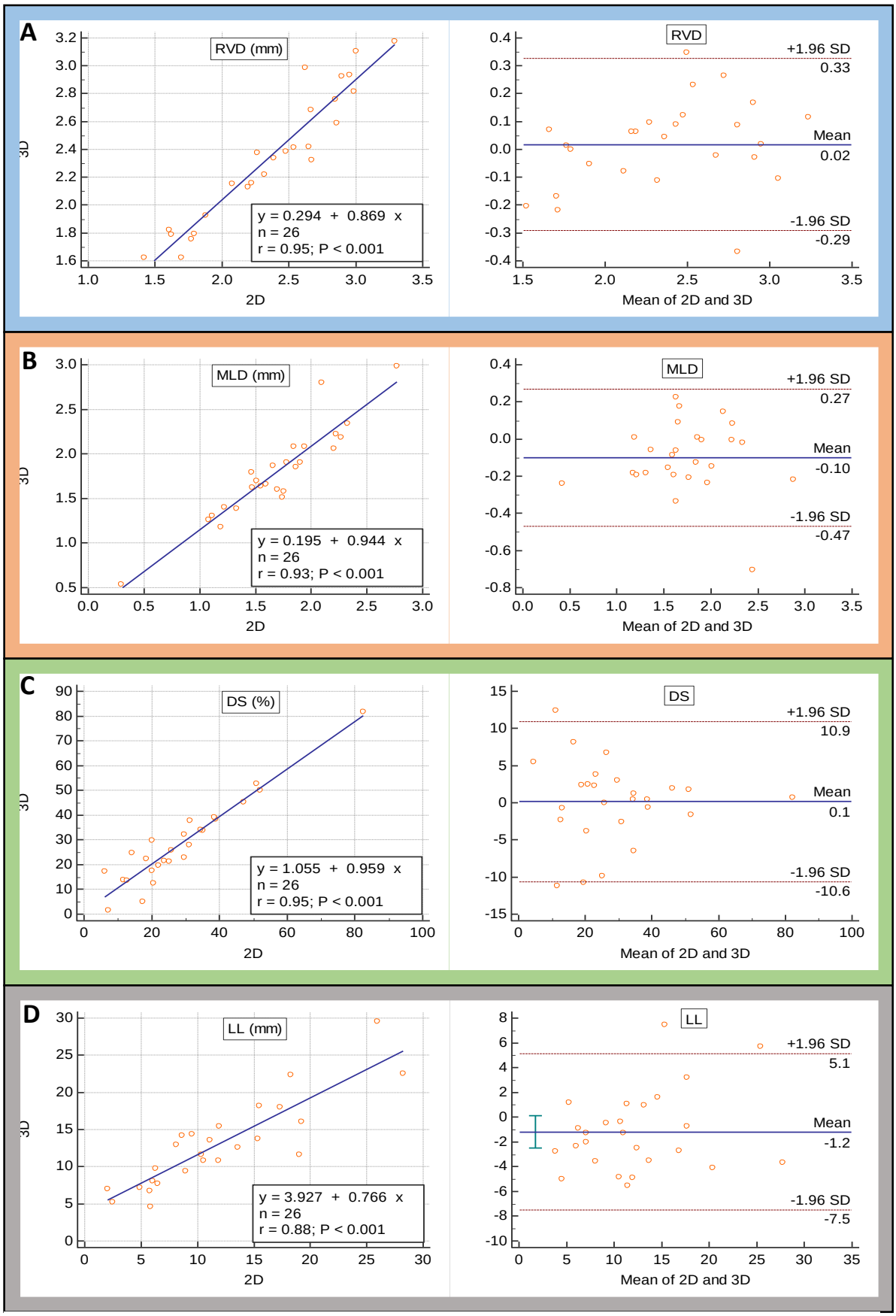

Figure 4.1: Regression (left) and Bland Altman (right) graph for a) the RVD, b) the MLD, c) the DS d) the LL of the Proximal Main Branch.

Table 4.3: Quantitative analysis of the Distal Main Branch.

cases	2D QCA				3D QCA			
	Distal Main				Distal Main			
	RVD (mm)	MLD (mm)	DS (mm)	LL (mm)	RVD (mm)	MLD (mm)	DS (%)	LL (mm)
1	2.18	1.17	46	14.60	2.19	1.30	40	17.22
2	2.07	1.11	46	22.21	2.03	1.28	37	23.99
3	3.13	0.75	76	16.31	3.12	0.81	74	18.20
4	2.44	1.46	43	17.31	2.57	1.56	39	17.36
5	2.39	0.74	68	10.70	2.31	1.39	40	13.51
6	2.89	2.20	21	12.94	2.77	2.26	18	17.31
7	2.44	1.16	52	16.31	2.43	1.08	55	13.47
8	2.41	1.84	22	14.93	2.35	1.91	19	15.24
9	2.74	2.22	19	9.08	2.76	2.20	20	6.41
10	3.67	2.99	20	12.53	3.73	3.08	17	13.92
11	2.73	1.16	58	4.50	2.74	1.06	61	7.94
12	2.82	2.48	15	9.36	2.90	2.59	11	9.20
13	3.00	2.30	21	12.22	2.91	2.50	14	17.86
14	2.88	2.24	25	7.09	2.97	2.46	17	14.64
15	3.43	2.06	41	13.36	3.47	1.82	48	20.46
16	2.06	1.05	48	5.48	2.04	1.27	38	11.61
17	2.98	1.82	36	12.07	2.85	1.59	44	23.88
18	2.12	1.43	37	4.58	2.26	1.54	32	7.56
19	2.80	1.74	33	14.51	2.60	1.55	40	15.87
20	2.70	1.52	44	6.05	2.70	1.60	41	10.20
21	2.21	2.05	14	2.50	2.40	2.24	7	7.55
22	2.00	0.88	56	35.30	2.00	1.08	46	30.99
23	2.74	1.30	52	8.70	2.68	1.50	44	12.30
24	3.17	1.96	31	9.51	2.83	1.49	47	10.31
25	3.00	2.18	15	7.00	2.57	1.93	25	11.50
26	3.06	2.60	18	15.51	3.16	2.79	12	7.73

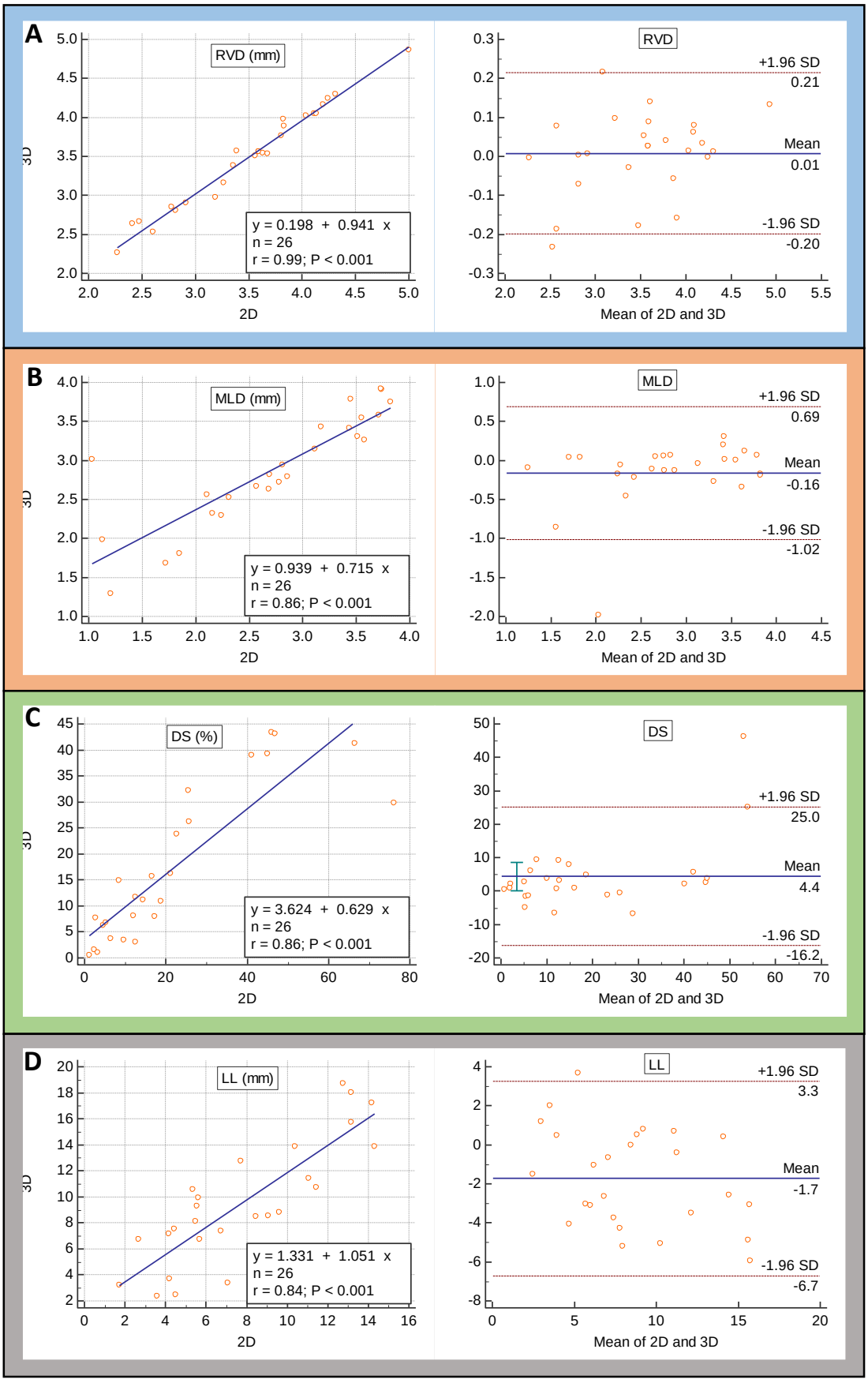

Figure 4.2: Regression (left) and Bland Altman (right) graph for a) the RVD, b) the MLD, c) the DS d) the LL of the Distal Main Branch.

Table 4.4: Quantitative analysis of the Side Branch.

cases	2D QCA				3D QCA			
	Side Branch				Side Branch			
	RVD (mm)	MLD (mm)	DS (mm)	LL (mm)	RVD (mm)	MLD (mm)	DS (%)	LL (mm)
1	1.70	0.30	82	15.36	1.63	0.53	82	13.74
2	2.65	1.87	30	25.91	2.42	1.85	23	29.58
3	2.07	1.46	30	8.94	2.15	1.80	32	9.43
4	1.77	1.08	39	17.30	1.76	1.26	38	18.06
5	1.88	1.66	12	11.89	1.93	1.87	14	10.83
6	2.22	1.69	24	15.49	2.16	1.60	22	18.19
7	2.66	2.32	13	11.91	2.69	2.34	13	15.41
8	2.67	2.21	17	10.50	2.32	2.06	5	10.87
9	2.62	2.09	20	13.60	2.99	2.80	30	12.64
10	2.98	2.77	7	6.27	2.82	2.99	2	9.80
11	2.32	1.60	31	8.62	2.22	1.66	28	14.16
12	2.19	1.75	20	8.12	2.13	1.58	18	12.96
13	3.00	1.47	51	11.11	3.11	1.63	53	13.61
14	2.85	2.22	22	10.36	2.76	2.22	20	11.64
15	3.29	1.74	47	19.23	3.18	1.52	45	16.03
16	2.38	1.55	35	4.87	2.34	1.64	34	7.19
17	2.90	1.78	39	2.48	2.92	1.90	39	5.23
18	2.26	1.85	18	5.80	2.38	2.08	22	6.72
19	2.54	1.90	25	5.81	2.41	1.90	21	4.63
20	1.79	1.33	26	6.05	1.79	1.39	26	8.04
21	1.61	1.51	6	2.00	1.82	1.70	17	6.97
22	1.42	1.22	14	28.24	1.62	1.40	25	22.53
23	2.96	1.94	34	6.46	2.94	2.08	34	7.71
24	2.48	1.19	52	18.29	2.39	1.18	50	22.36
25	2.86	2.27	21	9.50	2.59	2.18	12	14.41
26	1.62	1.11	31	19.04	1.79	1.31	38	11.59

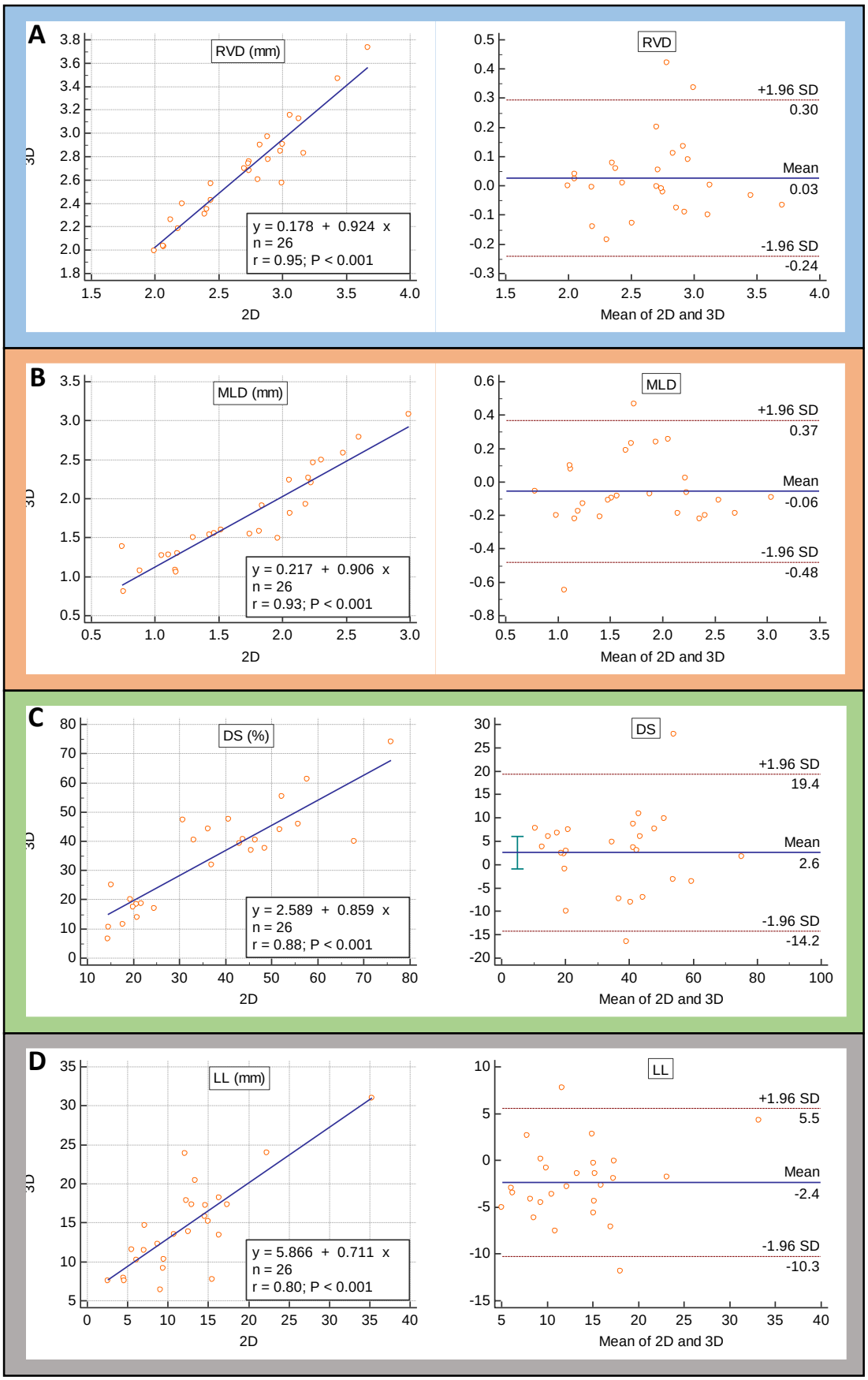

Figure 4.3: Regression (left) and Bland Altman (right) graph for a) the RVD, b) the MLD, c) the DS d) the LL of the Side Branch.

4.1.2 Validation based on the re-projection error

The second validation methodology is based on the projection of the 3D geometry of the vessel forward onto the angiographic projections to extract the 2D borders of the model (Figure 4.4). Then, we compare them with the annotated by expert lumen borders of the angiographic views using Spatial Distance and overlap-based metrics. Table 4.5 depicts the correlation between the 2D borders of the model and the annotated 2D lumen borders, which are considered as the gold standard, in terms of Hausdorff Distance and Dice Coefficient.

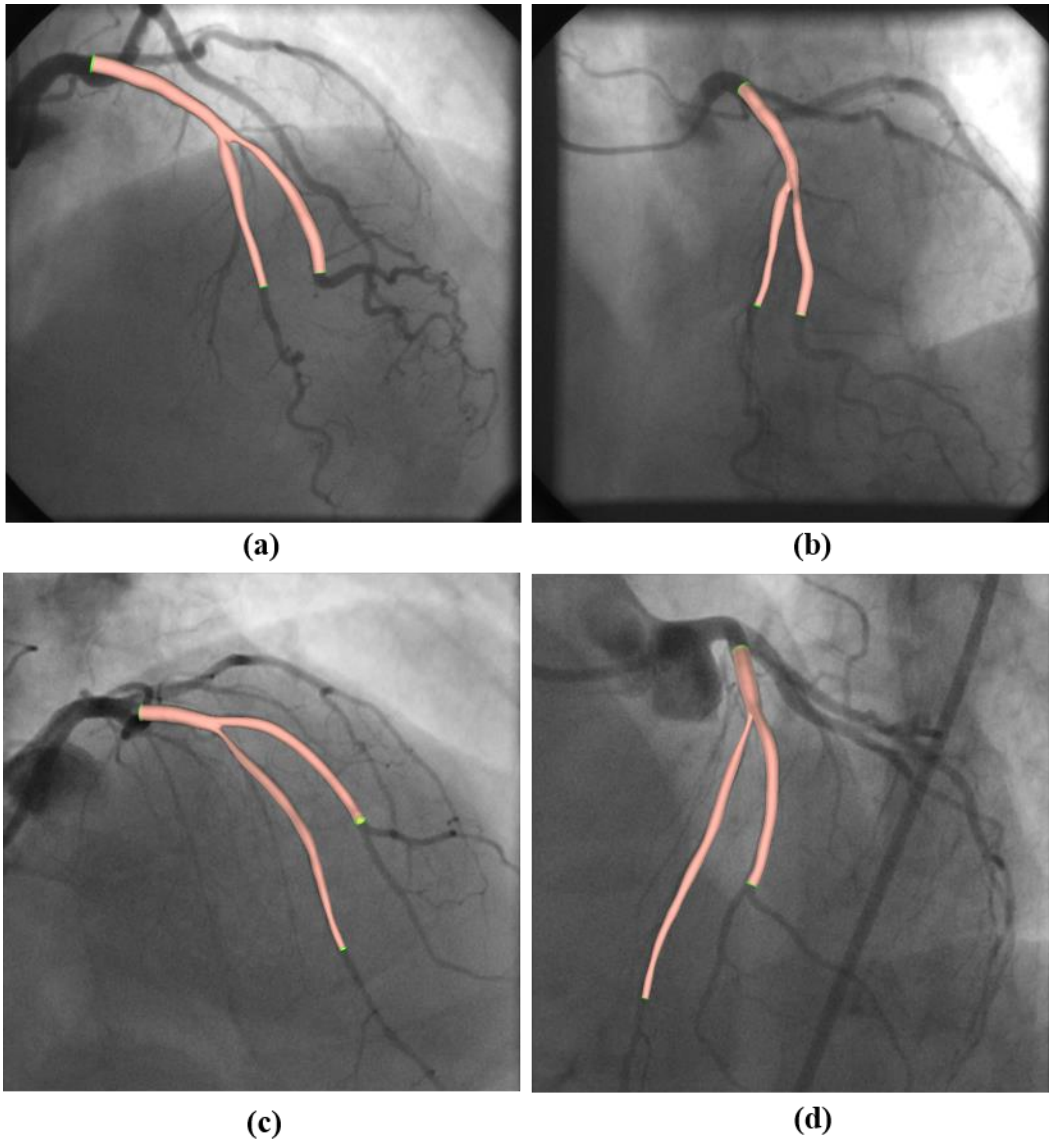

Figure 4.4: Forward projection of 3D models onto the angiographic views a-b) case 1, c-d) case 2.

Table 4.5: Correlation of the extracted 2D borders of model with the annotated 2D lumen borders in terms of Hausdorff Distance and Dice coefficient.

cases	View 1		View 2	
	HD (mm)	DC (%)	HD (mm)	DC (%)
1	0.09	98	0.35	88
2	0.19	93	0.13	98
3	0.11	95	0.17	96
4	0.12	97	0.08	99
5	0.07	98	0.48	79
6	0.08	98	0.50	80
7	0.43	95	0.24	92
8	0.39	94	0.09	97
9	1.08	75	0.22	95
10	0.32	95	0.15	97
11	0.88	77	0.08	99
12	0.28	94	0.10	96
13	0.08	98	1.26	80
14	0.13	97	0.50	88
15	0.16	93	0.16	96
16	0.90	79	0.06	97
17	0.30	96	0.08	98
18	1.88	84	0.14	95
19	0.16	95	0.06	98
20	0.20	94	0.07	99
21	0.06	98	0.51	87
22	0.20	93	0.06	98
23	0.10	97	0.79	84
24	0.09	98	0.09	97
25	0.13	98	0.29	92
26	0.34	91	0.10	97

In the Table 4.5 we observe that the 3D reconstructed models present high resemblance to the 2D vessels of the angiographic projections. In fact, taking into account the dataset of the 26 coronary bifurcated arteries, the mean Hausdorff Distance between the 2D borders of the model and the 2D annotated lumen borders, is 0.34 mm for the first angiographic view and 0.26 for the second one. The majority of the cases present remarkable HD values (less than 0.5 mm), highlighting thus the accuracy of the proposed 3D reconstruction method. Considering the Dice Coefficient value, the mean similarity of the 2D borders of model with the 2D annotated lumen borders is 0.93 both for the first and the second angiographic view.

Regarding the limitation of the 3D QCA, the complex shape of the artery onto the angiography (e.g. vessels overlapping) could lead to wrong 2D vessel segmentation while confined angle offset between the angiographic views could lead to failed 3D reconstruction of the bifurcation vessel. Therefore, the requirements of the proposed 3D QCA methodology are: i) high image resolution, ii) fine visualized coronary segments of the bifurcations artery on the coronary angiographies and iii) sufficient angle offset between the angiographic views ($\geq 30°$).

4.2 Blood flow modeling and assessment of the ESS

4.2.1 The impact of Side Branch on the blood flow modeling and the assessment of the ESS

We simulated the blood flow into the 3D geometries, as it has been described in section 3.9. Taking into account the first 12 coronary arteries of the dataset, we simulated the blood flow twice: considering the bifurcated vessels (both the main and the side branch) and considering only the main branch by omitting the side branch. Regarding the computational mesh of the compared arterial geometries (segment, bifurcation), we used hexahedral elements with face size between 0.01 and 0.09 mm, resulting to models of around 5 million elements. Moreover, the meshes in the lumen were generated using the commercial software ANSYS Workbench Meshing 17.2 while the equations for the blood flow were solved iteratively using ANSYS CFX 17.2 (ANSYS Inc., Canonsburg, PA).

For each case of the simulation, we computed the average cross-sectional ESS value every 0.5 mm along the stenosed vessel. Finally, we compared the ESS distribution on the bifurcated vessel with the ESS distribution on the segmented vessel. Figures 4.5 – 4.8 depict four indicative cases of the simulations and comparisons.

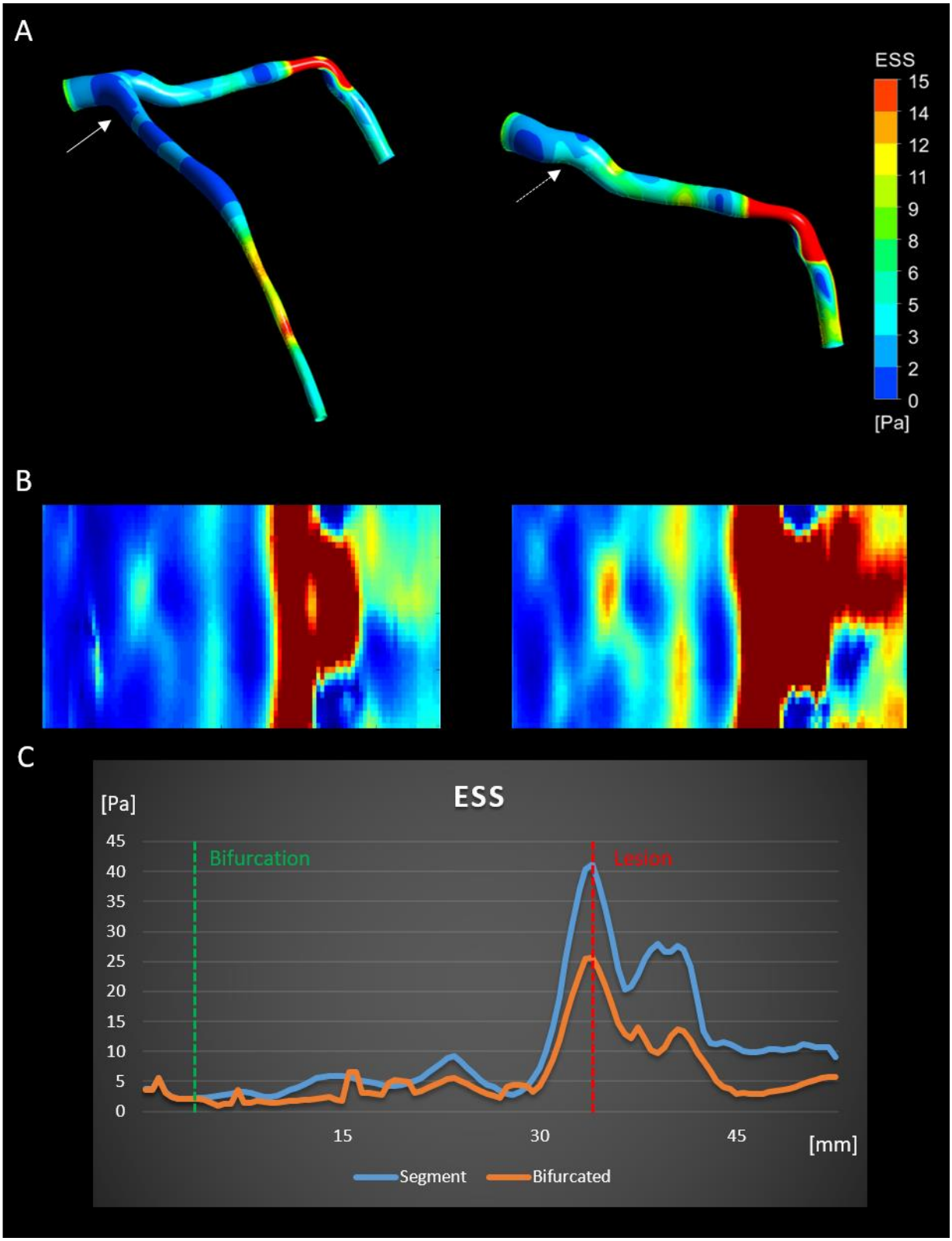

Figure 4.5: Case 5. Evaluation of the ESS both on the bifurcation (left) and the segmented (right) coronary artery, A. 3D models, B. ESS maps, C. ESS - length graphs.

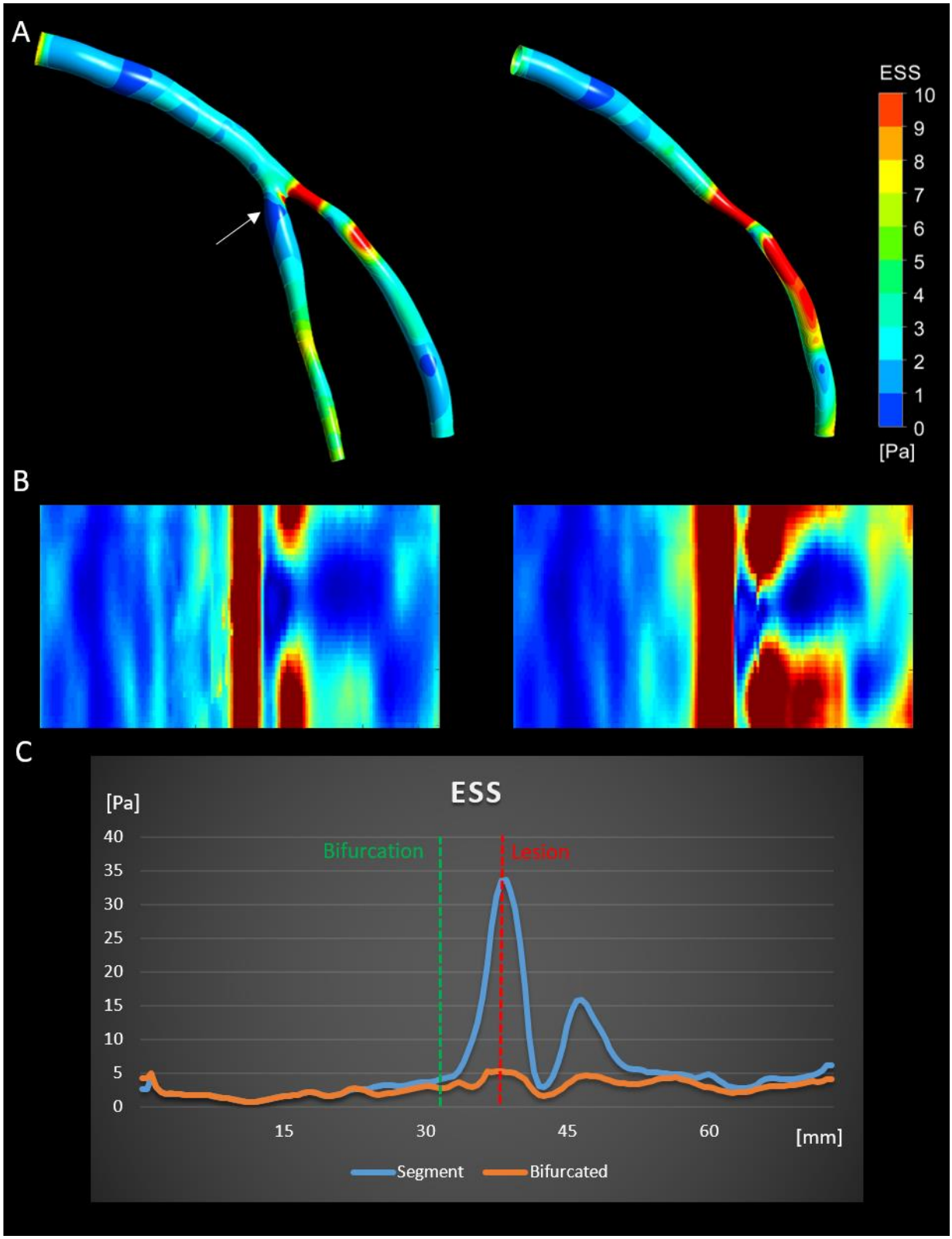

Figure 4.6: Case 1. Evaluation of the ESS both on the bifurcation (left) and the segmented (right) coronary artery, A. 3D models, B. ESS maps, C. ESS - length graphs.

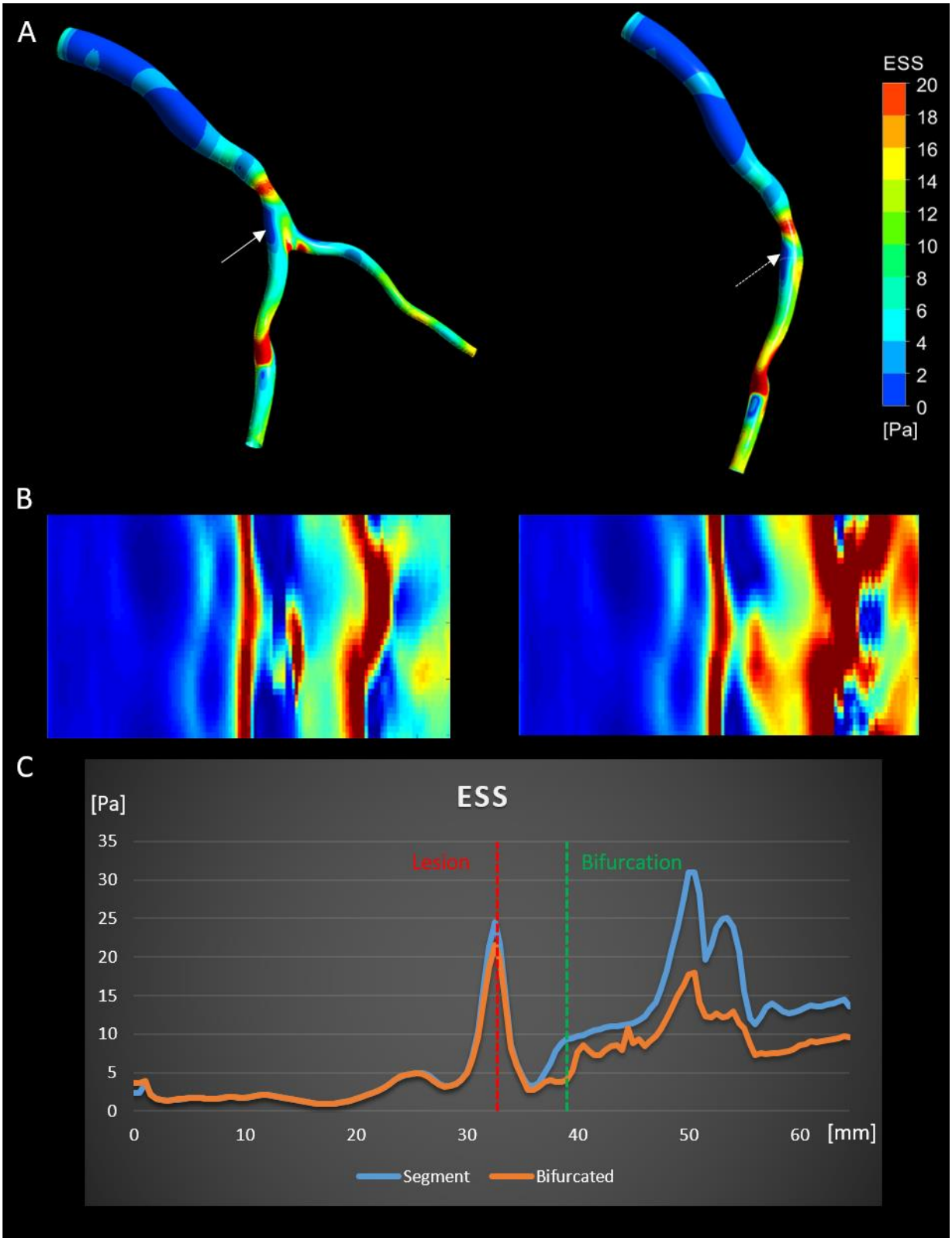

Figure 4.7: Case 9. Evaluation of the ESS both on the bifurcation (left) and the segmented (right) coronary artery, A. 3D models, B. ESS maps, C. ESS - length graphs.

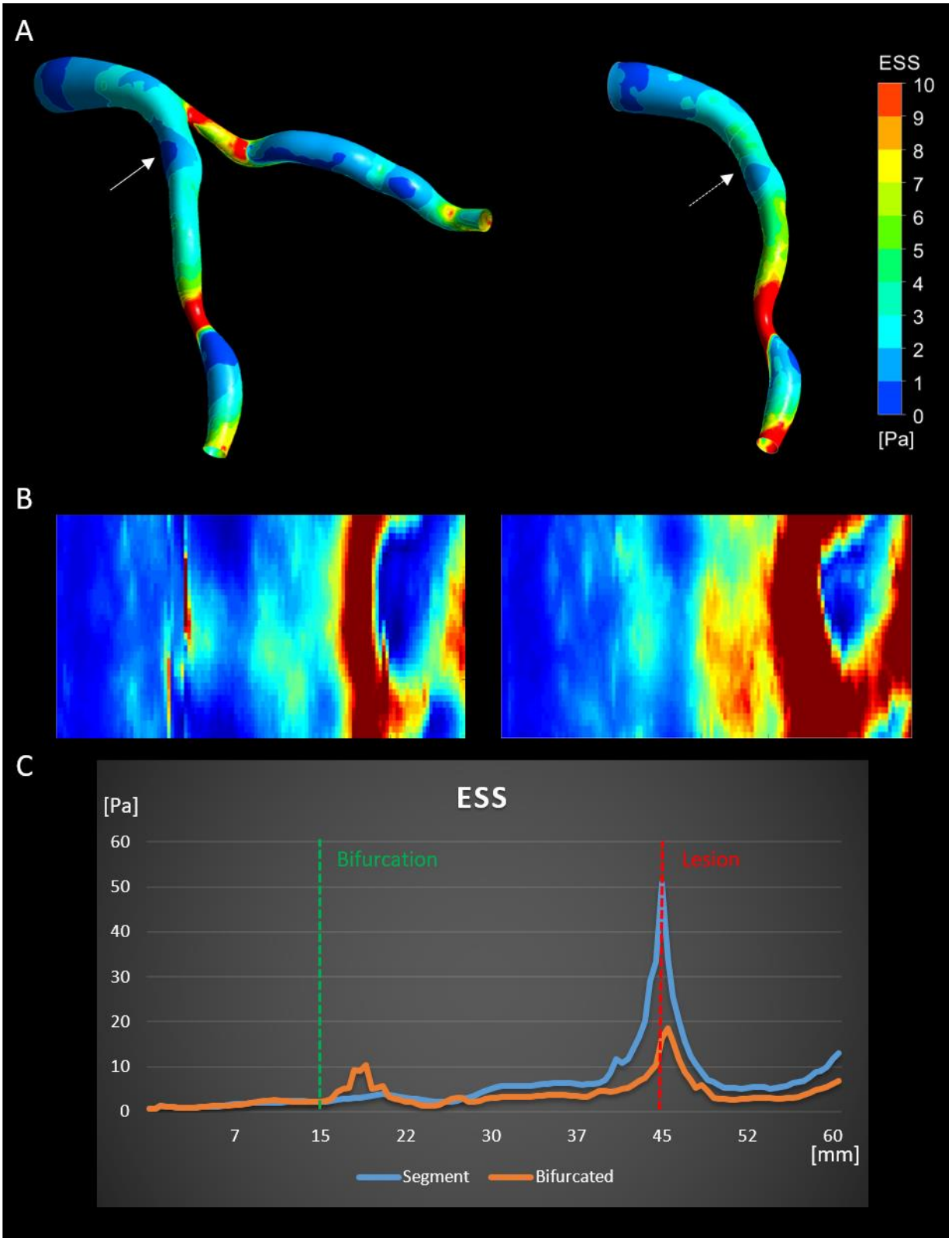

Figure 4.8: Case 11. Evaluation of the ESS both on the bifurcation (left) and the segmented (right) coronary artery, A. 3D models, B. ESS maps, C. ESS - length graphs.

The Endothelial shear stress (ESS) distribution demonstrates higher values in the case of the segmented models of the vessels than the bifurcated ones, especially around the bifurcation (Figures 4.5 – 4.8). Considering that the regions of bifurcated artery's lumen, which present low shear stress values, are prone to atherosclerosis, any computational diagnosis based on blood flow simulation in a segmented coronary vessel could lead to underestimation of the plaque growth model. The regions of bifurcated artery lumen, which present low shear stress values, are also prone to atherosclerosis (plaque growth). Table 4.1 includes the mean Endothelial Shear Stress values of the Proximal Main branch and the Distal Main branch both in the case of the bifurcated and the segmented 3D model of the coronary arteries.

Table 4.6: Mean ESS values both in the case of the bifurcated and the segmented artery.

cases	**Mean ESS [Pa]**			
	Bifurcated		**Segment**	
	Proximal Main	Distal Main	Proximal Main	Distal Main
1	1.93	3.42	2.19	8.70
2	2.75	3.34	2.59	12.58
3	3.89	4.59	3.95	14.01
4	3.29	1.94	4.26	2.55
5	2.89	5.90	3.00	9.81
6	2.50	5.28	1.81	10.51
7	4.82	9.31	3.93	12.63
8	2.42	5.69	2.96	20.11
9	3.09	9.25	3.80	14.51
10	2.89	2.78	2.42	6.14
11	2.46	5.39	1.88	12.63
12	3.29	8.90	2.28	7.55

In Table 4.6, we observe that both the segmented (without the side branch) and the bifurcated model presents almost equal mean ESS value at the Proximal Main branch. In the contrary, the Distal Main branch of the segmented artery demonstrating higher ESS values than the Distal Main of the bifurcated model. Obviously, in the case of the bifurcated artery, the blood coming through the Proximal Main Branch is being channeled both in the Distal Main and the Side Branch, producing thus lower shear stress on the endothelial tissue of the vessel. Moreover, the coronary

bifurcation anatomy generates local blood flow patterns such as turbulence flow, which provoke low ESS, especially around the bifurcation of the vessel. Nevertheless, the greater variation of the ESS between the bifurcated and the segmented (only the main branch) model of the coronary vessel is observed in the cases of LAD-LCX models where the bifurcation is located closer to the aorta.

4.2.2 Assessment of the ESS on the bifurcated vessel pre and post the PTCA

Blood flow simulations were also performed for the rest 14 bifurcated models of the coronary arteries dataset. Actually, the 3D reconstructed models correspond to 7 patients both before and after the Percutaneous Transluminal Coronary Angioplasty (PTCA) treatment. Moreover, we calculated the mean ESS value segmentally for each sub-segment of the coronary anatomy (Proximal Main, Distal Main and Side branch). Finally, we compared the variation of the ESS between the stenosed (pre) and the stented (post) artery taking into account both the position and the degree of the lesion on the vessel. Figures 4.9 – 4.11 depict the 3D models as well as the ESS distributions on them both pre and post the angioplasty procedure.

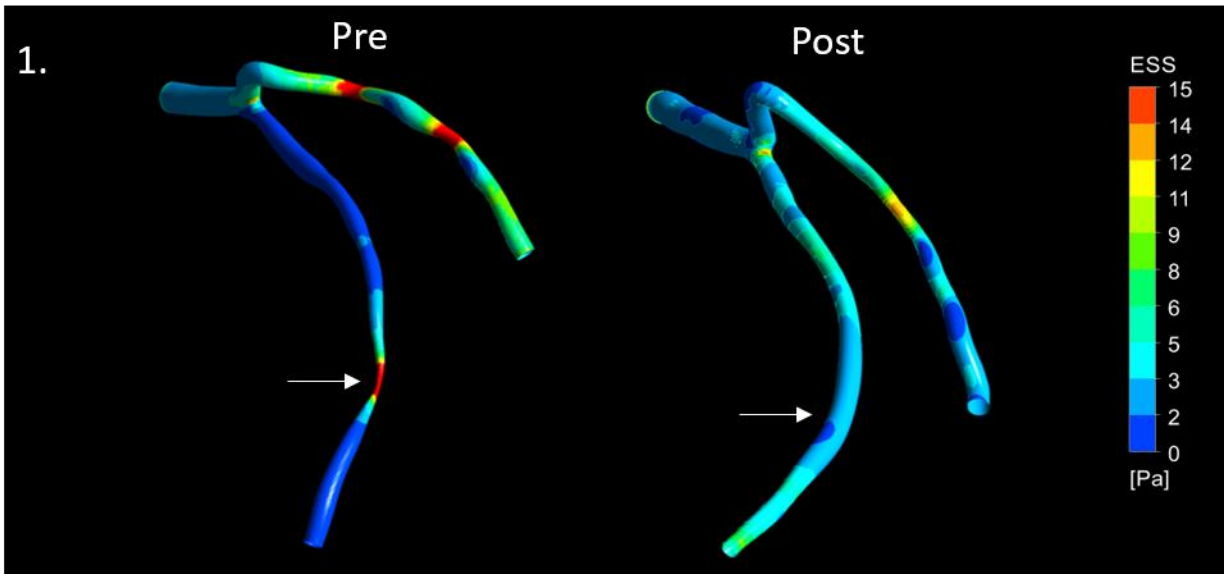

Figure 4.9: The ESS distribution on the bifurcated arteries 3D model of case 1. Before the PTCA procedure (pre) to the left, after the PTCA procedure (post) to the right.

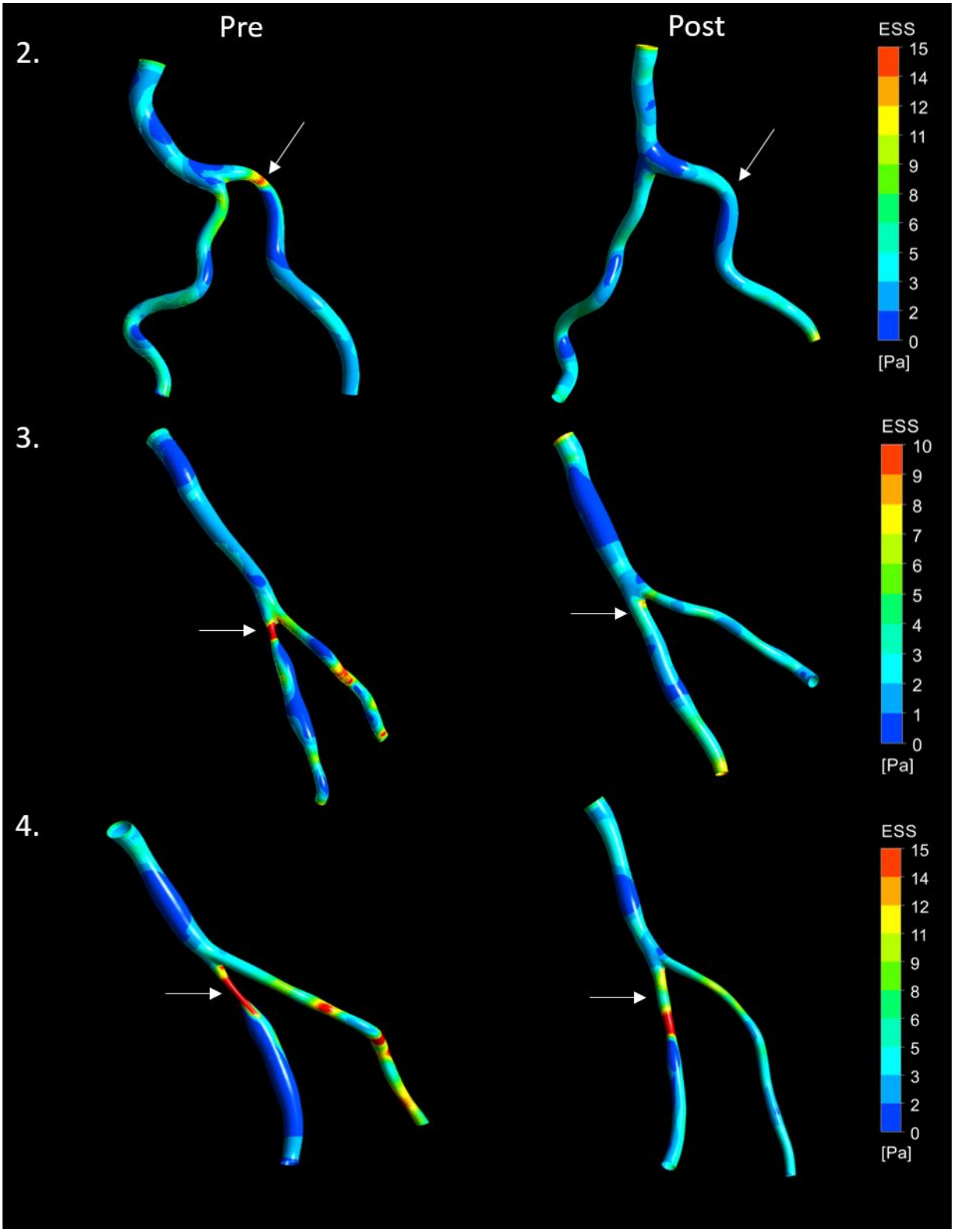

Figure 4.10: The ESS distribution on the bifurcated arteries 3D model of case 2, 3 and 4. Before the PTCA procedure (pre) to the left, after the PTCA procedure (post) to the right.

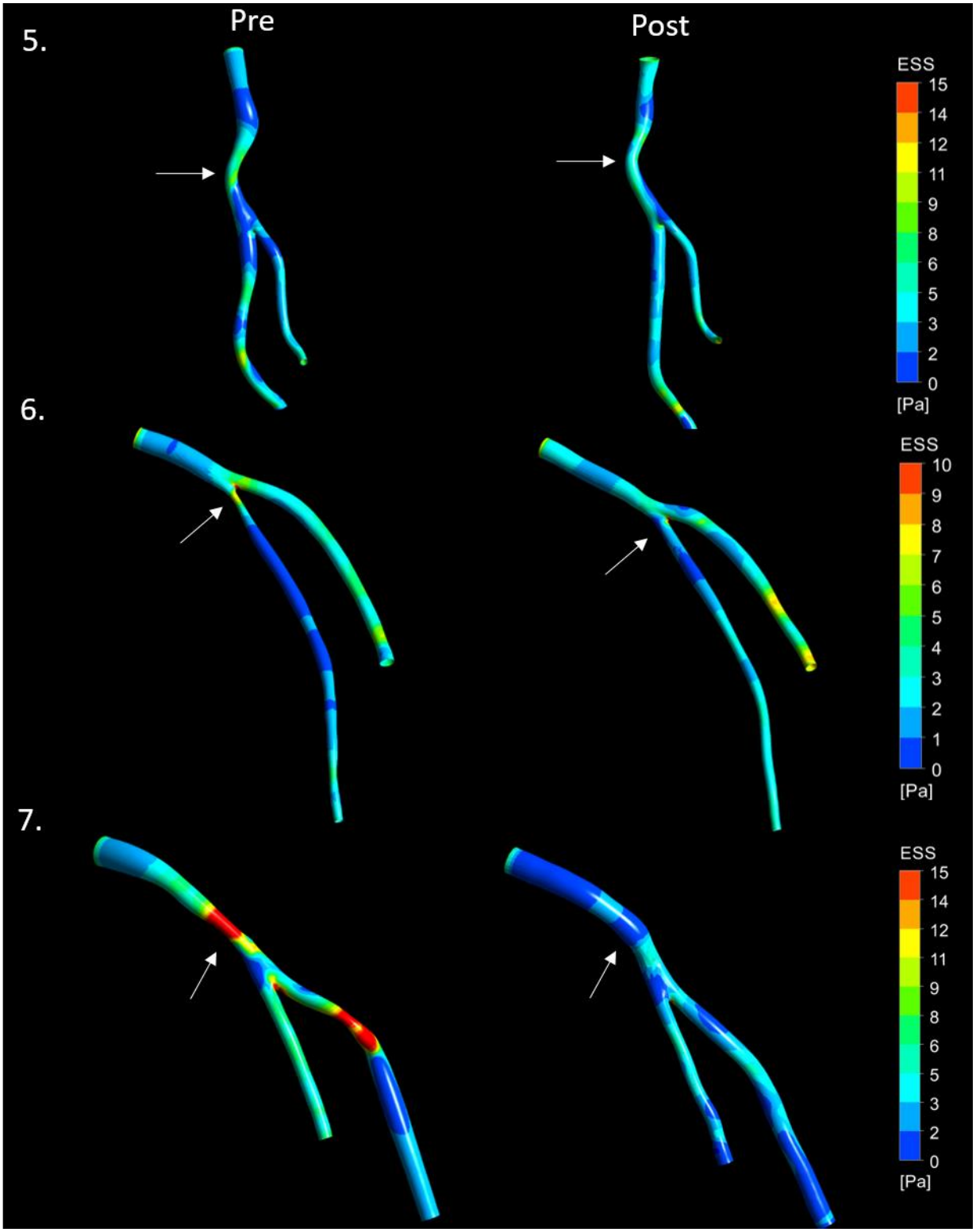

Figure 4.11: The ESS distribution on the bifurcated arteries 3D model of case 2, 3 and 4. Before the PTCA procedure (pre) to the left, after the PTCA procedure (post) to the right.

In Figures 4.9 – 4.11 we observe that almost in all of the cases of the coronary bifurcated arteries low ESS values are presented in the bifurcation both pre and post the angioplasty procedure. Actually, before the angioplasty treatment, both the distance of the lesion from the bifurcation and the degree of the arterial stenosis affect the blood flow, producing thus local blood flow patterns and low ESS values around the bifurcation. This probably could provoke a new lesion in the vessel except the existing one. Regarding the vessel after the angioplasty procedure, the artificial expansion of the lumen (balloon based) could also cause low ESS values both in the region where the stent has been applied (restenosis) and in the outside area of the vessel's bifurcation.

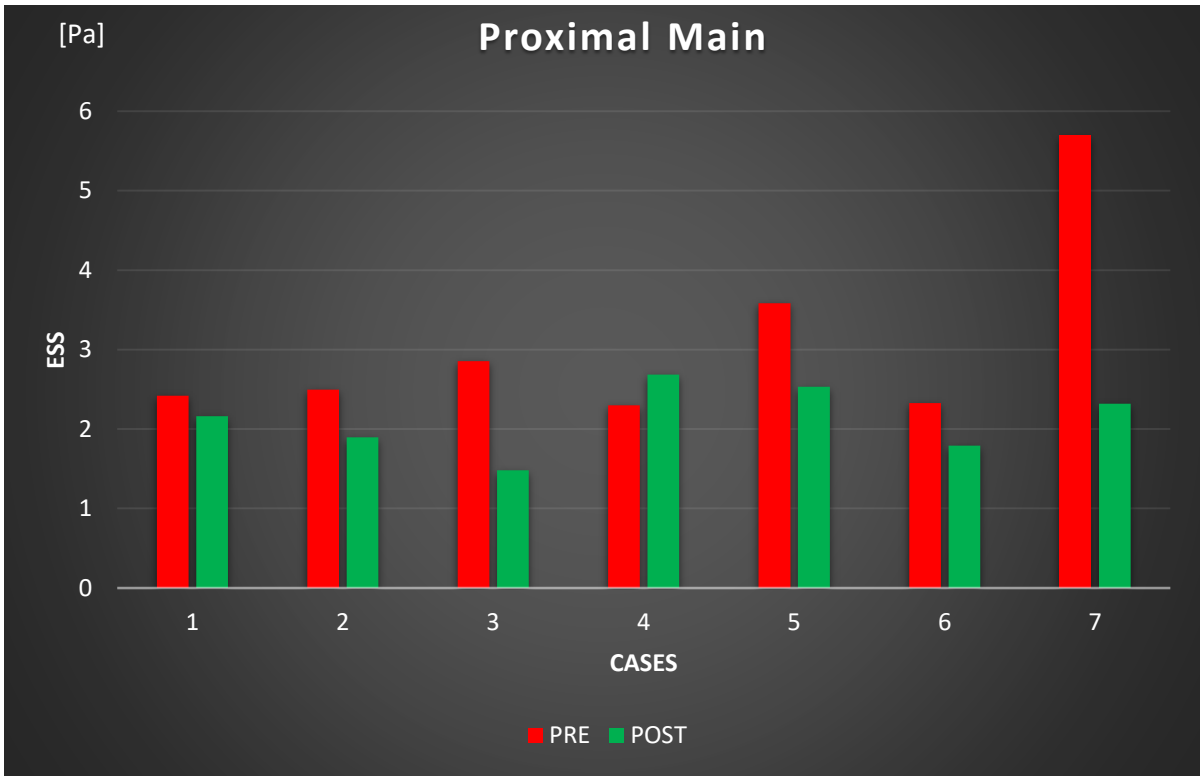

Figure 4.12: Mean ESS values of the Proximal Main Branches both pre and post the angioplasty procedure.

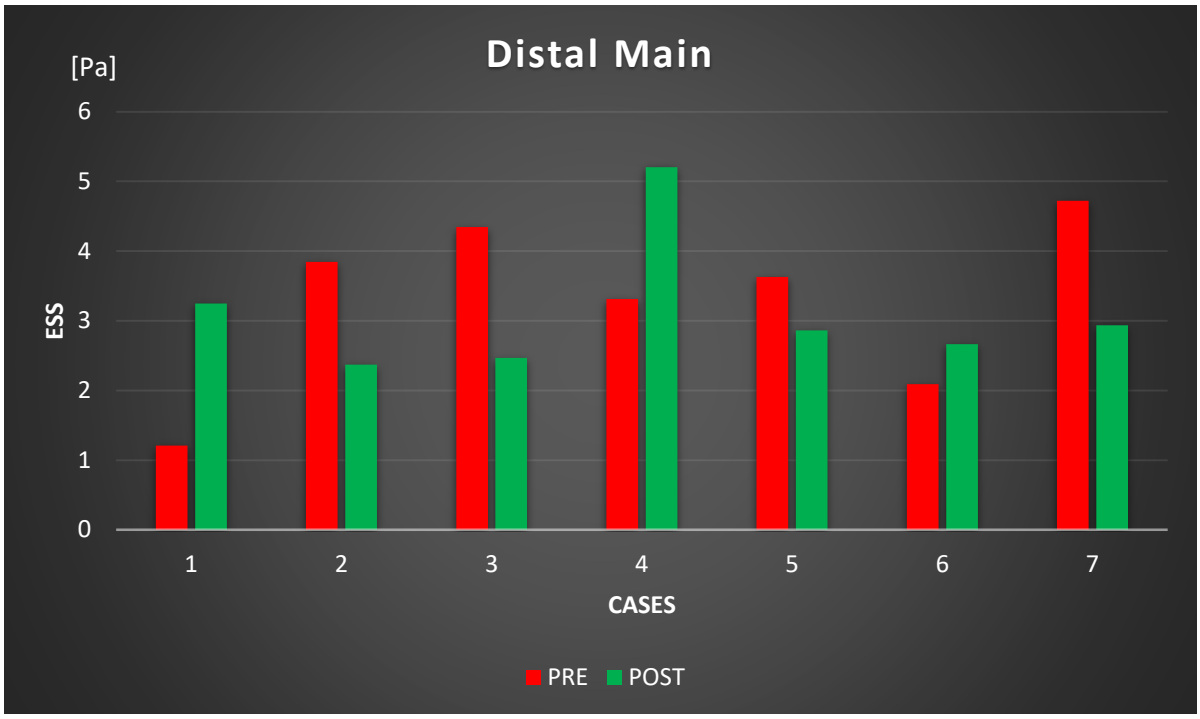

Figure 4.13: Mean ESS values of the Distal Main Branches both pre and post the angioplasty procedure.

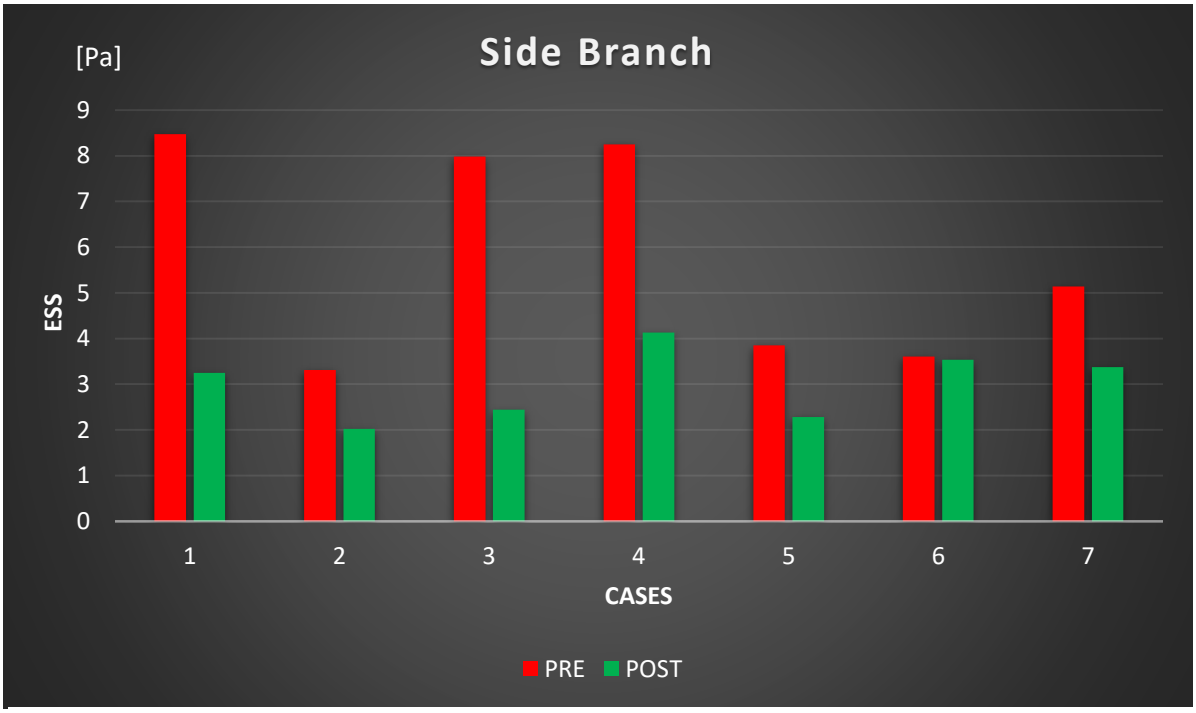

Figure 4.14: Mean ESS values of the Side Branches both pre and post the angioplasty procedure.

All the cases of the Proximal Main branch present decreased ESS values after the PTCA treatment (Figure 4.12). Obviously, the application of the stent either in the Distal Main branch or in the Side Branch enables the normal blood flow in the coronary sub-segments, reducing thus the ESS in the parent sub-segment (Proximal Main). Moreover, in the 7th case the mean ESS value is observed to be reduced significantly (≈ 4 Pa) after the angioplasty procedure due to the fact that the stenosis was located in the Proximal Main branch.

Most cases after the angioplasty procedure demonstrate decreased ESS mean values in the Distal Main branch, while less present a little bit increased. For example, the 1st case (Figure 4.13) has a significant stenosis in the Distal Main branch, which limits the blood flow to the following vessels of the coronary tree. Due to the fact that the lesion is located away from the bifurcation area, the blood is trapped into the coronary vessel before the stenosis, producing thus low mean ESS on the sub-segment, less than 1.5 Pa (Figure 4.13). Obviously, after the PTCA the blood flows normal in the vessel and regular mean shear stress value (≈3 Pa) is observed on the lumen.

High ESS mean values are observed in the side branches of all the 7 cases before the PTCA. Considering that the coronary lesion is located in the Distal Main branch, the blood flowing through the parent branch (Proximal Main) is channeled mainly in the side branch, producing thus increased shear stress on the endothelial tissue of the vessel. Nevertheless, normal (≈ 2-3 Pa) ESS mean values are observed in the side branch of all 7 cases, after the angioplasty procedure (Figure 4.14).

4.3 Computational Fraction Flow Reserve (FFR)

Taking into account the blood flow simulations, we computed the Fractional Flow Reserve (FFR) value for nine 3D models of the coronary bifurcation arteries. In fact, the gold standard FFR value is based on an invasive technique which requires the use of a dedicate pressure-flow wire, as well as the induction of hyperemia after the intravenous administration of adenosine. Thus, given the wire-based FFR values of the nine cases, we were able to validate our computational methodology. Table 4.7 contains both the computational and the wire-based FFR values for all the nine cases.

Table 4.7: Computational and wired-based FFR values.

cases	computational FFR	wire-based FFR	class
1	0.68	0.68	Pathological
2	0.96	0.97	Non-Pathological
3	0.77	0.79	Pathological
4	0.84	0.88	Non-Pathological
5	0.88	0.90	Non-Pathological
6	0.82	0.83	Non-Pathological
7	0.88	0.91	Non-Pathological
8	0.91	0.96	Non-Pathological
9	0.94	0.97	Non-Pathological

In Table 4.7 we observe that the computational FFR value presents high accuracy relatively to the wired-based FFR. It is worth noted that a FFR value of 0.80 is considered as the threshold below which, the diseased artery is in need of a Percutaneous Transluminal Coronary Angioplasty (PTCA). In the Table 4.7, we observe that both the computational and the wired-based FFR values are classified into the same class (Pathological, Non-Pathological). Moreover, performing regression analysis the computational FFR demonstrates high precision (r=0.97, p=0.014). Figure 4.15 and 4.16 depict the regression and the Bland-Altman graph of the FFR statistical analysis.

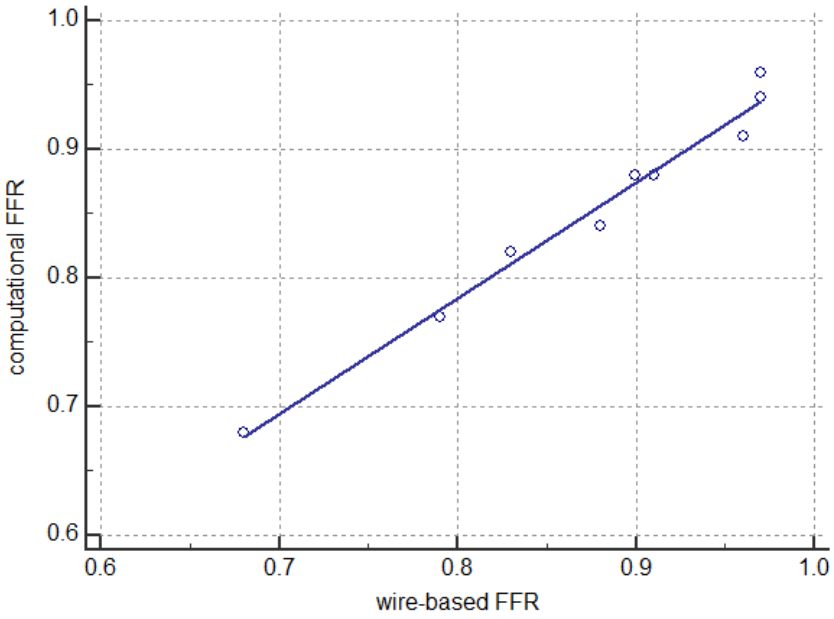

Figure 4.15: Computation vs wired-based FFR regression graph.

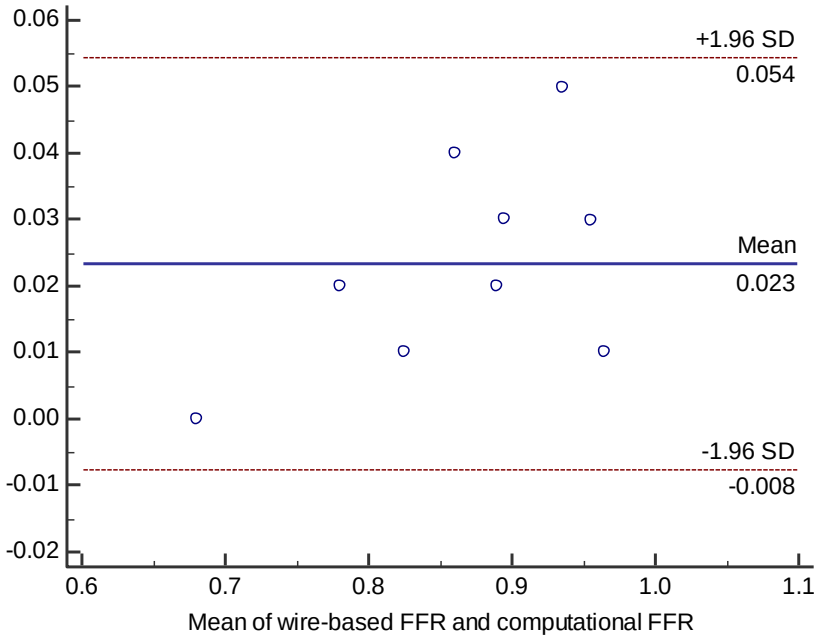

Figure 4.16: Computation vs wired-based FFR Bland-Altman graph.

Chapter 5. Conclusions

5.1 Discussion

Within this work we introduced a novel method for the 3D reconstruction of coronary bifurcation arteries from Invasive Coronary Angiography (ICA) imaging data. Moreover, in this thesis we demonstrated the impact of the side branch both in blood flow modeling and the evaluation of computational hemodynamic features such as the Endothelia Shear Stress (ESS) and the Fractional Flow Reserve (FFR). Therefore, in this chapter we briefly summarize the obtained results to finally discuss the corresponding future developments of the current study.

X-ray angiography (catheter-based) is widely used for the assessment of the coronary luminal silhouette, providing a quantitative visualization of the lesions along the coronary tree. In fact, it is still considered the gold standard in clinical decision making and therapy guidance. Nevertheless, CA is known to be fundamentally limited in some aspects. Indeed, in many clinical cases, the cumulative effect of suboptimal projection angles, vessel overlap, foreshortening, tortuosity and eccentricity may all lead to underestimation or overestimation of the lesion and probably to wrong treatment strategy. Several clinical techniques aim to detect and treat the coronary lesions, utilizing information from two or multiple X-ray images. Therefore, various

studies present novel techniques for the 3D reconstruction of the coronary vessels, using X-ray angiographic views (Quantitative Coronary Angiography - QCA). The majority of them focus on the coronary segments **omitting the side branch from the bifurcation anatomy**.

Bourantas *et. al*. [39, 100] proposed a back-projection-based method for the 3D reconstruction of the centerline of a **segmented** (without the side branch) coronary artery. Moreover, they validated their proposed method by computing the re-projection error of the 3D centerline. Toutouzas *et. al* [108] used the commercial software package QAngio XA 3D (Medis, the Netherlands), in order to reconstruct coronary **segments** in the 3D space, while blood flow simulations were performed into the 3D geometries of the vessels for the assessment of the ESS. Furthermore, Papafaklis *et. al.* [107] reconstructed coronary **segments** into the 3D space using also a commercial software, while they performed blood flow simulations into the 3D geometries of the vessels, in order to propose a new method for the computation of the FFR.

In this study we present a novel method for 3D reconstruction of coronary bifurcation **monoplane** angiographic views. Regarding the experimental part of this thesis, 26 coronary bifurcated arteries were reconstructed in the 3D space using our proposed method. Moreover, blood flow simulations were performed into the 3D geometries on the vessels. Finally, we compute the FFR value for 9 cases of the total dataset. Considering the X-ray angiography as the "gold standard" we validate the performance of the proposed algorithm we implemented two validation methods: i) the quantitative validation, and ii) validation based on the re-projection error. Comparing with the 2D QCA in the base of lumen diameter metrics, our proposed method demonstrating high accuracy for the 3D reconstruction of all the three sub-segments of the bifurcated artery. Regarding the re-projection error of all the 26 coronary bifurcated arteries, the mean **Hausdorff Distance** between the annotated vessel's silhouette and the re-projected lumen borders is **0.34 mm for the first angiographic** view and **0.26 mm for the second one (0.3 mm totally)**, while the **Dice Coefficient** value is **93 %** for both angiographies.

Comparing with other related works, our method presents decent accuracy (Table 5.1). For example, Goubergrits *et. al.* [109] reconstructed in the 3D space the model of a left coronary artery from **biplane** images using the commercial CAAS 5.2 QCA3D software of Pie Medical Imaging. According to the results of the authors, the measured re-projection error (Hausdorff Distance) was 0.236 mm for both angiographic views. Moreover, Yang *et. al.* [66] proposed a method for the 3D

reconstruction of coronary trees from **monoplane** angiographic views. Evaluating their algorithm on a dataset of 5 coronary trees, the authors measured re-projection error 0.26 mm. In fact, the quality of the 3D images registration is analogous to the number of the bifurcation points. Specifically, the more bifurcation points enforce the process of the angiographic views registration into the 3D space and potentially minimize the re-projection error. In our case, despite the existence of **a single bifurcation point,** the mean re-projection error for both angiographic views is **0.3 mm**. Finally, Cong *et. al.* [69], proposed a method for the 3D reconstruction of coronary trees using **multiple** monoplane angiographic views. According to the results of the Cong's study the mean re-projection error for 6 cases was 0.35 mm.

Table 5.1: Comparison with the literature

	Re-projection error	Images	dataset
Goubergrits *et. al.*	0.236 mm	Biplane	1 phantom of LCA
Yang *et. al.*	0.26 mm	Monoplane	5 coronary trees
Cong *et. al.*	0.35 mm	Multiple views	6 coronary trees
Our method	0.30 mm	Monoplane	26 coronary bifurcations

According to the results of the blood flow modeling, we conclude that the 3D model of the bifurcated coronary artery **presents more accurate ESS values than the 3D model without the side branch** (segmented artery). This escalation between the ESS distributions is observed especially around the region of the bifurcation, which is potentially prone to develop atheromatic plaque both *a priori* and *a posteriori* of the Percutaneous transluminal coronary angioplasty (PTCA) procedure. On this way the computational assessment of the CAD based on our methodology (bifurcated arteries) presents **robustness**, while the computational CAD analysis based on the 3D reconstruction of the segmented artery could lead to **underestimation** or **overestimation** of the ESS and probably to a wrong plaque growth model. Moreover, dangerously **low ESS values after the invasive treatment, especially around the area of the bifurcation, could cause artery restenosis, and probably new heart failure event**. Finally, the validity of our proposed method was questioned by comparing the computational FFR values against the respective invasively (wired-based) measured FFR values. Experimenting on nine cases, we observe **strong correlation** between the two methods, justifying the value of our work.

5.2 Limitations

Regarding the pros and cons of the proposed method, the 3D QCA is a quick and accurate method to assess the CAD into the 3D space, but the limited visualization of the coronary branches on the CA projections as well as confined angle offset between the angiographic views, potentially leads to failure in reconstruction process.

5.3 Future work

This thesis addresses the 3D reconstruction of the coronary bifurcation vessels in conjunction with the blood flow simulation into the 3D models. Therefore, it could be the base for further research in the flied of the cardiovascular engineering. For example, the 3D reconstruction of the total coronary tree and the blood flow modeling on top of it could be a potential evolution of this work.

Bibliography

[1] D. Edwards, L. Taylor, and K. Vorster, "Anatomy and physiology ofthe cardiovascular system," *Journal of PeriAnesthesia Nursing*, vol. 12, pp. 134-137, 1997.

[2] J. Moini, "Anatomy and Physiology of the Cardiovascular System," *Phlebotomy Principles and Practice*, pp. 35-52, 2013.

[3] D. Shier, J. Butler, and R. Lewis, *Hole's essentials of human anatomy & physiology*: McGraw-Hill Education, 2015.

[4] M. Zamir, *The physics of coronary blood flow*: Springer Science & Business Media, 2006.

[5] S. K. Steele, "Essentials of Anatomy and Physiology," in *Oncology Nursing Forum*, 2007, p. 740.

[6] A. Hasan, A. Memic, N. Annabi, M. Hossain, A. Paul, M. R. Dokmeci, *et al.*, "Electrospun scaffolds for tissue engineering of vascular grafts," *Acta biomaterialia*, vol. 10, pp. 11-25, 2014.

[7] M. L. Fitzgerald, Z. Mujawar, and N. Tamehiro, "ABC transporters, atherosclerosis and inflammation," *Atherosclerosis*, vol. 211, pp. 361-370, 2010.

[8] P. Libby, P. M. Ridker, and G. K. Hansson, "Progress and challenges in translating the biology of atherosclerosis," *Nature*, vol. 473, pp. 317-325, 2011.

[9] I. Tabas, K. J. Williams, and J. Borén, "Subendothelial lipoprotein retention as the initiating process in atherosclerosis," *Circulation*, vol. 116, pp. 1832-1844, 2007.

[10] I. Tabas, "Macrophage death and defective inflammation resolution in atherosclerosis," *Nature Reviews Immunology*, vol. 10, p. nri2675, 2009.

[11] S. Nicholls and P. Lundman, "The emerging role of lipoproteins in atherogenesis: beyond LDL cholesterol," in *Seminars in vascular medicine*, 2004, pp. 187-195.

[12] L. S. Athanasiou, D. I. Fotiadis, and L. K. Michalis, *Atherosclerotic Plaque Characterization Methods Based on Coronary Imaging*: Academic Press, 2017.

[13] J. Grotta, P. Yatsu, L. Pettigrew, H. Rhoades, P. Bratina, D. Vital, *et al.*, "Prediction of carotid stenosis progression by lipid and hematologic measurements," *Neurology*, vol. 39, pp. 1325-1325, 1989.

[14] R. L. Pande, T. S. Perlstein, J. A. Beckman, and M. A. Creager, "Secondary prevention and mortality in peripheral artery disease," *Circulation*, vol. 124, pp. 17-23, 2011.

[15] R. S. Rosenson, "Statins in atherosclerosis: lipid-lowering agents with antioxidant capabilities," *Atherosclerosis*, vol. 173, pp. 1-12, 2004.

[16] J. L. Bosch, M. T. Beinfeld, J. E. Muller, T. Brady, and G. S. Gazelle, "A Cost–Effectiveness Analysis of a Hypothetical Catheter-Based Strategy for the Detection and Treatment of Vulnerable Coronary Plaques with Drug-Eluting Stents," *Journal of interventional cardiology*, vol. 18, pp. 339-349, 2005.

[17] G. FitzGibbon, A. Leach, and H. Kafka, "Atherosclerosis of coronary artery bypass grafts and smoking," *CMAJ: Canadian Medical Association Journal*, vol. 136, p. 45, 1987.

[18] J. F. Lassen, N. R. Holm, G. Stankovic, T. Lefèvre, A. Chieffo, D. Hildick-Smith, *et al.*, "Percutaneous coronary intervention for coronary bifurcation disease: consensus from the first 10 years of the European Bifurcation Club meetings," *EuroIntervention*, vol. 10, pp. 545-60, 2014.

[19] G. Stanković, V. Vukčević, M. Živković, Z. Mehmedbegović, M. Živković, and V. Kanjuh, "Atherosclerosis and coronary artery bifurcation lesions: anatomy and flow characteristics," *Vojnosanitetski pregled*, vol. 74, pp. 161-166, 2017.

[20] J. M. Tarkin, M. R. Dweck, N. R. Evans, R. A. Takx, A. J. Brown, A. Tawakol, *et al.*, "Imaging atherosclerosis," *Circulation research*, vol. 118, pp. 750-769, 2016.

[21] A. L. Baert, *Coronary radiology*: Springer Science & Business Media, 2010.

[22] D. Hackett, G. Davies, and A. Maseri, "Pre-existing coronary stenoses in patients with first myocardial infarction are not necessarily severe," *Eur Heart J*, vol. 9, pp. 1317-23, Dec 1988.

[23] T. Pedersen, "Randomised trial of cholesterol lowering in 4444 patients with coronary heart disease: the Scandinavian Simvastatin Survival Study (4S)," *Atherosclerosis Supplements,* vol. 5, pp. 81-87, 2004.

[24] S. K. Mehta, J. R. McCrary, A. D. Frutkin, W. J. Dolla, and S. P. Marso, "Intravascular ultrasound radiofrequency analysis of coronary atherosclerosis: an emerging technology for the assessment of vulnerable plaque," *European heart journal,* vol. 28, pp. 1283-1288, 2007.

[25] J. M. Schmitt, "Optical coherence tomography (OCT): a review," *IEEE Journal of selected topics in quantum electronics,* vol. 5, pp. 1205-1215, 1999.

[26] I.-K. Jang, "Optical coherence tomography or intravascular ultrasound?," ed: JACC: Cardiovascular Interventions, 2011.

[27] M. Jaguszewski, R. Klingenberg, and U. Landmesser, "Intracoronary near-infrared spectroscopy (NIRS) imaging for detection of lipid content of coronary plaques: current experience and future perspectives," *Current cardiovascular imaging reports,* vol. 6, pp. 426-430, 2013.

[28] D. Owen, A. Lindsay, R. Choudhury, and Z. Fayad, "Imaging of atherosclerosis," *Annual review of medicine,* vol. 62, pp. 25-40, 2011.

[29] F. R. Joshi, A. C. Lindsay, D. R. Obaid, E. Falk, and J. H. Rudd, "Non-invasive imaging of atherosclerosis," *European Heart Journal–Cardiovascular Imaging,* vol. 13, pp. 205-218, 2012.

[30] C. C. PET-CT, "Fusion imaging: a new type of technologist for a new type of technology. July 31, 2002," *Journal of nuclear medicine technology,* vol. 30, p. 201, 2002.

[31] J. Eckert, M. Schmidt, A. Magedanz, T. Voigtländer, and A. Schmermund, "Coronary CT angiography in managing atherosclerosis," *International journal of molecular sciences,* vol. 16, pp. 3740-3756, 2015.

[32] L. Husmann, I. Valenta, O. Gaemperli, O. Adda, V. Treyer, C. A. Wyss, *et al.*, "Feasibility of low-dose coronary CT angiography: first experience with prospective ECG-gating," *European heart journal,* vol. 29, pp. 191-197, 2007.

[33] J. P. Earls, E. L. Berman, B. A. Urban, C. A. Curry, J. L. Lane, R. S. Jennings, *et al.*, "Prospectively gated transverse coronary CT angiography versus retrospectively gated helical technique: improved image quality and reduced radiation dose," *Radiology,* vol. 246, pp. 742-753, 2008.

[34] A. Berger, "How does it work?: Magnetic resonance imaging," *BMJ: British Medical Journal,* vol. 324, p. 35, 2002.

[35] S. Kang, C. Kyung, J. S. Park, S. Kim, S.-P. Lee, M. K. Kim, *et al.*, "Subclinical vascular inflammation in subjects with normal weight obesity and its association with body fat: an 18 F-FDG-PET/CT study," *Cardiovascular diabetology,* vol. 13, p. 70, 2014.

[36] M. Nichols, N. Townsend, P. Scarborough, and M. Rayner, "Cardiovascular disease in Europe: epidemiological update," *European heart journal,* vol. 34, pp. 3028-3034, 2013.

[37] D. B. Mark, D. S. Berman, M. J. Budoff, J. J. Carr, T. C. Gerber, H. S. Hecht, *et al.*, "ACCF/ACR/AHA/NASCI/SAIP/SCAI/SCCT 2010 expert consensus document on coronary computed tomographic angiography," *Catheterization and Cardiovascular Interventions,* vol. 76, 2010.

[38] N. E. Green, S. Y. J. Chen, A. R. Hansgen, J. C. Messenger, B. M. Groves, and J. D. Carroll, "Angiographic views used for percutaneous coronary interventions: A three-dimensional analysis of physician-determined vs. computer-generated views," *Catheterization and Cardiovascular Interventions,* vol. 64, pp. 451-459, 2005.

[39] C. V. Bourantas, M. I. Papafaklis, L. Athanasiou, F. G. Kalatzis, K. K. Naka, P. K. Siogkas, *et al.*, "A new methodology for accurate 3-dimensional coronary artery reconstruction using routine intravascular ultrasound and angiographic data: implications for widespread assessment of endothelial shear stress in humans," *EuroIntervention,* vol. 9, pp. 582-93, 2013.

[40] M. T. Dehkordi, S. Sadri, and A. Doosthoseini, "A review of coronary vessel segmentation algorithms," *Journal of medical signals and sensors,* vol. 1, p. 49, 2011.

[41] M. Kumar, L. Wei, R. Turlapthi, and J. S. Suri, "DSA image enhancement via multi-resolution motion correction for interventional procedures: a robust strategy," in

Proceedings of the fifth IASTED international conference: biomedical engineering. ACTA Press, Innsbruck, 2007.

[42] D. L. Wilson and E. J. Kaplan, "Linear and morphological digital image enhancement of peripheral angiography images," *Proceedings of SPIE: medical imaging IV: image processing. Newport Beach*, 1990.

[43] P. M. van der Zwet and J. H. Reiber, "The influence of image enhancement and reconstruction on quantitative coronary arteriography," *The International Journal of Cardiac Imaging*, vol. 11, pp. 211-221, 1995.

[44] E. H. Meijering, K. J. Zuiderveld, and M. A. Viergever, "Image registration for digital subtraction angiography," *International Journal of Computer Vision*, vol. 31, pp. 227-246, 1999.

[45] A. K. Klein, F. Lee, and A. A. Amini, "Quantitative coronary angiography with deformable spline models," *IEEE transactions on medical imaging*, vol. 16, pp. 468-482, 1997.

[46] A. P. Dhawan and L. Arata, "Segmentation of medical images through competitive learning," *Computer Methods and Programs in Biomedicine*, vol. 40, pp. 203-215, 1993.

[47] D. P. Kottke and Y. Sun, "Segmentation of coronary arteriograms by iterative ternary classification," *IEEE Transactions on Biomedical Engineering*, vol. 37, pp. 778-785, 1990.

[48] I. Liu and Y. Sun, "Recursive tracking of vascular networks in angiograms based on the detection-deletion scheme," *IEEE Transactions on Medical Imaging*, vol. 12, pp. 334-341, 1993.

[49] F. K. Quek and C. Kirbas, "Vessel extraction in medical images by wave-propagation and traceback," *IEEE transactions on Medical Imaging*, vol. 20, pp. 117-131, 2001.

[50] M. Gudmundsson, E. A. El-Kwae, and M. R. Kabuka, "Edge detection in medical images using a genetic algorithm," *IEEE transactions on medical imaging*, vol. 17, pp. 469-474, 1998.

[51] S. Kobashi, N. Kamiura, Y. Hata, and F. Miyawaki, "Fuzzy information granulation on blood vessel extraction from 3D TOF MRA image," *International journal of pattern recognition and artificial intelligence*, vol. 14, pp. 409-425, 2000.

[52] T. Kayikcioglu, A. Gangal, M. Turhal, and C. Kose, "A surface-based method for detection of coronary vessel boundaries in poor quality X-ray angiogram images," *Pattern Recognition Letters,* vol. 23, pp. 783-802, 2002.

[53] F. Auricchio, M. Conti, C. Ferrazzano, and G. A. Sgueglia, "A simple framework to generate 3D patient-specific model of coronary artery bifurcation from single-plane angiographic images," *Computers in biology and medicine,* vol. 44, pp. 97-109, 2014.

[54] H. Lee, H. Shim, and H.-J. Chang, "Intensity-vesselness Gaussian mixture model (IVGMM) for 2D+ t segmentation of coronary arteries for X-ray angiography image sequences," *Journal of X-ray Science and Technology,* vol. 23, pp. 579-592, 2015.

[55] A. F. Frangi, W. J. Niessen, K. L. Vincken, and M. A. Viergever, "Multiscale vessel enhancement filtering," in *International Conference on Medical Image Computing and Computer-Assisted Intervention*, 1998, pp. 130-137.

[56] K. Krissian, G. Malandain, N. Ayache, R. Vaillant, and Y. Trousset, "Model-based detection of tubular structures in 3D images," *Computer vision and image understanding,* vol. 80, pp. 130-171, 2000.

[57] I. Cruz-Aceves, A. Hernandez-Aguirre, and S. I. Valdez, "On the performance of nature inspired algorithms for the automatic segmentation of coronary arteries using Gaussian matched filters," *Applied Soft Computing,* vol. 46, pp. 665-676, 2016.

[58] A. Zifan, P. Liatsis, P. Kantartzis, M. Gavaises, N. Karcanias, and D. Katritsis, "Automatic 3D reconstruction of coronary artery centerlines from monoplane X-ray angiogram images," *International Journal of Biological and Medical Sciences,* vol. 2, pp. 105-110, 2008.

[59] A. Zifan and P. Liatsis, "Patient-Specific Computational Models of Coronary Arteries Using Monoplane X-Ray Angiograms," *Computational and mathematical methods in medicine,* vol. 2016, 2016.

[60] P. S.-P. Wang and Y. Zhang, "A fast and flexible thinning algorithm," *IEEE Transactions on Computers,* vol. 38, pp. 741-745, 1989.

[61] S. Çimen, A. Gooya, M. Grass, and A. F. Frangi, "Reconstruction of coronary arteries from X-ray angiography: A review," *Medical image analysis,* vol. 32, pp. 46-68, 2016.

[62] K. R. Hoffmann, A. Sen, L. Lan, K.-G. Chua, J. Esthappan, and M. Mazzucco, "A system for determination of 3D vessel tree centerlines from biplane images," *The International Journal of Cardiac Imaging,* vol. 16, pp. 315-330, 2000.

[63] S. J. Chen and J. D. Carroll, "3-D reconstruction of coronary arterial tree to optimize angiographic visualization," *IEEE transactions on medical imaging,* vol. 19, pp. 318-336, 2000.

[64] C. Blondel, G. Malandain, R. Vaillant, and N. Ayache, "Reconstruction of coronary arteries from a single rotational X-ray projection sequence," *IEEE Transactions on Medical Imaging,* vol. 25, pp. 653-663, 2006.

[65] P. Fallavollita and F. Cheriet, "Optimal 3D reconstruction of coronary arteries for 3D clinical assessment," *Computerized Medical Imaging and Graphics,* vol. 32, pp. 476-487, 2008.

[66] J. Yang, Y. Wang, Y. Liu, S. Tang, and W. Chen, "Novel approach for 3-D reconstruction of coronary arteries from two uncalibrated angiographic images," *IEEE Transactions on Image Processing,* vol. 18, pp. 1563-1572, 2009.

[67] R. Liao, D. Luc, Y. Sun, and K. Kirchberg, "3-D reconstruction of the coronary artery tree from multiple views of a rotational X-ray angiography," *The international journal of cardiovascular imaging,* vol. 26, pp. 733-749, 2010.

[68] X. Liu, F. Hou, A. Hao, and H. Qin, "A parallelized 4D reconstruction algorithm for vascular structures and motions based on energy optimization," *The Visual Computer,* vol. 31, pp. 1431-1446, 2015.

[69] W. Cong, J. Yang, D. Ai, Y. Chen, Y. Liu, and Y. Wang, "Quantitative analysis of deformable model-based 3-D reconstruction of coronary artery from multiple angiograms," *IEEE Transactions on Biomedical Engineering,* vol. 62, pp. 2079-2090, 2015.

[70] A. K. Law, H. Zhu, and F. H. Chan, "3D reconstruction of coronary artery using biplane angiography," in *Engineering in Medicine and Biology Society, 2003. Proceedings of the 25th Annual International Conference of the IEEE*, 2003, pp. 533-536.

[71] U. Jandt, D. Schäfer, M. Grass, and V. Rasche, "Automatic generation of time resolved motion vector fields of coronary arteries and 4D surface extraction using rotational x-ray angiography," *Physics in medicine and biology,* vol. 54, p. 45, 2008.

[72] J. Li and L. D. Cohen, "Reconstruction of 3D tubular structures from cone-beam projections," in *Biomedical Imaging: From Nano to Macro, 2011 IEEE International Symposium on*, 2011, pp. 1162-1166.

[73] U. Jandt, D. Schäfer, M. Grass, and V. Rasche, "Automatic generation of 3D coronary artery centerlines using rotational X-ray angiography," *Medical Image Analysis,* vol. 13, pp. 846-858, 2009.

[74] E. M. Khouri, D. E. Gregg, and H. S. Lowensohn, "Flow in the major branches of the left coronary artery during experimental coronary insufficiency in the unanesthetized dog," *Circulation research,* vol. 23, pp. 99-109, 1968.

[75] W. M. Fam and M. McGregor, "Pressure-flow relationships in the coronary circulation," *Circulation research,* vol. 25, pp. 293-301, 1969.

[76] D. N. Ku, D. P. Giddens, C. K. Zarins, and S. Glagov, "Pulsatile flow and atherosclerosis in the human carotid bifurcation. Positive correlation between plaque location and low oscillating shear stress," *Arteriosclerosis, thrombosis, and vascular biology,* vol. 5, pp. 293-302, 1985.

[77] C. K. Zarins, D. P. Giddens, B. Bharadvaj, V. S. Sottiurai, R. F. Mabon, and S. Glagov, "Carotid bifurcation atherosclerosis. Quantitative correlation of plaque localization with flow velocity profiles and wall shear stress," *Circulation research,* vol. 53, pp. 502-514, 1983.

[78] H. Mohammadi and F. Bahramian, "Boundary conditions in simulation of stenosed coronary arteries," *Cardiovascular Engineering,* vol. 9, pp. 83-91, 2009.

[79] J. V. Soulis, G. D. Giannoglou, Y. S. Chatzizisis, K. V. Seralidou, G. E. Parcharidis, and G. E. Louridas, "Non-Newtonian models for molecular viscosity and wall shear stress in a 3D reconstructed human left coronary artery," *Medical engineering & physics,* vol. 30, pp. 9-19, 2008.

[80] C. A. Taylor and D. A. Steinman, "Image-based modeling of blood flow and vessel wall dynamics: applications, methods and future directions," *Annals of biomedical engineering,* vol. 38, pp. 1188-1203, 2010.

[81] C. A. Taylor, T. J. Hughes, and C. K. Zarins, "Finite element modeling of blood flow in arteries," *Computer methods in applied mechanics and engineering,* vol. 158, pp. 155-196, 1998.

[82] Y. Li, J. L. Gutiérrez-Chico, N. R. Holm, W. Yang, L. Hebsgaard, E. H. Christiansen, *et al.*, "Impact of side branch modeling on computation of endothelial shear stress in coronary artery disease: coronary tree reconstruction by fusion of 3D angiography and OCT," *Journal of the American College of Cardiology,* vol. 66, pp. 125-135, 2015.

[83] A. Sakellarios, C. V. Bourantas, S.-L. Papadopoulou, P. H. Kitslaar, C. Girasis, G. W. Stone, *et al.*, "The effect of coronary bifurcation and haemodynamics in prediction of atherosclerotic plaque development: a serial computed tomographic coronary angiographic study," *EuroIntervention: journal of EuroPCR in collaboration with the Working Group on Interventional Cardiology of the European Society of Cardiology,* vol. 13, pp. e1084-e1091, 2017.

[84] M. I. Papafaklis, C. V. Bourantas, P. E. Theodorakis, C. S. Katsouras, D. I. Fotiadis, and L. K. Michalis, "Association of endothelial shear stress with plaque thickness in a real three-dimensional left main coronary artery bifurcation model," *International journal of cardiology,* vol. 115, pp. 276-278, 2007.

[85] K. Shishido, A. Antoniadis, S. Takahashi, M. Tsuda, M. I. Papafaklis, I. Andreou, *et al.*, "The Relationship of Endothelial Shear Stress after Stent Implantation with In-Stent Neointimal Hyperplasia and Clinical Outcomes in Humans," ed: Am Heart Assoc, 2014.

[86] T. P. van de Hoef, M. A. van Lavieren, P. Damman, R. Delewi, M. A. Piek, S. A. Chamuleau, *et al.*, "Physiological basis and long-term clinical outcome of discordance between fractional flow reserve and coronary flow velocity reserve in coronary stenoses of intermediate severity," *Circulation: Cardiovascular Interventions,* vol. 7, pp. 301-311, 2014.

[87] M. Echavarría-Pinto, T. P. van de Hoef, P. W. Serruys, J. J. Piek, and J. Escaned, "Facing the complexity of ischaemic heart disease with intracoronary pressure and flow measurements: beyond fractional flow reserve interrogation of the coronary circulation," *Current opinion in cardiology,* vol. 29, pp. 564-570, 2014.

[88] T. P. van de Hoef, M. Meuwissen, and J. J. Piek, "Fractional flow reserve and beyond," *Heart,* vol. 99, pp. 1699-1705, 2013.

[89] S. Tu, E. Barbato, Z. Köszegi, J. Yang, Z. Sun, N. R. Holm, *et al.*, "Fractional flow reserve calculation from 3-dimensional quantitative coronary angiography and TIMI frame count: a fast computer model to quantify the functional significance of moderately obstructed coronary arteries," *JACC: Cardiovascular Interventions,* vol. 7, pp. 768-777, 2014.

[90] L. Liu, W. Yang, Y. Nagahara, Y. Li, S. R. Lamooki, T. Muramatsu, *et al.*, "The impact of image resolution on computation of fractional flow reserve: coronary computed tomography angiography versus 3-dimensional quantitative coronary angiography," *The international journal of cardiovascular imaging,* vol. 32, pp. 513-523, 2016.

[91] G. Tommasini, A. Camerini, A. Gatti, G. Derchi, A. Bruzzone, and C. Vecchio, "Panoramic coronary angiography," *Journal of the American College of Cardiology,* vol. 31, pp. 871-877, 1998.

[92] A. J. Klein, J. A. Garcia, P. A. Hudson, M. S. Kim, J. C. Messenger, I. P. Casserly, *et al.*, "Safety and efficacy of dual-axis rotational coronary angiography vs. standard coronary angiography," *Catheterization and Cardiovascular Interventions,* vol. 77, pp. 820-827, 2011.

[93] R. S. Giuberti, A. Caixeta, A. C. Carvalho, M. M. Soares, E. O. ABREU-SILVA, J. O. M. Pestana, *et al.*, "A randomized trial comparing dual axis rotational versus conventional coronary angiography in a population with a high prevalence of coronary artery disease," *Journal of interventional cardiology,* vol. 27, pp. 456-464, 2014.

[94] D. Schafer, J. Borgert, V. Rasche, and M. Grass, "Motion-compensated and gated cone beam filtered back-projection for 3-D rotational X-ray angiography," *IEEE transactions on medical imaging,* vol. 25, pp. 898-906, 2006.

[95] S. Y. J. Chen and C. E. Metz, "Improved determination of biplane imaging geometry from two projection images and its application to three-dimensional reconstruction of coronary arterial trees," *Medical Physics*, vol. 24, pp. 633-654, 1997.

[96] J. C. Messenger, S. J. Chen, J. D. Carroll, J. Burchenal, K. Kioussopoulos, and B. M. Groves, "3D coronary reconstruction from routine single-plane coronary angiograms: clinical validation and quantitative analysis of the right coronary artery in 100 patients," *The International Journal of Cardiac Imaging*, vol. 16, pp. 413-427, 2000.

[97] M. Sonka and V. Hlavac, "R. Boyle Image Processing," *Analysis, And Machine Vision. Pp10-210 &*, pp. 646-670, 1999.

[98] C. Metz, M. Schaap, A. Weustink, N. Mollet, T. van Walsum, and W. Niessen, "Coronary centerline extraction from CT coronary angiography images using a minimum cost path approach," *Medical physics*, vol. 36, pp. 5568-5579, 2009.

[99] J. A. Sethian, "Fast marching methods," *SIAM review*, vol. 41, pp. 199-235, 1999.

[100] C. V. Bourantas, I. C. Kourtis, M. E. Plissiti, D. I. Fotiadis, C. S. Katsouras, M. I. Papafaklis, *et al.*, "A method for 3D reconstruction of coronary arteries using biplane angiography and intravascular ultrasound images," *Computerized Medical Imaging and Graphics*, vol. 29, pp. 597-606, 2005.

[101] M. Hosaka, *Modeling of Curves and Surfaces in CAD/CAM*: Springer Science & Business Media, 2012.

[102] D.-T. Lee and B. J. Schachter, "Two algorithms for constructing a Delaunay triangulation," *International Journal of Computer & Information Sciences*, vol. 9, pp. 219-242, 1980.

[103] P. Garrone, G. BIONDI-ZOCCAI, I. Salvetti, N. Sina, I. Sheiban, P. R. Stella, *et al.*, "Quantitative coronary angiography in the current era: principles and applications," *Journal of interventional cardiology*, vol. 22, pp. 527-536, 2009.

[104] A. A. Taha and A. Hanbury, "Metrics for evaluating 3D medical image segmentation: analysis, selection, and tool," *BMC medical imaging*, vol. 15, p. 29, 2015.

[105] A. A. Taha and A. Hanbury, "An efficient algorithm for calculating the exact Hausdorff distance," *IEEE transactions on pattern analysis and machine intelligence,* vol. 37, pp. 2153-2163, 2015.

[106] L. R. Dice, "Measures of the amount of ecologic association between species," *Ecology,* vol. 26, pp. 297-302, 1945.

[107] M. I. Papafaklis, T. Muramatsu, Y. Ishibashi, L. S. Lakkas, S. Nakatani, C. V. Bourantas, *et al.*, "Fast virtual functional assessment of intermediate coronary lesions using routine angiographic data and blood flow simulation in humans: comparison with pressure wire-fractional flow reserve," *EuroIntervention: journal of EuroPCR in collaboration with the Working Group on Interventional Cardiology of the European Society of Cardiology,* vol. 10, pp. 574-583, 2014.

[108] K. Toutouzas, Y. S. Chatzizisis, M. Riga, A. Giannopoulos, A. P. Antoniadis, S. Tu, *et al.*, "Accurate and reproducible reconstruction of coronary arteries and endothelial shear stress calculation using 3D OCT: comparative study to 3D IVUS and 3D QCA," *Atherosclerosis,* vol. 240, pp. 510-519, 2015.

[109] L. Goubergrits, E. Wellnhofer, U. Kertzscher, K. Affeld, C. Petz, and H.-C. Hege, "Coronary artery WSS profiling using a geometry reconstruction based on biplane angiography," *Annals of biomedical engineering,* vol. 37, pp. 682-691, 2009.

Publications:

1. **Ioannis O. Andrikos**, Antonis I. Sakellarios, Panagiotis K. Siogkas, George Rigas, Themis P. Exarchos, Lambros S. Athanasiou, Antonis. Karanasos, Kostas Toutouzas, Dimitris Tousoulis, Lampros K. Michalis, Dimitrios I. Fotiadis, "Semi-automated reconstruction of coronary bifurcations using angiography and OCT", International Conference on Biomedical and Health Informatics (BHI), 2017
2. **Ioannis O. Andrikos**, Antonis I. Sakellarios, Panagiotis K. Siogkas, George Rigas, Themis P. Exarchos, Lambros S. Athanasiou, Antonis. Karanasos, Kostas Toutouzas, Dimitris Tousoulis, Lampros K. Michalis, Dimitrios I. Fotiadis, "A novel hybrid approach for reconstruction of coronary bifurcations using angiography and OCT", International Biomedical Engineering (EMBC), 2017
3. Vassiliki I. Kigka, George Rigas, Antonis Sakellarios, Panagiotis Siogkas, **Ioannis O. Andrikos**, Themis P. Exarchos, Dimitra Loggitsi, Constantinos D. Anagnostopoulos, Lampros K. Michalis, Danilo Negliaf, Gualtriero Pelosi, Oberdan Parodi, Dimitrios I. Fotiadis, "3D Reconstruction of Coronary Arteries and Atherosclerotic Plaques based on Computed Tomography Angiography images", Biomedical Signal Processing and Control, 2017
4. Antonis I. Sakellarios, George Rigas, Vassiliki Kigka, Panagiotis Siogkas, Panagiota Tsompou, Georgia Karanasiou, Themis Exarchos, **Ioannis Andrikos**, Nikolaos Tachos, Gualtriero Pelosi, Oberdan Parodi, Dimitrios I. Fotiaids "SMARTool: A Tool for Clinical Decision Support for the Management of Patients with Coronary Artery Disease Based on Modeling of Atherosclerotic Plaque Process", International Biomedical Engineering (EMBC), 2017
5. Theodora Bampali, Lampros Lakkas, Antonis Sakellarios, Panagiotis Siogkas, **John Andrikos**, Anna Kotsia, Michail Papafaklis, Christos Katsouras, Dimitrios I Fotiadis, Dimitrios Karmpaliotis, Emmanouil Brilakis, Lampros Michalis, "The correlation of near-infrared-spectroscopy lipid pools with computationally measured accumulation of low density lipoprotein in coronary arteries", Atherosclerosis, 2017
6. **Ioannis O. Andrikos**, Atnonis I. Sakellarios, Panagiotis K. Siogkas, Panagiota I. Tsompou, Vassiliki I. Kigka, Lampros. K. Michalis, Dimitrios I. Fotiadis, "A novel method

for 3D reconstruction of coronary bi-furcation using Quantitative Coronary Angiography", in World Congress on Medical Physics and Biomedical Engineering (IUPESM), 2018

7. Antonios Karanasos, Konstantinos Toutouzas, **Ioannis Andrikos**, Antonis Sakellarios, Panagiotis Siogkas, George Rigas, Themis Exarchos, Andreas Synetos, George Latsios, Eleftherios Tsiamis, Lampros Michalis, Dimitris Fotiadis and Dimitris Tousoulis, "Evaluation of flow dynamics in bifurcations by fusion of 3-dimensional angiography and two-vessel optical coherence tomography", Journal of the American College of Cardiology (JACC), 2018

Short CV:

Ioannis O. Andrikos was born in Ioannina, Greece in 1992. In 2015 he received his diploma degree (diploma of Computer Engineer – 5 years equivalent to Meng.) from the department of Computer Engineering & informatics of University of Patras. In 2018 he accomplished the MSc program "Advanced Materials" associated with Biomaterials and Biomedical Technology of the Department of Materials Science and Engineering, University of Ioannina, Ioannina Greece. Since 2016 he is working on cardiovascular engineering as research associate of Unit of Medical Technology and Intelligent Information Systems, University of Ioannina.